technische universität
dortmund

MAX-PLANCK-INSTITUT
FÜR MOLEKULARE PHYSIOLOGIE

Mechanisms of Spatial and Temporal Regulation of Actin Dynamics

vorgelegt von

Ankit Animesh Roy

Dissertation zur Erlangung des akademischen Grades eines

Doktors der Naturwissenschaften (Dr. rer. nat.)

der Fakultät für Chemie und Chemische Biologie
der Technischen Universität Dortmund

Angefertigt am Max-Planck Institut für Molekulare Physiologie in Dortmund

June 2024

Tag der Abgabe der Dissertation: 31 Mai 2024

Von Ankit Animesh Roy

Erstgutachter	Prof. Dr. Philippe I. H. Bastiaens
Zweitgutachter	Prof. Dr. Jan Kierfeld

The work presented in this thesis was performed in the group of Dr. Peter Bieling in the Department of Systemic Cell Biology lead by Prof. Dr. Philippe I. H. Bastiaens at the Max Planck Institute of Molecular Physiology, Dortmund, Germany.

Dedicated to my parents, who have bestowed upon me the ultimate gift of education and made me oblivious to all limitations.

To my ma Jyoti, and in memory of my baba Animesh.

Acknowledgements

In this section it is customary to thank people who have positively influenced me during my PhD. I was planning to do just that until I fell into the rabbit hole of reminiscing figments of all the things that I've been part of during my time here as a PhD student. So instead, I've decided to share glimpses of a few things I'm most grateful for and the people that made it happen.

An acknowledgment section such as this would be incomplete without first mentioning the person who made it possible for me to even write my thesis today. I'm sincerely grateful to Peter who gave me the opportunity to work with our group. Despite the gamble of recruiting a computational biologist to an experimental biochemistry lab, he had faith in my ability to grow as a biochemist. Today, I'm a confident biochemist only because I could learn from his expertise, experiences and constant feedback.

A lab is nothing without the members that inhabit its spaces and make the magic of science happen. I was blessed to be part of a group of such ~~wizards~~ scientists with diverse talents and amazing personalities. You see, Peter wasn't the only reason why I'm a confident biochemist today, each member of my lab has taught me something crucial that is now part of my ~~thesis~~ personality and has made the journey more meaningful along the way.

Johanna and Lena showed me the ropes with everything actin. Ilaria always had a few tricks up her sleeve when I went asking for troubleshooting advice. Svenja is by far the coolest TA a lab could have. She has always helped a lot with large-scale purifications - every time I went to her and said, "Svenja", with a particular tone, she would know I was asking for a 24 L suspension culture. Apart from assisting me with all lipid-based experiments, Mike has also introduced me to plenty of bargains and the joy of bouldering! And tea, he makes so much of it! Yannic and I have the most engaging conversations about anything and everything. Since he has also been my flatmate, he has had to

bear me double time! There have often been times when we would be discussing why chaotic systems are deterministic and this would take precedence over the more pressing question of why the dishwasher is still not working.

The people in my lab aren't the only ones I'm grateful to. I've enjoyed my time in this department, sharing my time with individuals from all walks of life. Everyone in the department has always been welcoming of my random bouts of walking into their offices for no apparent reason other than to just have a quick chat. I would like to express my appreciation to Philippe for allowing me to be part of such a talented and inspiring group of people in the department.

I'd have to summon Peter once again to thank him for encouraging me to apply for the MBL advanced research courses. Without his suggestion, I would have never had the fun and knowledge that I acquired from the MBL@Deep Learning course. Little did I know how influential the time that I spent with the people at the course would be both in my professional and personal life. Coincidentally, it is also at this course where I met someone who completely hijacked my years of planning on which labs I'd like to be part of as a Postdoc only to find an even better one. I'll soon be joining this lab and I cannot be more excited to do so! It's funny how chance just flips the script, right when you think you've figured it all out.

To all my friends, you know who you are and you know how much I appreciate you all! Thanks for always having my back.

This is by no means an exhaustive list of people I'd like to thank and it's a shame that I have to draw an arbitrary line somewhere so you can finally read my thesis! However, I am sincerely grateful for each and every one of you who has made my life richer by sharing even a little bit of your time and space with me. There's so much that has happened over the course of these five years and I would be damned the day when my memory betrays me. I'm glad to be able to take this opportunity to pen some of the moments down that represent how colorful my time has been at this MPI. A PhD is tough but people and moments like these make it so much easier.

TLDR: In summary if I were to be trapped in a time vortex and found myself at the beginning of my PhD. I would happily do this all over again! :)

TLDR's TLDR: It was fun!

Contents

Title i

Dedication iv

Acknowledgements v

Contents ix

1 Abstract 1

2 Zusammenfassung 3

3 Introduction 5

3.1 The Actin Protein 5

3.2 Thermodynamics and Kinetics of Actin Polymerization 7

3.3 Mechanisms Regulating Actin Dynamics 12

3.3.1 Sequestration 13

3.3.2 Nucleation 14

3.3.3 Elongation 14

3.3.4 Capping 15

3.3.5 Aging 16

3.3.6 Severing 16

3.4 Branched Actin Networks 17

3.5 Nucleation Promoting Factors 18

4 Objectives 23

4.1 Mechanism of Inorganic Phosphate Release from the Actin Core 23

4.1.1 Actin Single Filament Polymerization Kinetics 23

4.1.2 Phosphate Release in Actin Mutants 24

4.2 Density Dependent Regulation of NPF Activity 24
4.2.1 *In vitro* Reconstitution of Branched Actin Nucleation 24
4.2.2 Membrane Recruitment of NPFs at Varying Densities 25
4.2.3 Comparing the Effects of NPF Densities with Dual NPF Binding to Arp2/3 Complex and Mother Filament Supplementation 25

5 Results **26**
5.1 Mechanism of Inorganic Phosphate Release 26
5.1.1 Evolution of nucleotide states in an ageing actin filament 26
5.1.2 Steric occlusion of the P_i release pathway 31
5.1.3 Instantaneous release of P_i from actin mutants 34
5.2 A Novel Density Dependent Mechanism of NPF Regulation 38
5.2.1 A metastable pool of actin and its nucleator 38
5.2.2 Overcoming metastability with membrane bound NPFs 44
5.2.3 Heterogenous distribution of NPFs in cells 46
5.2.4 Density controls NPF activity in a switch-like manner 48

6 Discussion and Conclusions **59**
6.0.1 Temporal control of P_i release 59
6.0.2 Spatial control of NPF activity 63

7 Materials and Methods **67**
7.1 Protein Purification 67
7.1.1 α-actin 67
7.1.2 β,γ-actin 68
7.1.3 Gelsolin (G4-6) 69
7.1.4 Profilin 69
7.1.5 Arp2/3 complex 70
7.1.6 Nucleation Promoting Factors 72
7.1.7 Capping Protein 73
7.1.8 Dark mCherry 74
7.2 Protein Labeling 74
7.2.1 Pyrene labeling 75
7.2.2 SNAP-tag based self-labeling 75
7.2.3 Maleimide labeling 76
7.3 NPF Dimerization 76

7.4 Mother Filament Stabilization 77
7.5 Lipid Preparations 78
7.5.1 Small Unilamellar Vesicles 78
7.5.2 Lipid Coated Beads 79
7.5.3 Embedding NPFs on beads 80
7.6 Biochemical Assays and Microscopy 80
7.6.1 Pyrene Assay 80
7.6.2 Bead Motility Assay 81
7.7 Data Analysis 82
7.7.1 NPF Density and Intermolecular Distance Calculation 82
7.7.2 Filament Length Tracking 82

References **85**

List of Figures **99**

List of Tables **101**

Acronyms **102**

A Source Code **107**
A.1 Stochastic Simulation of an Ageing Actin Filament 107

Affidavit **113**

1 Abstract

Actin subunits in filaments exhibit accelerated ATP hydrolysis compared to monomers. The subsequent slow phosphate (P_i) release results in an age-dependent distribution of ADP-P_i and ADP subunits within the filament. This stochastic process prevents newer regions from severing, as turnover occurs primarily in older sections rich in ADP subunits. However, the mechanism underlying P_i release from actin filament cores remains elusive. In the initial portion of this study, we present the mechanism responsible for P_i egress from actin filament cores. Our findings indicate that P_i can readily escape through a molecular backdoor in the terminal subunit which is largely occluded in the core of the filament. Utilizing molecular dynamics simulations, we identified potential egress pathways for the exit of P_i from filament cores. These escape pathways appeared to be obstructed by an intricate network of hydrogen bonding involving residues previously associated with disease-linked mutations. Lastly, our study demonstrates that disrupting this hydrogen-bonding network with actin mutants that confer an open-backdoor conformation results in increased P_i release in both bulk polymerization and single filament measurements.

The Arp2/3 complex initiates lamellipodial protrusions and endocytic actin patches through nucleation of force-generating branched actin networks. The activity of the Arp2/3 complex is regulated by Nucleation Promoting Factors (NPFs), characterized by a conserved C-terminal domain that activates the Arp2/3 complex and diverse N-terminal domains that exert spatial and temporal control over the NPFs. While some NPFs are autoinhibited and require the release of intramolecular autoinhibition by GTPases and phosphatidylinositol lipids for activation, others exhibit unclear regulatory mechanisms. Importantly, all NPFs assemble branched actin networks exclusively from cellular membranes. In the second section of this study, we propose a novel density-dependent mechanism for the regulation of NPF activity. We demonstrate that NPFs recruited to the membrane can spawn a branched actin network from a pool of profilin-actin

under physiological concentrations of Arp2/3 complex and capping protein, whereas NPFs in solution cannot. Moreover, the nucleation process shows a switch-like response to membrane-bound NPF density, with nucleation only occurring above a threshold density. The concentration of capping protein can further tune this density-dependent response of NPF activity. Our findings suggest that this density-dependent regulation operates on NPFs regardless of autoinhibition, thus superseding the traditional autoinhibition mechanism.

2 Zusammenfassung

Aktin Untereinheiten in Filamenten weisen im Vergleich zu Monomeren eine beschleunigte ATP-Hydrolyse auf. Die anschließende langsame Freisetzung von inorganischem Phosphat (P_i) führt zu einer altersabhängigen Verteilung von ADP-P_i und ADP-gebundenen Aktin Untereinheiten innerhalb des Filaments. Dieser stochastische Prozess verhindert, dass neu polymerisierte Filamentregionen abgebaut werden und der Abbau hauptsächlich in älteren Teilen von Aktinfilamenten stattfindet, welche reich an ADP-Untereinheiten sind. Der biochemische und strukturelle Mechanismus, welcher die Phosphatfreisetzung aus Aktinfilamenten kinetisch kontrolliert, ist jedoch weitgehend unbekannt. Im ersten Teil dieser Arbeit studiere ich den Mechanismus, welcher für die Freisetzung von Phosphat verantwortlich ist. Unsere Ergebnisse zeigen, dass Phosphat durch eine molekulare Hintertür in der terminalen Untereinheit schnell entweichen kann, welche in Untereinheiten im Filamentinneren überwiegend blockiert ist. Durch die Nutzung von Molekulardynamik-Simulationen identifizieren wir potenzielle Austrittswege von Phosphat in Untereinheiten im Filamentinneren. Diese Austrittswege sind durch ein komplexes Netzwerk von Wasserstoffbrückenbindungen blockiert, die durch von Aminosäuren gebildet werden, welche zuvor mit krankheitsbezogenen Mutationen in Verbindung gebracht wurden. Die Störung dieses Netzwerkes aus Wasserstoffbrücken durch solche Aktinmutationen öffnet den Ausstrittsweg über die molekulare Hintertür, was zu erhöhten Raten der Phosphatfreisetzung führt, welche ich über verschiedene biochemische Methoden nachweise.

Der Arp2/3-Komplex initiiert lamellipodiale und endozytische Aktinstrukturen durch die Nukleation von krafterzeugenden, dendritischen Aktinnetzwerken. Die Aktivität des Arp2/3-Komplexes wird durch Nukleationsföordernde Faktoren (sogenannte NPFs) reguliert, welche durch eine konservierte C-terminale Domäne den Arp2/3 direkt binden und aktivieren, wogegen verschiedene N-terminale Domänen die räumliche und zeitliche Kontrolle der NPFs gewährleisten. Wähhrend einige NPFs autoinhibiert sind und ihre

Aktivierung eine Membranrekrutierung durch kleine GTPasen und Phosphatidylinositol-Lipide erfordert, besitzen andere NPFs unbekannte regulatorische Mechanismen. Jedoch ist die Aktivität aller NPFs räumlich an zelluläre Membranen beschränkt. Im zweiten Abschnitt dieser Arbeit erarbeite ich einen neuen dichteabhängigen Mechanismus zur Regulierung der NPF-Aktivität. Ich zeige, dass an NPFs unter physiologisch realistischen Bedingungen in der Anwesenheit von Profilin und Capping Protein nur ausgehend von Membranen, nicht aber in Lösung, den Arp2/3 Komplex aktivieren können. Ferner zeige ich, dass der Nukleationsprozess in einer nicht-linearen Weise von der Dichte der membrangebundenen NPFs abhängt, wobei die Nukleation erst oberhalb einer Schwellendichte zu beobachten ist. Die Konzentration des Capping-Proteins kann die diese Dichteabhängigkeit regulieren. Unsere Ergebnisse zeigen, dass die Regulierung über Oberflächendichte einen entscheidenden Beitrag zu Kontrolle von NPFs darstellt, welche vermutlich bedeutsamer ist als der traditionelle Mechanismus der intramolekaren Autoinhibition.

3 Introduction

3.1 The Actin Protein

Actin is one of the most abundant and conserved proteins found in eukaryotic cells [1, 2, 3]. This small, globular protein is an ATPase [4] and can transition between a monomeric and polymeric state [5]. Actin plays essential roles in various cellular and tissue functions, including maintaining a cell's shape and polarity [6, 7], facilitating motility [8], enabling muscle contraction [9], and regulating transcription [10]. Its versatility to perform these functions arises from its unique ability to interact differentially with multiple proteins in the cell, depending on its monomeric or polymeric state [5]. Three distinct actin isoforms, namely α, β, and γ, exist in human cells [11]. Muscle-specific variants of the α isoform include those found in skeletal muscles (α-skeletal, ACTA1), aortic smooth muscles (α-smooth, ACTA2), and cardiac muscles (α-cardiac, ACTC1). The cytoplasm of all cells contains the β (ACTB) and γ (ACTG1) isoforms, with an additional variant of γ actin (γ-smooth, ACTG2) existing in enteric smooth muscles [3, 12]. The β and γ actin isoforms differ by only a few amino acids towards the N-terminus [11].

Cytoplasmic actin polymerizes into networks of parallel or branched filaments that generate higher order structures, such as the cell cortex, focal adhesion stress fibers, transverse arcs, lamellipodia, and filopodia [13]. These structures appear in various cellular locations, collaborating to sustain a cell's structure by proving mechanical resistance to the cytoplasm, generating polarized tracks for intracellular transport and promoting cellular motility (fig. 3.1). Protrusive actin network structures such as lamellipodia and filopodia generate pushing forces at the leading edge of a migrating cell [14, 15], while contractile structures such as the cell cortex, transverse arcs, and focal adhesion-associated stress fibers help maintain the rigidity of the cell membrane and are responsible for trailing edge retraction during the movement of the cell [16, 17, 18]. Examining the ultrastruc-

ture of these actin networks, one might perceive actin as a static molecule present either as monomers or filaments. However, this perception is misleading, as we will discover in the forthcoming sections that actin exhibits a highly dynamic nature and is constantly in flux between the two states due to its constant turnover, which is a result of its intrinsic polymerization kinetics, that are tightly regulated by interactions with other proteins.

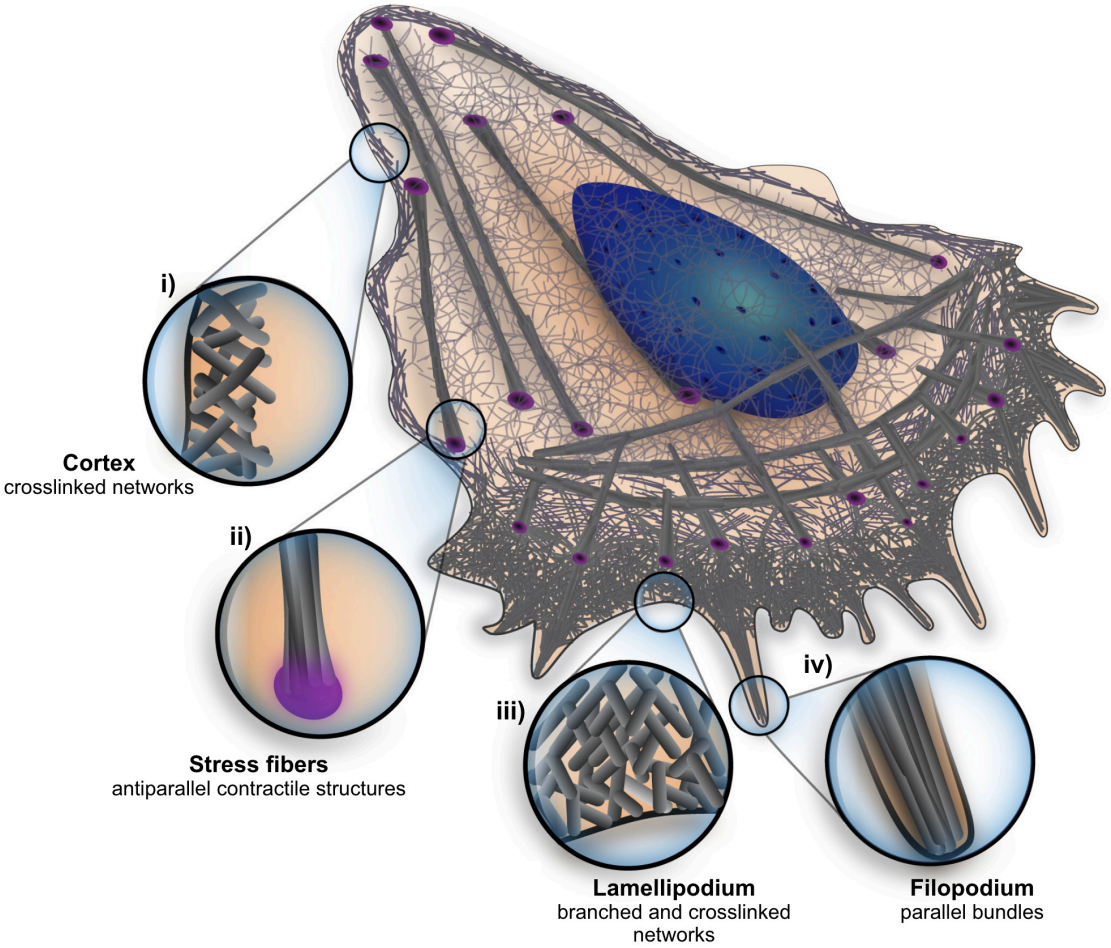

Figure 3.1: Schematic illustration of the distinct actin networks found within a cell: i) cortex, ii) stress fibers, iii) lamellipodia, and iv) filopodia. Adapted from [13].

3.2 Thermodynamics and Kinetics of Actin Polymerization

Actin polymerizes into filaments and converts chemical energy into mechanical force, facilitating membrane protrusion [16, 19]. Actin molecules initiate filament formation through an energetically unfavorable nucleation step, which is subsequently followed by a favorable polymerization step [20, 21, 22]. The rate of actin polymerization can be expressed as in eq. (3.1).

$$\frac{d[M_f]}{dt} = -\frac{d[M_g]}{dt} = k_+[F][M_g] - k_-[F] \tag{3.1}$$

where, $[M_f]$ is the concentration of actin monomers in filaments, $[M_g]$ is the concentration of monomeric actin, $[F]$ is the concentration of filaments, k_+ is the polymerization rate constant and k_- is the depolymerization rate constant. Since actin polymerization is a reversible process, the rate of polymerization and depolymerization are equal at equilibrium and the concentration of monomeric actin at equilibrium is known as the critical concentration of actin [22, 23]. This can be expressed as in eq. (3.2).

$$K_{eq} = \frac{k_+}{k_-} = \frac{1}{[M_g]_{eq}} = \frac{1}{C_c} \tag{3.2}$$

where, K_{eq} is the equilibrium constant, $[M_g]_{eq}$ is the concentration of monomeric actin at equilibrium which is also referred to as the critical concentration of actin C_c.

Actin spontaneously nucleates and polymerizes above its critical concentration. The nucleation process begins with the formation of a stable trimeric nucleus [24, 25], which can then be elongated to form a filament. Once an actin filament has nucleated, it can be extended on both ends (barbed end and pointed end), but the rates of extension as well as the solvent accessible surfaces of the two ends are not identical. Specifically, the barbed end exhibits faster polymerization and depolymerization kinetics compared to the pointed end [26, 27].

Actin filaments exhibit variable polymerization and depolymerization rates that depend on not only on the concentration of available monomers and the identity of the two

ends but also the nucleotide state of the terminal subunits. Since actin is an ATPase, its subunits can either exit in the ATP state [28] or in the ADP state when the nucleotide is hydrolyzed [29]. Additionally, the actin subunits can also exist in a third state when the nucleotide has been hydrolyzed but the inorganic phosphate has not yet been released from the subunit (ADP-P_i) [26]. These different nucleotide states at each end of the actin filament give rise to six distinct polymerization and depolymerization rates that have been previously been determined experimentally (table 3.1).

Table 3.1: Kinetic rate constants and critical concentrations of actin at the different ends of the filament and for different nucleotide states [26, 27].

Filament End	**Nucleotide**	k_+ ($\mu\mathbf{M}^{-1}\mathbf{s}^{-1}$)	k_- ($\mathbf{s}^{-1}$)	C_c (μM)
Barbed End	ATP	11.60	1.40	0.12
	ADP-P_i	3.40	0.20	0.06
	ADP	2.90	5.40	1.80
Pointed End	ATP	1.30	0.80	0.62
	ADP-P_i	0.11	0.02	0.14
	ADP	0.14	0.25	1.80

At steady state, actin filaments can polymerize at their barbed ends while depolymerizing at their pointed ends, resulting in growth at the barbed end due to monomers released from the pointed ends. This process, driven by differences in critical concentrations at the two ends and nucleotide hydrolysis, is referred to as actin treadmilling (fig. 3.2) [30, 31]. Once a subunit depolymerizes from the pointed end, it can exchange its nucleotide with an ATP molecule before polymerizing at the barbed end [32]. In the absence of other binding proteins, this phenomenon occurs above the critical concentration of the barbed end ($C_c^{BE:ATP} = 0.12$ μM) and below that of the pointed end ($C_c^{PE:ATP} = 0.62$ μM, $C_c^{PE:ADP} = 1.8$ μM) [33, 34]. These concentrations are in the sub-micromolar range, which is significantly lower than the actin concentrations observed in cells (100 – 150 μM) [2, 35, 36]. In cells, actin binds to a variety of proteins that influence its polymerization dynamics and give rise to a modified form of treadmilling coupled with turnover, a topic I will cover in the following section and which has major implications in force generation at the leading edge of motile cells.

The polymerization of actin generates force that can be utilized to push against a membrane. This force originates from monomer binding at the barbed end and, indirectly,

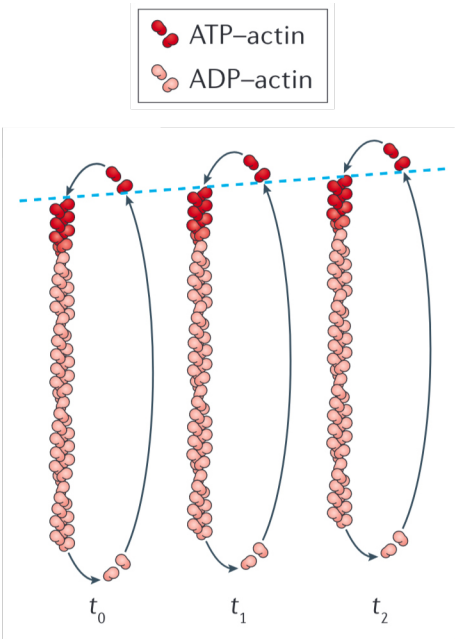

Figure 3.2: Schematic representation of actin treadmilling. The scheme illustrates ATP-actin polymerizing at the barbed end (red) and ADP-actin depolymerizing at the pointed end (light red) at three consecutive timepoints in a timeseries. The dashed blue line indicates the growth at the barbed end, and the slope of this line denotes the treadmilling rate. Adapted from [31].

from maintaining the treadmilling cycle through ATP hydrolysis. The free energy stored in unbound actin monomers can be estimated with eq. (3.3).

$$\Delta G = -k_B T \ln \frac{[M_g]}{C_c} \tag{3.3}$$

where, ΔG is the stored Gibbs free energy, k_B is the Boltzmann's constant, T is the absolute temperature. Upon monomer binding, this free energy can be converted into pushing force. The equilibrium stall force that can be obtained from a pool of unbound actin monomers can be estimated with eq. (3.4) [37].

$$F_{eq} = \frac{k_B T}{\delta} \ln \frac{[M_g]}{C_c} \tag{3.4}$$

where F_{eq} is the equilibrium stall force and δ is the incremental length extension of the filament in the direction of the force upon addition of an actin monomer. Since the filament might grow obliquely from the direction of the force, δ is a function of the

incidence angle of the filament θ, such that $\delta = \delta_0 \cos\theta$, where δ_0 is 2.7 nm, equivalent to the rise in an actin filament per subunit addition [19].

What is immediately clear from eq. (3.3) and eq. (3.4) is that the free energy of binding and consequently the equilibrium stall force are both directly proportional to the concentration of free actin monomers ($[M_g]$). Although the concentration of actin in cells is high, the amount of free actin is surprisingly low (< 2 μM, [38]). This is because actin is partitioned between filaments and sequestering proteins that bind to monomeric actin. Despite the negligible concentration of free actin, a large fraction of unpolymerized actin bound to other proteins can participate in polymerization at the barbed end and therefore contribute to the free energy. This fraction of polymerizable actin could be as much as 50 - 100 μM in cells [2, 38], which translates to stall forces of roughly 10 - 20 pN.

One of the first attempts to unify the thermodynamics of the free energy stored in the pool of actin that can polymerize with the kinetics of growing actin filaments generating force on the membrane was made by Hill [37]. He proposed a model relating the filament polymerization rate (r) to the free energy (ΔG) and the force generated on the membrane (F) as described in eq. (3.5).

$$\begin{aligned} r &= k_+ C_c e^{-fF\delta/k_BT} - k_- e^{(1-f)F\delta/k_BT} \\ &= k_- e^{(1-f)F\delta/k_BT} \left(e^{-\Delta G - F\delta/k_BT} - 1\right) \end{aligned} \tag{3.5}$$

where, f is a dimensionless parameter that expresses the split of the work done to push against the membrane ($F\delta$) between the polymerization rate ($k_+[M_g]$) and the depolymerization rate (k_-). This model assumes that actin filaments are always attached to the motile surface, which is not the case in cells. To account for actin filaments generating force on the membrane without being physically attached to it, the "Brownian Ratchet" model was proposed (eq. (3.6), [39]). This model also accounts for thermal fluctuations and membrane deformations that might open up enough of a gap for the addition of a new subunit.

$$r = k_+ C_c \int_{\delta}^{\infty} p(x)dx - k_- \tag{3.6}$$

where, $p(x)$ is probability density for opening a gap of distance x and can be solved as in eq. (3.7) as the solution to the Boltzmann density of $p(x)$ at stead-state.

$$p(x) = \frac{e^{-U(x)/k_BT}}{\int_0^\infty e^{-U(x)/k_BT} dx} \tag{3.7}$$

In the "Brownian Ratchet" formulation, the actin filament does not need to be attached to the motile surface directly. Instead, the polymerization rate is only affected by the gap opening probability density $p(x)$. Furthermore, $p(x)$ can account for the filament end's search process to find an optimal gap with potential energy, $U(x)$, which is equivalent to that of the opened gap under a constant force, $U(x) = Fx$, or for a spring-like filament end with $U(x) = \kappa(x - x_0)^2$, where κ is the stiffness and x_0 is the equilibrium position of the filament end [19].

The "Brownian Ratchet" model can sufficiently explain force generation at the membrane without requiring actin filaments to be directly attached [39]. However, it fails to account for cases where particles are propelled via actin filaments or the deformation of vesicles that spawn an actin network. Multiple studies have reported the actin-mediated propulsion of *Listeria monocytogenes* inside cells [40, 41, 42] and this persistently pushing force requires some actin filaments to be attached to the surface of the bacteria. Furthermore, actin networks spawned on lipid vesicles generate tensile forces that deform the vesicle [43]. This could only happen if at least a fraction of the actin filaments are attached to the vesicle. A new model, known as the "Tethered Brownian Ratchet" was proposed to further expand the "Brownian Ratchet" model and explain these observations [19, 44]. The main premise of this model is to assume that forces generated by actin networks are due to a population of attached filaments and unattached filaments across which the load is distributed as described in eq. (3.8).

$$F_L + \langle F_a \rangle a = F_w \tag{3.8}$$

where, F_L is the load on the motile surface, $\langle F_a \rangle$ is the load on attached filaments averaged over time, a is the number of attached filaments and F_w is the load on the total working filaments. At any given point in time the population of attached (a) and working filaments (w) can be deduced from the nucleation rate (n, rate at which new

filaments are generated), rate of filament detachment (k_d) and capping rate (k_c, rate at which filaments are capped and prevented from further extension) as given by eq. (3.9).

$$n = k_d a = k_c w \tag{3.9}$$

Additionally, the time-averaged load on attached filaments can be estimated using the filament stiffness (κ), filament extension rate (V), and the time-averaged detachment probability ($\langle t \rangle$) as shown in eq. (3.10). Since actin filaments are semi-flexible polymers [45], they are treated as Hookean springs with a stiffness of approximately 1 pN/nm, and the growth velocity of the filament is estimated using Hill's model ($V = r\delta_0 \cos\theta$). $\langle t \rangle$ is calculated from the detachment time probability density, $p(t)$, which is a function dependent on the detachment rate constant, k_d, and further scales with the load on attached filaments in comparison to the force of the attachment bond (see [19] for details).

$$\begin{aligned} \langle F_a \rangle &= \kappa V \langle t \rangle \\ &= \kappa V \int_0^\infty t\, p(t) dt \end{aligned} \tag{3.10}$$

As you may have realized by now, actin is a highly dynamic protein that utilizes its kinetic asymmetry at the two ends of filaments and the potential energy stored in the polymerizable pool of actin to generate the force necessary for membrane protrusion. Nevertheless, these processes are further regulated by proteins that bind to actin, either in its monomeric or polymeric state, and modify various kinetic parameters that contribute to force generation. In the following section, I will describe the mechanisms through which actin dynamics are regulated and the proteins involved in this process.

3.3 Mechanisms Regulating Actin Dynamics

Alongside the inherent kinetic regulatory mechanisms, actin is regulated by numerous proteins that bind to it, controlling diverse processes like nucleation, elongation, branching, branch termination, severing, and annealing. In this section, I will delve into some

of the essential proteins participating in these functions and how they collaborate to orchestrate actin dynamics.

3.3.1 Sequestration

Monomeric actin spontaneously nucleates and polymerizes above its critical concentration of 0.12 μM. However, cells have significantly higher concentrations of actin (approximately 100-150 μM) [2]. To prevent spontaneous nucleation, cells have proteins such as β-thymosin and profilin that bind to monomeric actin. Both these proteins interact with monomeric actin; however, they do so with significantly different affinities and behave differently upon binding. β-thymosin forms a highly enlongated strucuture that encircles the actin monomer to block all major interaction interfaces necessary for filament formation and binds to monomeric actin with micromolar affinities [46]. Profilin is a globular protein that binds with nanomolar affinity to the barbed end face of the actin monomer, leaving the pointed end free [47].

An important functional distinction is that profilin-bound actin can take part in polymerization at the barbed end of filaments, while β-thymosin-bound actin cannot and therefore constitutes a passive reservoir of soluble actin [48]. Notably, profilin and β-thymosin share partially overlapping binding sites and therefore compete for binding to soluble actin. The difference in affinity is thought to drive the rapid regeneration of profilin-actin from complexes with β-thymosin once free profilin is liberated from the barbed ends of actin filaments in the process of polymerization. Additionally, profilin accelerates the nucleotide exchange of bound actin monomers and replenishes the pool of ATP-bound actin [49].

Profilin is one of the most conserved actin regulators, since it is - unlike many other actin binding proteins - ubiquitously found in every eukaryotic organism. Its central role is to maintain a large pool of polymerizable actin monomers that is refractory to spontaneous nucleation. This kind of metastability will become apparent in the second part of this thesis.

3.3.2 Nucleation

Actin nucleation is energetically unfavorable, and cells utilize various proteins to facilitate this process. There are three primary classes of nucleators [50] that differ in their mode of nucleation:

Class I nucleators, such as the Arp2/3 complex and its associated Nucleation Promoting Factors (NPFs) that activate it, make up this class. The Arp2/3 complex initiates filament growth through structural mimicry of a trimeric nucleus. It is unique in generating branched actin networks which are a major topic of this thesis. Instead of providing a detailed explanation of the Arp2/3 complex and its activating NPFs here, I will discuss them in more depth within the biochemical context of branched actin networks, the actin network structure that these proteins assemble [51].

Class II nucleators, like Diaphanous (DIA) [52], formins (FMN) [53], and inverted formins (INF) [54] families, stabilize spontaneously formed actin dimers. These proteins are characterized by the presence of conserved FH (Formin Homology) domains, by which they nucleate actin filaments and processively track the elongating barbed end actin filaments [55]. The latter is crucial for their actin elongation or polymerase activity as discussed in the following section. Similar to the activation of the Arp2/3 complex, formins are generally inactive in the cytoplasm and only locally activated at cellular membranes in response to signaling.

Class III nucleators comprise proteins containing three or more actin binding domains. They increase the frequency of nucleation by binding to multiple actin monomers with their WH2 or Leu-rich repeat (LRR) domains. This class of proteins include Spire [56], cordon-bleu (COBL) [57], and leiomodin families of proteins [58].

3.3.3 Elongation

Once a filament has been nucleated, it can freely elongate until either the actin pool is depleted or its end is capped by various capping proteins. Proteins known as elongators protect the barbed end from capping and, in some instances, enhance polymerization rates. This class includes formins and Ena/VASP proteins [50].

Formins, as previously mentioned, are not only nucleators but also function as elongators once a filament is initiated. After nucleation, the formin protein processively travels with the growing filament end and adds actin subunits by recruiting profilin-actin using their FH1 domains. Formins create donut-shaped dimers with their FH2 domain and rope-like extensions made up of their FH1 domains, which recruit profilin-actin from the surroundings. Unlike formins, Ena/VASP proteins do not initiate nucleation but rather elongate existing filaments by recruiting either actin or profilin-actin through their tetramerization [59].

3.3.4 Capping

Capping is an essential aspect of actin regulation because filaments do not grow indefinitely after nucleation. Excessively long filaments would be detrimental for force production due to their low buckling force. In addition, their disproportionate elongation would rapidly deplete the soluble actin pool.

The heterodimeric actin capping protein (CP) plays a vital role in regulating actin filament elongation by binding to the barbed ends of free actin filaments and preventing the addition of further actin subunits. The interaction between CP and the filament barbed end is very strong with sub-nanomolar affinity and kinetically very stable. Capped filaments are therefore refractory to further growth and destined to undergo disassembly after some time [60].

In addition to CP, various other proteins, including members of the gelsolin family [61], adducins [62], and epidermal growth factor receptor kinase substrate 8 (EPS8) [63], possess barbed-end capping activity. While CP serves as the most widespread and abundant barbed-end capper, other capping proteins have more specialized roles, characterized by specific cell and tissue expressions and unique modes of regulation [64].

Recent studies have revealed several molecules that interact with CP, influencing its capping activity. The significance of these interactions remains a crucial area of investigation.

3.3.5 Aging

Actin subunits hydrolyze their bound ATP at any given time and can exit in either an ATP-bound, ADP-Pi-bound, or ADP-bound state. Monomeric actin subunits exhibit slow hydrolysis rates. Furthermore, monomeric subunits with hydrolyzed nucleotides quickly exchange into ATP-bound states due to the high ATP concentrations in the cytoplasm of cells (millimolar levels [65]) and enhanced nucleotide exchange from the majority of actin being bound to profilin. However, this is not the case for actin filaments. The hydrolysis rate accelerates upon incorporation of a subunit into a growing filament, while the incorporated subunits do not readily exchange their nucleotide with the cytoplasmic pool. Consequently, the distribution of nucleotide states in a growing actin filament evolves with its age. Older parts of the filament are rich in ADP-bound subunits, whereas newer parts are formed from ATP-subunits that rapidly hydrolyze their nucleotide to transition into ADP-Pi-subunits retaining their bound P_i before eventually becoming ADP-bound. Due to a half-life of P_i release exceeding 100 seconds, actin filaments develop an ADP-P_i cap that advances with the growing end of the filament [66]. Recent work investigating the mechanism by which P_i is retained for such prolonged timescales will be discussed in the first part of this thesis.

3.3.6 Severing

Central to actin disassembly are proteins of the Actin Depolymerizing Factor (ADF)/cofilin family. These proteins selectively target aged, predominantly ADP-containing subunits within actin filaments. Binding of ADF/cofilin is a highly cooperative process that results in drastic changes in the actin subunit packing within the filament, which destabilizes interactions between neighboring subunits. This leads to the severing of actin filaments into smaller fragments, increasing the number of ends available for disassembly [67].

However, ADF/cofilin proteins do not work in isolation. Instead, they synergize with other proteins such as Coronin, actin-interacting protein 1 (AIP1), and cyclase-associated protein (CAP), which exert specific biochemical roles in the severing process [68].

3.4 Branched Actin Networks

Branched actin networks, also known as dendritic networks, are characterized by a distinctive ultrastructure derived from y-shaped, branched actin filaments that create propulsive forces at the leading edge of membrane protrusions in motile cells [69]. The assembly of these structures is initiated by the activity of a single protein complex called the Arp2/3 complex [70]. By nucleating a new filament (daughter filament) from an existing filament, commonly referred to as the mother filament, the Arp2/3 complex generates dendritic structures. Importantly, the Arp2/3 complex mediates the physical connection between the pointed end of the daughter to the side of the mother filament. It is therefore not only a nucleator, but also an important crosslinking protein. The daughter filament emerges at a canonical angle of 70° from the branch point, relative to the pre-existing filament (fig. 3.3) [71]. Because branched filaments are always born from preexisting filaments, they inherently generate forces as they remain connected to the entire branched actin network while propelling the membrane forward [72].

The Arp2/3 complex is a seven-subunit protein comprised of two subunits, Arp2 and Arp3, which act as pseudoactin dimers to initiate nucleation [74]. The remaining seven subunits function as scaffolding units, maintaining the complex structure and interacting with the mother filament [75]. In the cytoplasm, however, the Arp2/3 complex remains inactive with its two subunits, Arp2 and Arp3, splayed apart [76]. A class of proteins known as nucleation-promoting factors (NPFs) is required to activate this complex [77]. NPFs perform three major functions in initiating nucleation from the Arp2/3 complex: 1) They bind and induce a conformational change that brings the two Arps together; 2) They deliver an actin molecule to the pseudoactin dimer of the activated Arp2/3 complex; 3) They facilitate the complex's binding to the mother filament.

Many proteins interact with the branched actin network to either stabilize it or destabilize it. Cortactin is known to stabilize branched actin networks and enhance the persistence of lamellipodia [78]. Conversely, proteins such as Coronin [79], Arpin [80], GMF [81] and gadkin [82] inhibit the Arp2/3 complex, destabilize branch points, or promote debranching. The interplay between these proteins, along with the aging of filaments and severing by proteins like ADF/Cofilin, forms an intricate network of interactions, kinetic and spatio-temporal regulations that constantly remodels the branched actin network throughout the cell.

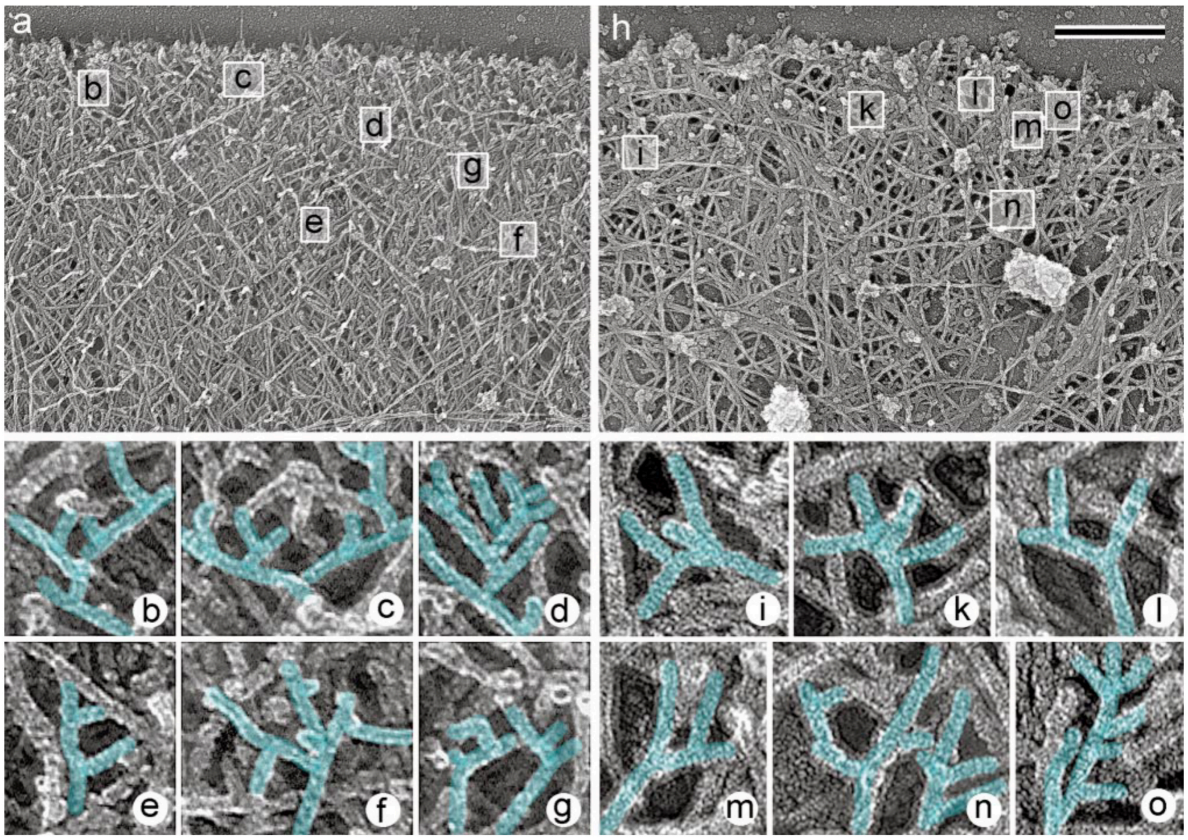

Figure 3.3: Electron micrographs show branched actin networks at the leading edge of *Xenopus* keratocytes (a) and fibroblasts (h). Enlarged regions from sections of the leading edge on the keratocyte are presented as b-g, while i-o illustrate similar details from the fibroblast's leading edge. Scale bar represents 0.5 μm. Adapted from [73].

3.5 Nucleation Promoting Factors

The Arp2/3 complex exists in an inactive state in its basal condition and requires activation by proteins referred to as Nucleation Promoting Factors (NPFs). Two primary classes of NPFs exist, differing in the mechanisms through which they activate the Arp2/3 complex [83].

Class I NPFs are characterized by their ability to bind both monomeric actin and the Arp2/3 complex for its activation. Examples include WASP and N-WASP (neuronal-WASP); WAVE1, WAVE2, and WAVE3 (Wiskott Aldrich Syndrome Protein and Verprolin Homologue, also known as SCAR for suppressor of cAMP receptor); WASH (Wiskott-Aldrich Syndrome Protein and SCAR homologue); WHAMM (WASP homolog

associated with actin, membranes and microtubules) and JMY(junction-mediating and -regulatory protein); and the recently discovered WHIMP [84, 85, 51, 86, 87, 88]. Class I NPFs are highly potent and can nucleate branched filaments at nanomolar concentrations. They activate the Arp2/3 complex through binding to conserved C (Central) and A (Acidic) domains [89].

Class II NPFs are identified by their ability to bind both filamentous actin and the Arp2/3 complex for its activation, include proteins such as Cortactin, Abp1, and Pan1 [90, 91, 92]. Class II NPFs are less potent activators of the Arp2/3 complex compared to class I NPFs. Their mechanism of activating the Arp2/3 complex remains unclear, furthermore, they possess only the A domain.

A new class of NPFs, called WDS proteins, interact directly with the Arp2/3 complex to activate it without binding to either monomeric or filamentous actin [93]. This interaction occurs at a site that overlaps with the mother filament binding sites, leading to activated Arp2/3 complex molecules that cannot be incorporated into branched actin networks. Instead, they promote the growth of linear actin filaments [94].

Class I NPFs within the WASP family of proteins, including various isoforms of WASP, NWASP, and WAVE, are the most canonical nucleators [95, 96]. They share similarities in domain organization while maintaining a diverse overall sequence. The family is characterized by the presence of a conserved C-terminus, that constitutes the region harboring functions related to actin nucleation. The NPF C-terminus commonly consists of a Verprolin homology domain (also known as the WH2 or WASP-homology-2 domain), C (Central or Cofilin homology) domain, and A (Acidic) domain. As mentioned before, the CA domain is necessary for Arp2/3 complex binding and activation. The WH2 domain is also strictly required for nucleation and facilitates the transfer of an actin monomer binding to the bound Arp2/3 complex during the nucleation process [96, 89].

These proteins also contain a proline-rich domain that binds to profilin-actin complexes and other SH3 domain containing proteins. Profilin recruitment via proline rich-domains is a common functional element in actin nucleating and elongating factors such as NPFs, formins and Ena/VASP proteins. Because profilin-actin constitutes the major source of polymerizable actin in cells, it is not surprising that these factors have evolved the means to efficiently recruit and utilize soluble profilin actin complexes for their respective

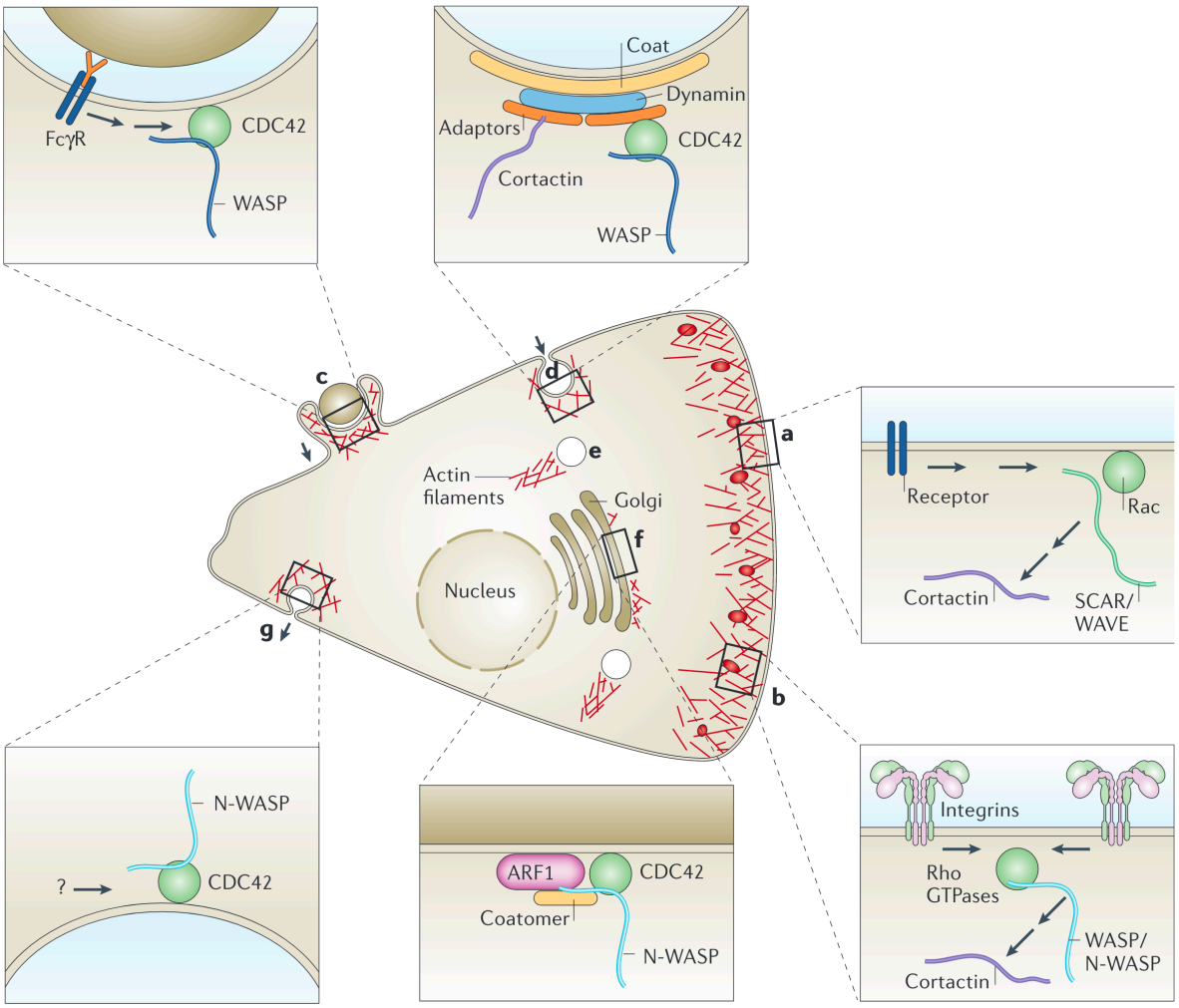

Figure 3.4: Schematic representation of the branched actin networks formed using Class I NPFs in various locations and their roles in diverse biological functions. (a) WAVE/SCAR mediated lamellipodial protrusion, (b) WASP/N-WASP mediated podosome formation, (c) WASP mediated phagocytosis, (d) WASP mediated endocytosis, (e) motility of vesicles and organelles, (f) N-WASP mediated Golgi trafficking, and (g) N-WASP mediated exocytosis. Adapted from [83].

function. In NPFs the proline-rich domain collaborates with the downstream WH2 domain for efficient monomer transfer to the Arp2/3 complex [97, 98].

Alongside their conserved C-terminal domains, WASP family proteins harbor a divergent set of N-terminal domains that are responsible for either the incorporation into larger multi-protein complexes and/or for regulation. WASPs and WAVEs form protein complexes—the WIP-WASP complex and the WAVE Regulatory Complex (WRC), respectively. These proteins are autoinhibited via intramolecular or intermolecular interactions with components of their respective complexes, shielding the VCA domain and rendering it inaccessible to activate the Arp2/3 complex [99]. Both classes of proteins relieve their autoinhibition through activation by small GTPases: Cdc42 for the WIP-WASP complex, and Rac for the WRC [100, 101, 102]. Moreover, they require binding to members of the PIP lipid species, PI(4,5)P_2 for the WIP-WASP complex and PI(3,4,5)P_3 for the WRC complex, respectively, to become fully active [103]. As a consequence of their divergent molecular inputs, these proteins execute distinct biological functions and are localized at different regions of the cell. For instance, certain WASP isoforms contribute significantly to endocytic vesicle formation and are recruited to clathrin-coated pits. In contrast, the WRC is primarily associated with the leading edge of motile cells, responsible for generating protrusive lamellipodia (fig. 3.4) [104, 105].

Even though significant progress has been made in understanding the mechanisms of NPFs over the past decade, a clear understanding of how their activity is regulated is still lacking. For instance, autoinhibition in the WIP-WASP complex and the WRC prevents unintended nucleation in the cytoplasm and enables controlled nucleation at sites of membrane recruitment. However, not all NPFs are autoinhibited. For example, Las17, a WASP homolog in yeast, does not exhibit autoinhibition and instead is fully capable of activating the Arp2/3 complex *in vitro*, but still only activates the Arp2/3 complex at the plasma membrane in the cellular context. Similarly, the mammalian NPFs WHAMM and JMY appear to lack autoinhibitory elements. This raises questions about how NPF activity can be licensed to occur only at cellular membranes even in the absence of autoinhibition.

Recent Cryo-EM structures of the Arp2/3 complex have revealed two orthogonal NPF binding sites. Moreover, it has been reported that dimeric NPFs are more effective nucleators than monomeric variants. However, the significance of simultaneously binding

two NPFs to the same complex is not fully understood since a single NPF can already promote Arp2/3 activation.

Lastly, a recent study on Las17 revealed a switch-like mechanism for endocytic branched actin assembly. This mechanism is only activated when Las17 levels exceed a threshold level, exhibiting minimal activity below it. Collectively, these findings highlight the importance of further investigating NPF regulation mechanisms that can reconcile these disparities. In my thesis, I propose a novel density-dependent NPF regulation mechanism that does not rely on autoinhibition and mimics switch-like thresholding behavior in nucleation activity.

4 Objectives

4.1 Mechanism of Inorganic Phosphate Release from the Actin Core

The primary objective of the initial section of my thesis was to elucidate the mechanism by which P_i is released from the core of actin filaments following the hydrolysis of ATP upon the addition of an actin subunit to a growing filament.

4.1.1 Actin Single Filament Polymerization Kinetics

Actin filaments polymerized from ATP-actin quickly hydrolyze their bound nucleotide. After nucleotide hydrolysis, the actin subunit retains the P_i for a short period before its release, resulting in the subunit subsequently being bound to an ADP molecule. The process of ATP hydrolysis and subsequent P_i release is stochastic, and the distribution of different nucleotide states along the filament does not form distinct boundaries. However, due to the rapid rate of ATP hydrolysis and slower release of P_i, actin filaments growing from a pool of actin-ATP have an ADP-P_i cap near the newer parts and ADP in the older parts. Since the rates of polymerization and depolymerization depend on the nucleotide state of the terminal subunit, I aimed to deduce the rate of P_i release as a function of changes in depolymerization velocities measured from length changes observed in individual filaments. To accomplish this goal, I conducted microfluidics-assisted single filament polymerization and depolymerization experiments.

4.1.2 Phosphate Release in Actin Mutants

The rate of P_i release from the terminal subunit is faster than that observed in the interior of actin filaments. We aimed to investigate the structural differences in the conformation of actin subunits, specifically at the filament end versus the interior, which might explain the disparities in P_i release rates. Furthermore, we intended to identify potential exit pathways for P_i from the filament core and pinpoint key residues that accelerate P_i egress, thus facilitating a more thorough understanding of the mechanism governing P_i release from actin filaments. Lastly, I sought to identify critical residues whose mutation accelerates the transition from an ADP-P_i state to the ADP-bound state in actin depolymerization, thereby corroborating their role in regulating the slow P_i release from the filament core.

4.2 Density Dependent Regulation of NPF Activity

The primary objective of the second portion of my thesis was to unravel the underlying mechanism explaining how NPF recruitment onto the plasma membrane controls Arp2/3 complex-mediated branched actin nucleation.

4.2.1 *In vitro* Reconstitution of Branched Actin Nucleation

Branched actin nucleation in cells is mediated through the Arp2/3 complex, however, the Arp2/3 complex is heavily regulated to prevent nucleating branched filaments in the cytoplasm. To investigate the regulatory mechanisms of branched actin nucleation in cells, I aimed to carry out *in vitro* reconstitution of a minimal system for branched actin nucleation that closely mirrors the physiological conditions within cells. The objective was to reconstitute actin nucleation from a pool of profilin-sequestered actin and initiate nucleation using constitutively active versions of the NPFs, WAVE and NWASP. Furthermore, I intended to explore the role of capping protein in defining the boundary conditions of branched actin nucleation within the reconstituted systems.

4.2.2 Membrane Recruitment of NPFs at Varying Densities

In cells, NPFs are recruited to the plasma membrane, where they subsequently activate the Arp2/3 complex and initiate branched actin nucleation. My findings from *in vitro* reconstitution experiments in solution with physiological boundary conditions showed the presence of a metastable state where the system was kinetically prevented from reaching thermodynamic equilibrium. However, under similar conditions within cells, branched actin nucleation occurs. To enhance the equivalence between my reconstituted system and physiological conditions in cells, I attempted to mimic plasma membrane-recruited NPFs by examining NPFs embedded onto lipid bilayers. Moreover, I explored how the membrane density of NPFs influenced branched actin nucleation.

4.2.3 Comparing the Effects of NPF Densities with Dual NPF Binding to Arp2/3 Complex and Mother Filament Supplementation

The Arp2/3 complex can simultaneously bind to two molecules of NPFs and requires binding to a pre-existing mother filament to be activated and initiate the formation of a daughter filament. Since altering NPF density could impact either of these processes, I aimed to discern the effect of modulating NPF density from the process of dual NPF binding or an excessive presence of mother filaments. To elucidate the impact of dual NPF binding, I performed experiments using dimeric variants of the NPFs. Furthermore, I carried out studies with excess mother filaments that were stabilized to enable Arp2/3 complex binding for nucleation purposes but did not engage in polymerization themselves. This design permitted a more precise investigation into the influence of NPF density on the process of branched actin nucleation.

5 Results

5.1 Mechanism of Inorganic Phosphate Release

Actin filaments spontaneously hydrolyze ATP into ADP and transiently retain P_i before releasing it. The rate of P_i release has been observed to be faster at the terminal subunit compared to the core of actin filaments, however the mechanism of P_i release is not well understood. Understanding the mechanism of P_i release is essential for gaining insight into the kinetics-driven temporal regulation of actin dynamics. In this section of my thesis, I discuss the findings that aid us in our understanding of the mechanistic details of P_i release from actin filaments.

5.1.1 Evolution of nucleotide states in an ageing actin filament

Actin is an ATPase and can hydrolyze ATP in both its monomeric and filamentous states. However, the rate of ATP hydrolysis in actin filaments (0.3 s^{-1}) is significantly higher than when it is in its monomeric state. This increase in ATP hydrolysis rate upon incorporation of the monomer into a filament results in the rapid transition of the incorporated filament subunit to an ADP-P_i-bound state before releasing P_i and finally transitioning to an ADP-bound state. The rate at which P_i is released from the filament varies depending on the position of the subunit within the filament. Terminal subunits exhibit a much higher rate of P_i release (> 2 s^{-1}), in contrast to internal subunits that release their bound P_i at a much slower pace (0.003 s^{-1}). Additionally, the process of P_i release is stochastic rather than one that is deterministic and dependent on neighboring subunits. Collectively, these processes result in an inhomogeneous distribution of different nucleotides in a growing actin filament and constantly evolve with the age of the filament. To visualize the distribution of various nucleotides in a growing actin

filament, I performed a Monte Carlo simulation to model the stochastic process of actin filament growth and to determine how the distribution of different nucleotides changes with the age of the filament.

I simulated the growth of an actin filament under conditions where the pointed end is tethered, and growth and shrinkage occur exclusively through the barbed end. This was done for parity with single filament experiments utilizing actin filaments grown from surface-tethered spectrin-actin seeds, which will be discussed in detail in an upcoming section. Some fundamental assumptions were made. Firstly, I assumed that the hydrolysis of ATP from an incorporated actin subunit is a stochastic process, as there is substantial evidence for P_i release to be stochastic [66], and I assumed similarly for ATP hydrolysis. Secondly, I presumed that the rate of ATP hydrolysis does not depend on the position of the subunit within the filament, unlike the case for P_i release which is known to be rapid in the terminal actin subunit. This assumption was made based on a lack of evidence supporting differential hydrolysis rates dependent on subunit position. Additionally, to simplify the process, the system was modeled under pseudo-first-order conditions with a constant actin concentration, ensuring that the polymerization rate would always remain constant. Furthermore, I simulated growth from a pool of profilin-actin instead of actin itself, as this aligned with experimental conditions that made it simpler to prevent spontaneous nucleation in bare actin conditions.

Stochastic simulations of actin filament polymerization were conducted under 2 μM profilin-actin (17.7 monomers$\cdot s^{-1}$) for a duration of 300 seconds. At 300 s, the simulation was set to depolymerizing conditions by setting and maintaining the concentration of profilin-actin to zero. Polymerization proceeded using ATP-actin subunits that could hydrolyze after filament incorporation (0.3 s^{-1}). However, since the terminal subunit could be in any of the three nucleotide states during depolymerization, the instantaneous depolymerization rate varied between the rates of the ATP-bound (1.4 s^{-1}), ADP-P_i-bound (0.2 s^{-1}), or ADP-bound (6.6 s^{-1}), actin subunit. Furthermore, the P_i release rate was determined based on the positioning of the ADP-P_i-bound subunit as either an internal subunit (0.011 s^{-1}) or the terminal subunit (5.1 s^{-1}). A sequence of snapshots derived from the stochastic simulation illustrates changes in filament length and the development of nucleotide distribution as an actin filament ages (fig. 5.1).

As the actin filament grows in the simulation through the incorporation of ATP-bound actin subunits (red in fig. 5.1), it rapidly hydrolyzes the nucleotide, transitioning to an

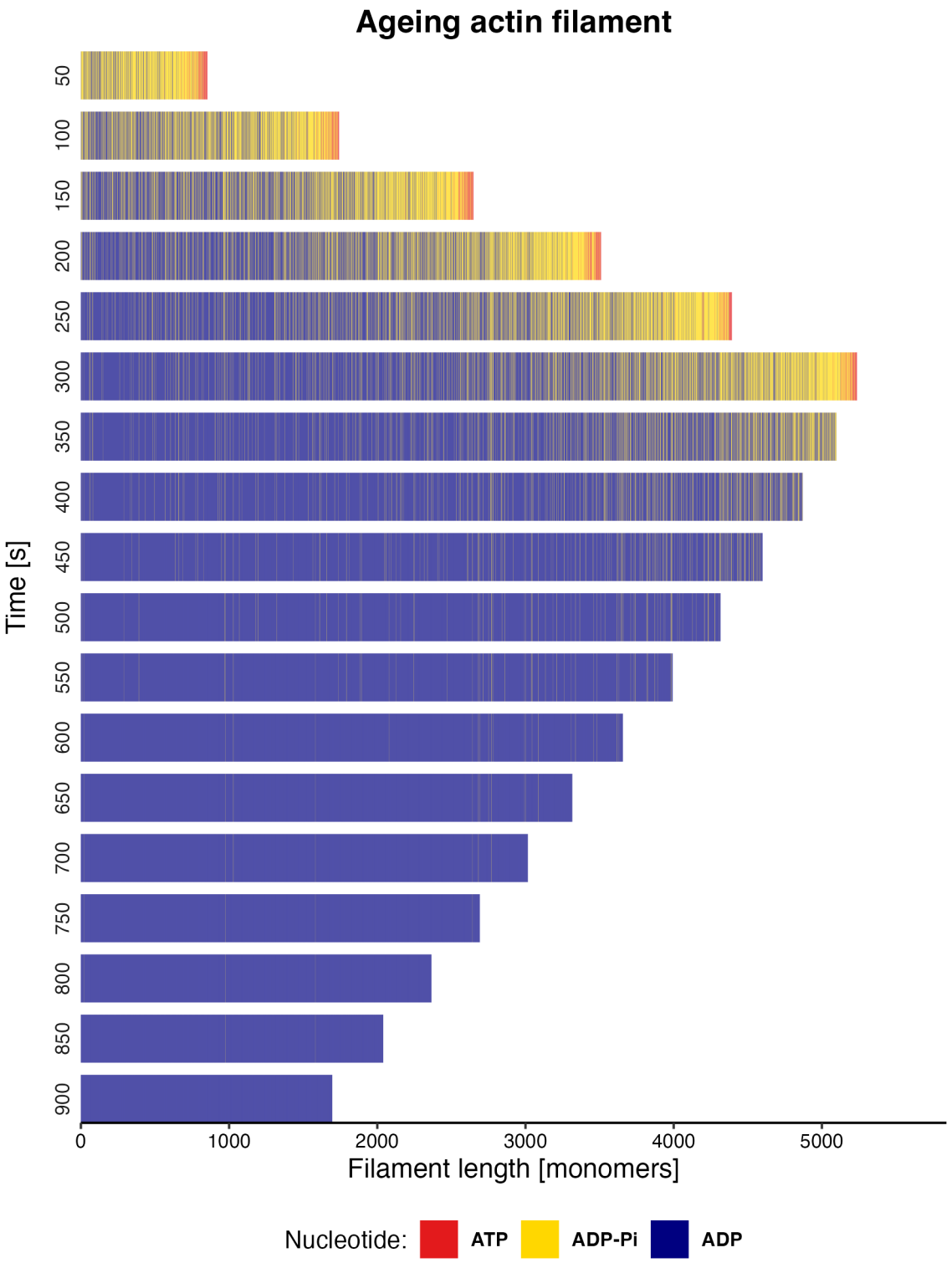

Figure 5.1: Stochastic simulation of an aeging actin filament. The simulated filament polymerizes from 2 μM ATP-bound actin subunits (red) for a duration of 300 seconds. Subsequently, it depolymerizes in the absence of monomeric actin. During these processes, actin hydrolyzes ATP to generate ADP-P_i containing subunits (yellow) that release their bound P_i to transition to the ADP-bound state (blue) over time. *[Continued on the following page.]*

Figure 5.1: Growth and depolymerization processes in the filament occurs exclusively at the barbed end (right hand side).

ADP-P_i-bound state (yellow in fig. 5.1). Due to the slow P_i release rate, a visible cap of ADP-P_i-rich region accompanies the growing filament and eventually fades at older parts of the filament enriched with ADP-bound actin (blue in fig. 5.1). As polymerization occurs exclusively through ATP-bond subunits, the length of the filament linearly increases during this process (fig. 5.2A, grey time window). However, upon initiation of depolymerization, the length variation becomes nonlinear since the instantaneous depolymerization velocity depends on the nucleotide state of the terminal subunit (fig. 5.2, unshaded time window). Initially, the depolymerization velocity is predominantly influenced by the ADP-P_i-bound state but eventually approaches a purely ADP-bond state.

This change in the instantaneous depolymerization velocity can be further elucidated through the analysis of different nucleotide state distributions within the filament over time. During the polymerization phase, the actin filament swiftly hydrolyzes ATP and rapidly reaches a steady state with approximately 50-60 subunits in the ATP-bound state (fig. 5.2B and C, upper panels). Following the hydrolysis of ATP, the filament accumulates ADP-P_i-bound subunits, which tend towards a steady state as P_i is released from the older sections of the filament (fig. 5.2B and C, middle panels). Throughout the polymerization phase, the number of ADP-bound subunits increases (fig. 5.2B, lower panel). During the depolymerization phase, all ATP-subunits are hydrolyzed within a few seconds (fig. 5.2B and C, upper panels). Conversely, ADP-P_i-bound subunits gradually decay to become ADP-bound subunits (fig. 5.2B and C, middle panels), eventually resulting in the filament progressively maturing towards the ADP-bound state (fig. 5.2C, lower panel). Since ATP-bound subunits are instantly hydrolyzed, they contribute insignificantly to the depolymerization velocity, which is instead dominated by the exponentially decaying ADP-P_i-bound subunits that approach the ADP-bound subunit depolymerization velocity. As the depolymerization velocity of ADP-P_i-bound subunits is slower than that of ADP-bound subunits, the initial part of the depolymerization phase exhibits a characteristic curvature in the evolution of length over time. This curve starts with a slower depolymerization velocity and transitions towards a faster one (fig. 5.2A, unshaded time window).

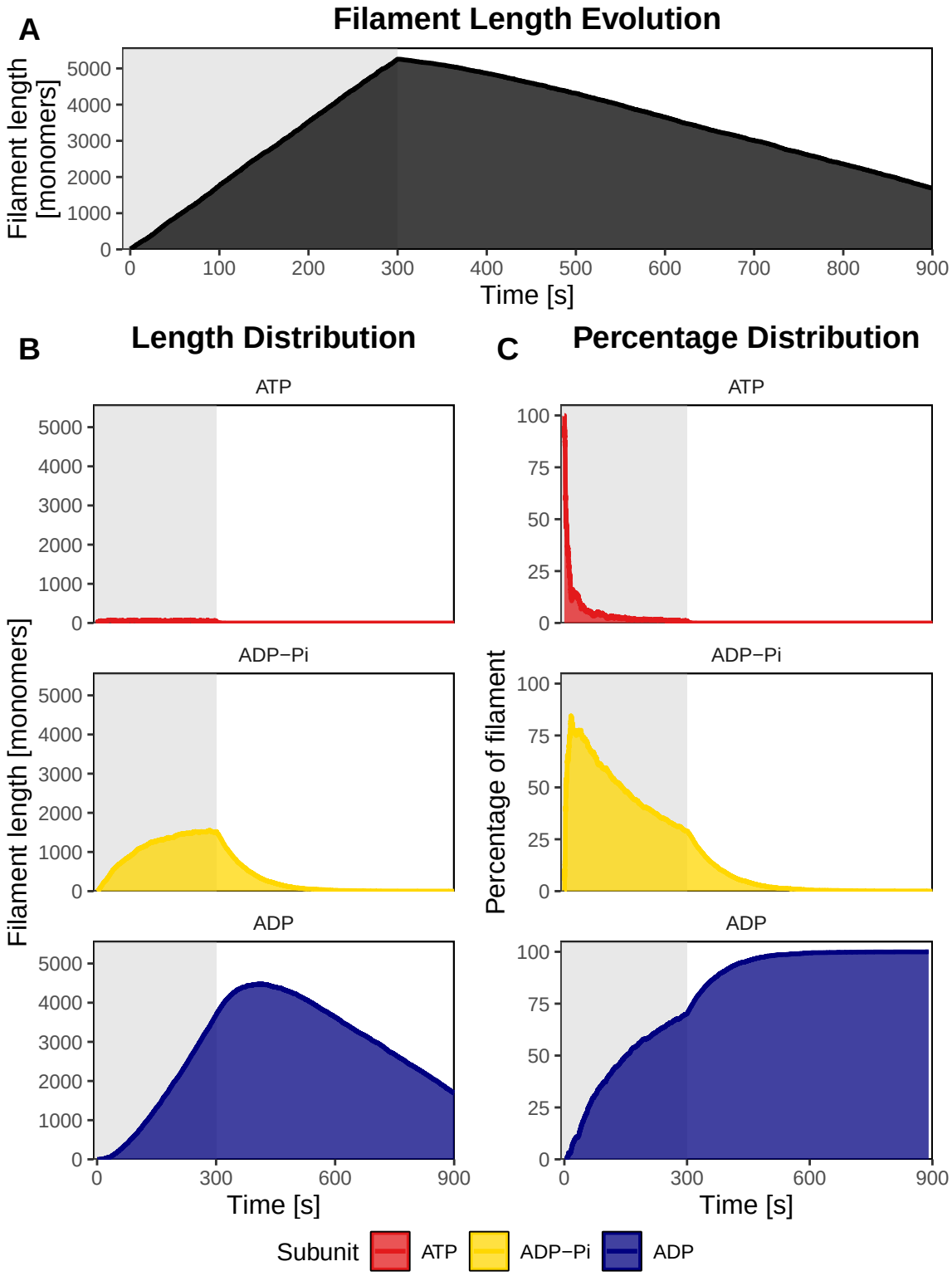

Figure 5.2: Distribution of different nucleotide states in an aging actin filament. **A)** Evolution of filament length over the time course of the stochastic simulation. **B)** Distribution of the number of monomers exhibiting different nucleotide states in the filament. **C)** Percentage of subunits in the filament exhibiting different nucleotide states at any point in time. *[Continued on the following page.]*

Figure 5.2: Grey shaded area indicates the time window during which the filament was polymerized and the unshaded area indicates the depolymerization period.

Though a detailed distribution of nucleotide states cannot be directly visualized in experiments, we use the transition in depolymerization velocities as a proxy in an upcoming section. This transition signifies the shift from a filament terminus predominantly composed of ADP-P_i-bound subunits to one with only ADP-bound subunits.

5.1.2 Steric occlusion of the P_i release pathway

The release rate of P_i is significantly higher ($> 2\ s^{-1}$) at the terminal subunit compared to that in an internal subunit ($0.003\ s^{-1}$). To understand the underlying cause, we collaborated with Wout Oosterheert in the department of Structural Biochemistry in our institute led by Stefan Raunser, who determined the Cryo-EM structure of the undecorated barbed end of an actin filament [106]. Specifically, the structure of the barbed end consisting of β,γ-actin was obtained from about 44,000 particles and refined to a resolution of 3.59 $\mathring{A}$ with the asymmetric unit containing four actin subunits (fig. 5.3, PDB 8OI6). The asymmetric unit encompasses the barbed end, which consists of the terminal subunit A_0 and penultimate subunit A_1, as well as two internal subunits, A_3 and A_4. All actin subunits in this structure are bound to ADP, suggesting an aged filament state.

To identify potential differences in conformation between the terminal subunit A_0 and internal subunit A_2, we performed a structural superimposition using Cα atoms from both subunits. Remarkably, the overall Cα RMSD between the two subunits was less than 1 $\mathring{A}$ demonstrating that the overall structure of these subunits were very similar. Although the global differences were not immediately apparent, local rearrangements distinguish the two subunits notably at the Pro-rich loop (residues 107-112), W-loop (residues 165-172), hydrophobic plug (residues 264-273), and disordered carboxylic terminus (residues 363-375) of the actin subunits [106]. Taken together, these results suggest the absence of any major structural rearrangements that potentiate P_i release.

One of the earliest investigations into the mechanism of P_i release was performed using MD simulations. The results from these simulations suggested that P_i is released from the subunit by exiting the nucleotide cleft via a solvent-accessible cavity, known as an

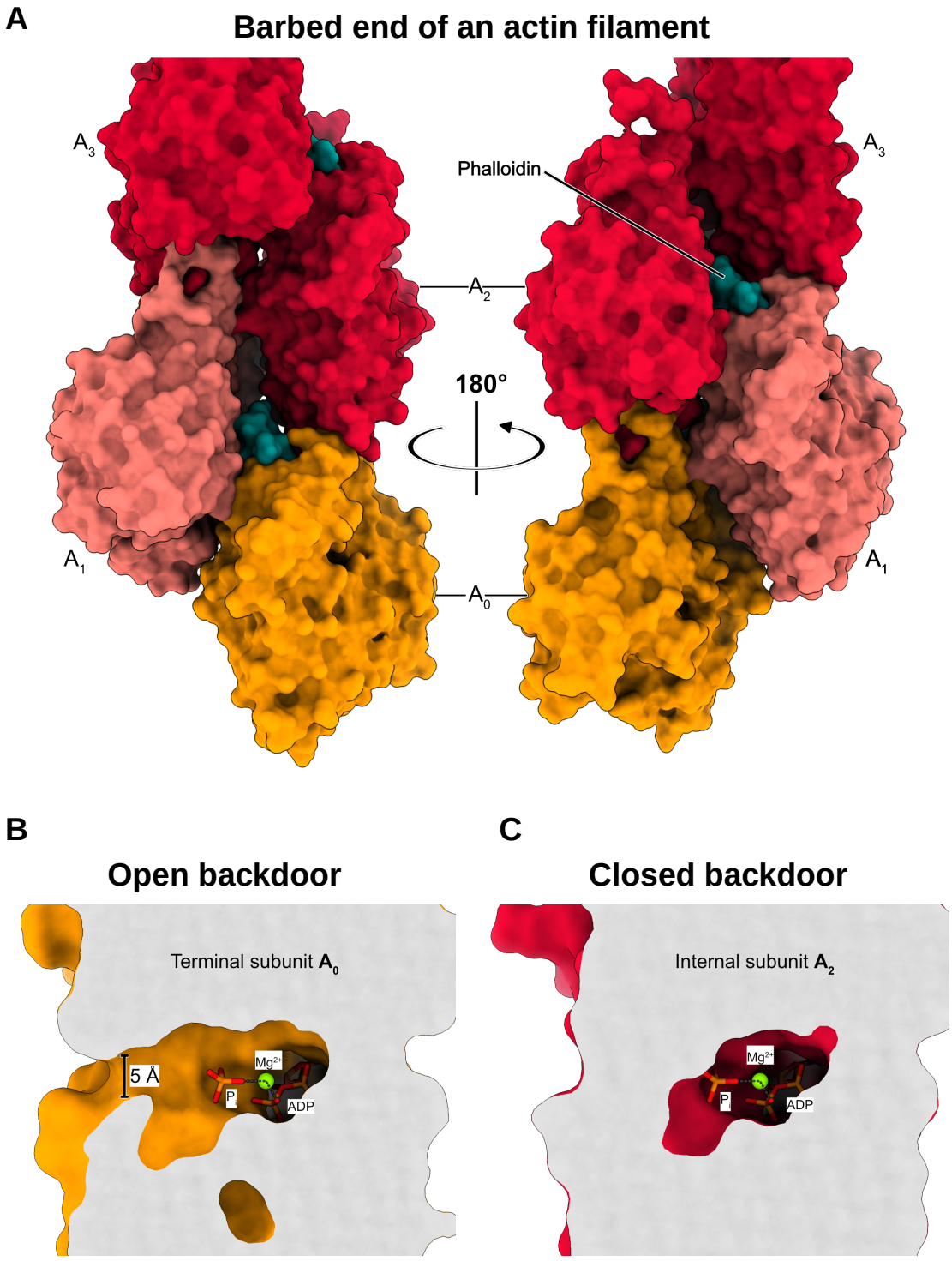

Figure 5.3: Cryo-EM structure of the barbed end of an actin filament. A) Surface representation of the barbed end of an actin filament bound to phalloidin. The structure depicts the barbed end comprising the terminal (A_0) and penultimate subunit (A_1), along with internal subunits (A_2 and A_3). *[Continued on the following page.]*

Figure 5.3: B) Surface slice of the nucleotide-binding cleft from the terminal subunit (A_0) of the actin filament, showing the open backdoor conformation. **C)** Surface slice of the nucleotide-binding cleft from an internal subunit (A_2) of the actin filament, illustrating the closed backdoor conformation. Additionally, **B** and **C** denote the positions of ADP, Mg^{2+}, and P_i within the nucleotide-binding cleft.

open backdoor, through disrupting its ionic bond with Mg^{2+} and rearrangement of the R177 and H73 sidechains. However, it is important to note that this simulation was carried out using the structure of monomeric actin as a reference, which is known to conformotionally differ from filamentous subunits that undergo flattening of the pseudo-dihedral angle upon polymerization. In fact, we found that the internal subunit A_2 has a closed backdoor, which occludes the escape of P_i (fig. 5.3C), in line with high-resolution structures of filamentous actin determined previously [107, 108]. Surprisingly, the terminal subunit A_0 was found to have an open backdoor in contrast to the internal subunit A_2 (fig. 5.3B and C). The absence of steric occlusion for the release of P_i in the terminal subunits might explain its faster P_i release kinetics compared to the internal subunits.

During our investigation of the backdoor, we discovered an intricate hydrogen bonding network mediated by residues at the closed backdoor of internal subunits (N111, R177, H73, and G74). These residues appear to be disrupted in the open backdoor of the terminal subunit. Notably, some of these same residues have previously been implicated in mediating the release of P_i. To identify the most likely egress pathway and the amino acid residues that regulate the release of P_i from actin filaments, MD simulations were performed by our collaborator, Florian E. C. Blanc at the Department of Theoretical Biophysics at the MPI in Frankfurt [107].

Simulating P_i release from the terminal subunit (A_0) of the actin filament revealed a trajectory similar to one previously reported [107] and involved the R177-N111 backdoor. Due to the longer timescale required for the kinetics of P_i release from the core of actin filaments ($t_{1/2} > 100$ s), conventional MD simulation methods are not suitable for studying this phenomenon. As a result, a novel method with an enhanced sampling strategy was developed to study the egress pathways of P_i release from the core of actin filaments.

Interestingly, the simulations revealed two plausible egress pathways: one involving the residues in the canonical backdoor (R177-N111), and another involving the residue R183.

The residues N111 and R183, which are involved in the two egress pathways, have previously been implicated in disease-linked mutations that cause actin-related disorders and developmental malfunctions [109, 110]. To further identify their role in the release of P_i from filaments, biochemical assays with an actin mutant of the N111 residue (N111S) was carried out as described in the following section.

5.1.3 Instantaneous release of P_i from actin mutants

To investigate the role of the actin mutants in P_i release from filaments, two different experimental strategies were employed. In the initial approach, pyrene fluorescence and a fluorescent P_i sensor were used synchronously to observe bulk polymerization and P_i release concurrently. The second strategy involved growing individual actin filaments and measuring alterations in depolymerization velocities using microfluidics-assisted TIRF microscopy.

Experiments involving bulk polymerization were carried out by Peter Bieling. In these experiments, actin filaments were polymerized from spectrin-actin seeds while monitoring the polymerization progress via pyrene fluorescence. Concurrently, as the filament grew and began to age, the released P_i was measured with a fluorescence based MDCC P_i sensor. In the case of wt-actin, a notable delay was detected between polymerization onset and P_i release, evident by the distinct separation of pyrene fluorescence and and MDCC fluorescence (fig. 5.4A). Conversely, the N111S mutant displayed instantaneous P_i release as evidenced by the overlapping polymerization and P_i release curves. By applying a reaction kinetics model to account for both polymerization and P_i release processes, an estimated effective P_i release rate (k_{-P_i}) of at least 15-fold higher (≥ 0.1 s^{-1}) was determined for the N111S mutant compared to wt-actin (0.0065 s^{-1}). The R183W mutant also exhibited about 3-fold higher P_i release rate in comparison to the wt-actin

To evaluate the P_i release rate at the level of individual actin filaments, I performed single filament assays by growing actin filaments from surface tethered spectrin-actin seeds (fig. 5.4B). To calculate the instantaneous depolymerization accurately, it was crucial to have an accurate measurement of the filament length at any point in time. I used a constant flow to align the filaments in the direction of the flow, ensuring that the filaments were more reliable in tracking and their length measurements during the two phases, the

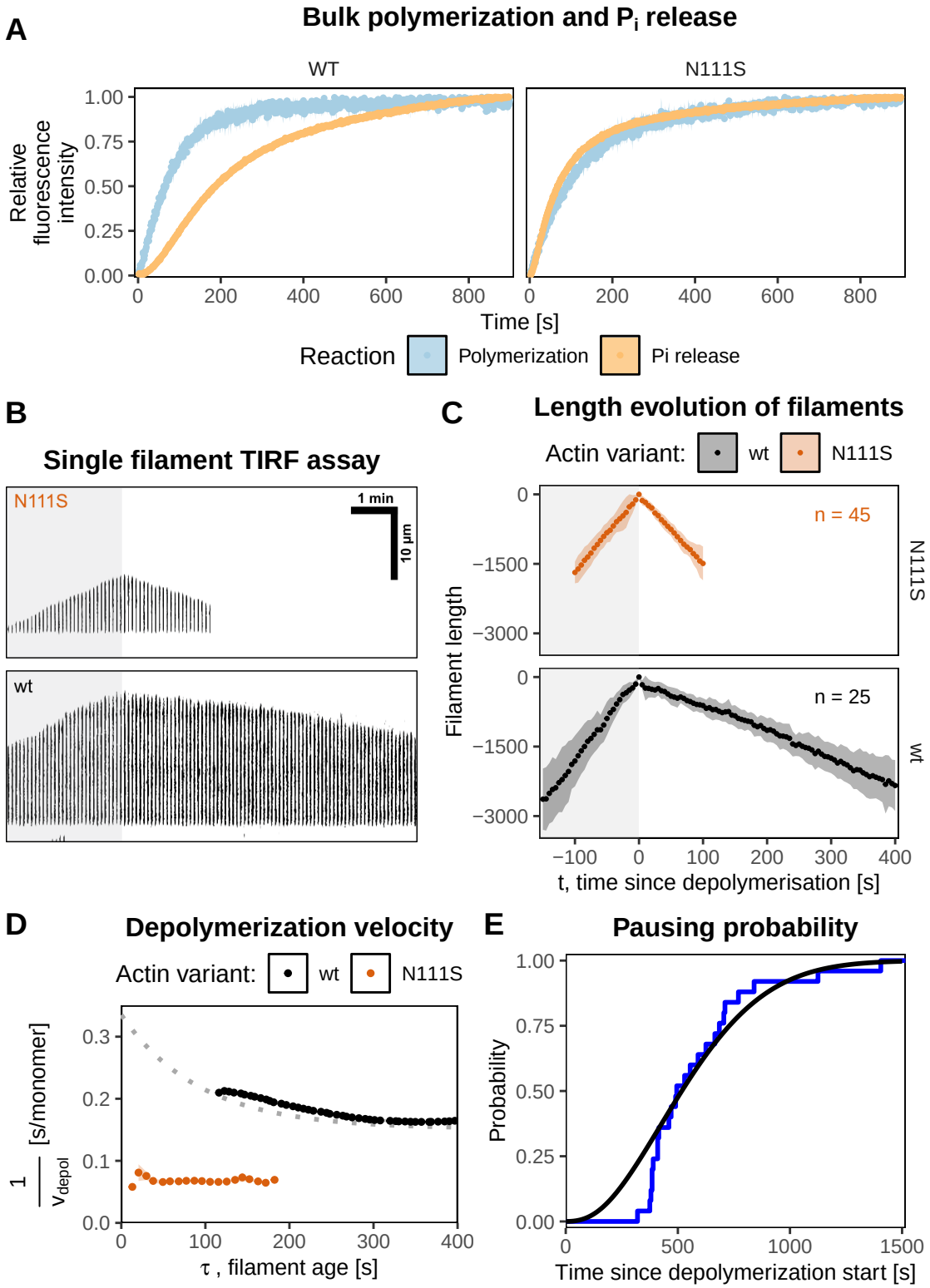

Figure 5.4: P_i release kinetics of actin and its mutant. A) Simultaneous measurement of bulk polymerization and P_i release for wild-type (wt) and N111S mutant actin. Polymerization reaction consisted of 10 μM actin, 1.5% pyrenyl-actin, 30 nM MDCC P_i sensor, and 160 nM spectrin-actin seeds. Relative fluorescence intensity of pyrene (cyan) and the MDCC P_i sensor (light orange). *[Continued on the following page.]*

Figure 5.4: B) Time-lapse imaging of single filament polymerization and depolymerization using microfluidics-assisted TIRF microscopy. Actin filaments (black) were grown from surface-attached spectrin-actin seeds and visualized with AlexaFluor488 labeled Lifeact. The horizontal axis represents time, while the vertical axis shows the length of an actin filament. **C)** Average length of wt actin filaments (black) and N111S mutant actin filaments (red), measured by tracking individual filament growth in C. The shaded region around the mean indicates standard deviation. The grey shaded area in B and C represents the time window for polymerization, with the unshaded area indicating depolymerization periods. **D)** Instantaneous depolymerization velocity ($1/v_{depol}$) as a function of filament age (τ). v_{depol} was calculated using average filament lengths measured in C. Gray dashed line indicates a fit used to obtain the P_i release rate constant from the wt data (black). **E)** Cumulative pausing probability of single filament depolymerization. Survival curve for pausing events observed in individual depolymerizing filaments (blue), with each step representing the fraction of filaments that have paused at any given point in time. Predicted pause probability from a model considering protomer transition rates leading to pause of depolymerizing actin filaments [111].

polymerization phase (fig. 5.4B, grey shaded window) and the depolymerization phase (fig. 5.4B, unshaded window), of the reaction cycle, were consistent.

Tracking the length of actin filaments during the polymerization phase shows a linear increase in filament length. This linearity in filament length increase was observed for both wt-actin and the N111S mutant (fig. 5.4C, grey shaded window). Additionally, the polymerization rates calculated from the length changes were comparable for both the wt and N111S mutant (about 11 monomers$\cdot s^{-1}$ at 1 μM actin). However, the behaviors during the depolymerization phase differed significantly between the two actin variants (fig. 5.4C, unshaded window). In agreement with previous work [66], the length changes in wt-actin during the depolymerization phase were nonlinear, exhibiting a slight convex region towards the beginning of the depolymerization. In contrast, the N111S mutant demonstrated a completely linear length change profile during the depolymerization phase.

The nonlinearity observed in the length of actin filaments during the depolymerization phase can be attributed to the variable depolymerization velocities, which change from those of ADP-P_i-subunits to those of ADP-subunits due to P_i release. This was also evident in the simulations discussed previously (fig. 5.2A). Since P_i release is a first-order reaction, the amount of P_i within the filament decays exponentially and this decay is a function of the filament age. The rate at which P_i decays is directly proportional to the

rate at which the depolymerization velocity changes from that of an ADP-P_i-subunit to that of an ADP-subunit in aging filaments.

To ensure that intermittent pausing of filaments did not influence the results, all analysis was restricted to time frames when filaments continuously depolymerized. Moreover, the pausing probability of filaments was determined to obtain a low protomer transition rate of $5.8 \times 10^{-7} s^{-1}$ (fig. 5.4E). This value is consistent with previous observations [111] and reflects that photo-induced dimerization does not significantly contribute at the time scales relevant for calculating depolymerization velocities.

The P_i release rate was determined by fitting the instantaneous depolymerization velocity of actin filaments as a function of filament age (fig. 5.4D). The wt-actin had a P_i release rate of 0.0077 s^{-1}. Due to the absence of a detectable transition from ADP-P_i-subunits to ADP-subunits depolymerization velocities in the N111S mutant, its P_i release rate could only be estimated (0.113 - 0.117 s^{-1}). However, the estimated P_i release rate for the N111S mutant is much higher than the wt-actin rates. These findings are consistent with bulk experiments which indicated instantaneous P_i release. Taken together, these results highlight the crucial role of N111 in maintaining the hydrogen-bond network that regulates P_i release from the backdoor of the actin filament core.

5.2 A Novel Density Dependent Mechanism of NPF Regulation

Cells create forces required for motility by generating branched actin networks through the Arp2/3 complex. The activity of the Arp2/3 complex is spatially confined to the membrane surface because NPFs spatially regulate the activity of the Arp2/3 complex, preventing it from generating branched networks in the cytoplasm. The exact mechanism by which NPFs regulate their nucleation machinery in the absence of autoinhibition remains unclear. In this section of my thesis, I will discuss the experimental results that reveal a novel density-dependent regulation of NPF activity.

5.2.1 A metastable pool of actin and its nucleator

To explore the regulatory mechanisms of NPFs on actin nucleation and polymerization dynamics, I initiated my study by reconstituting the branched actin machinery *in vitro*. The primary objective was to establish a system that closely mimics physiological conditions within cells and can be continuously monitored to capture dynamic changes as the reaction approaches kinetic and in some cases thermodynamic equilibrium.

To track the actin polymerization reaction, I utilized the so-called pyrene assays. In these experiments, reactions were supplemented with a minor concentration of pyrene-labeled actin that drastically increases its fluorescence when labeled subunits are incorporated into actin filaments (fig. 5.5A). Pyrene assays have been previously demonstrated to have minimal interference with nucleation and polymerization processes [112].

Monomeric actin spontaneously nucleates into filaments above its critical concentration (0.12 μM). Nevertheless, the reaction is constrained by the rate-limiting step of trimeric nucleus formation. In reactions with varying monomeric actin concentrations, the rate of polymerization (slope of polymerization curves, fig. 5.5B) and the amount of polymerized actin (height at saturation in figure fig. 5.5B and C) are directly proportional to the monomeric actin concentration. The presence of an initial lag-phase, particularly evident at lower actin concentrations, signifies the unfavorable process of nucleus formation. Following this, the nuclei elongate by incorporating monomers until the free monomeric actin concentration in the reaction reaches the critical concentration.

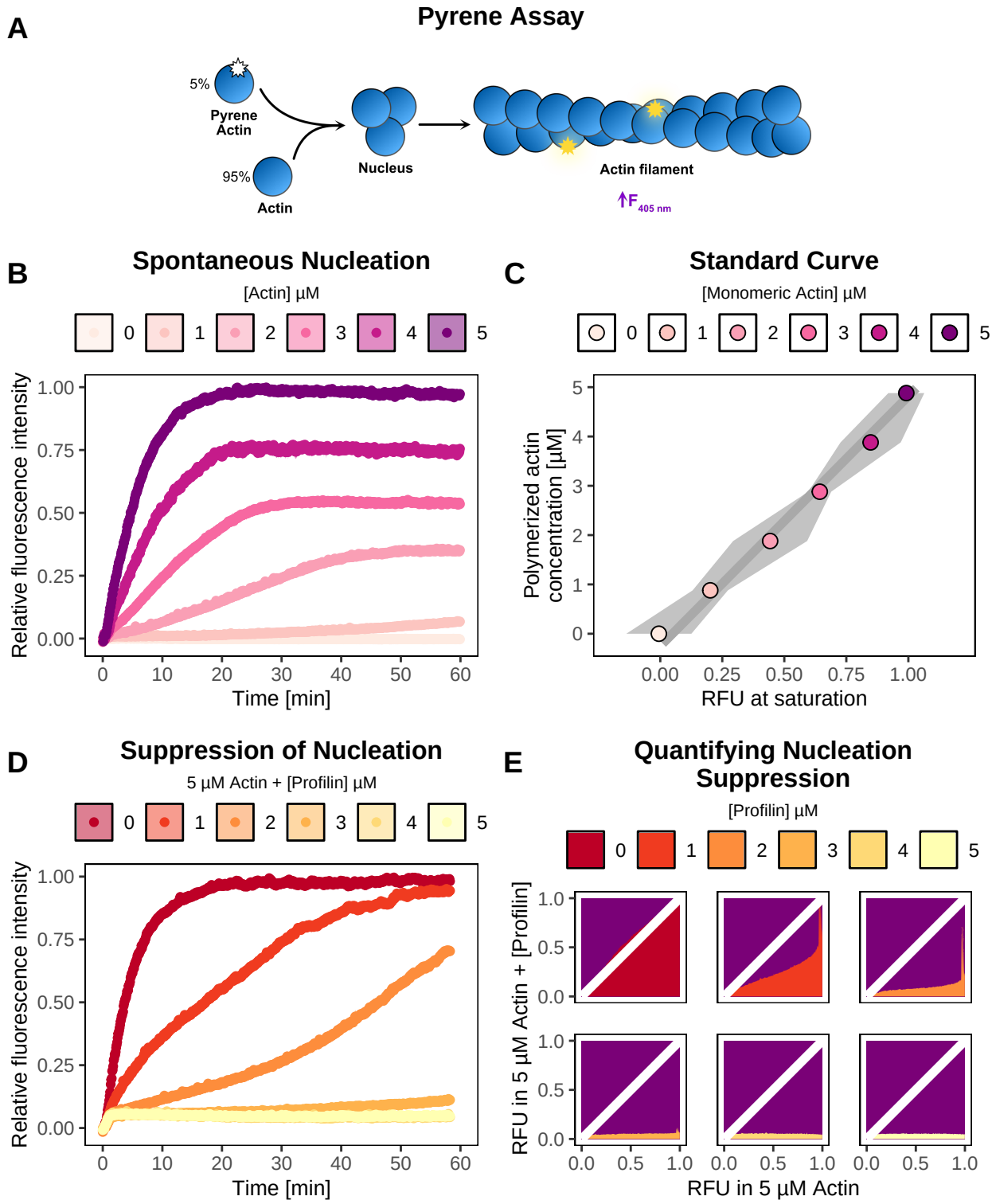

Figure 5.5: Spontaneous nucleation and polymerization. A) Schematic representation of a pyrene assay with bare actin. Reaction contains 95% unlabeled β,γ-actin and 5% pyrene-labeled α-actin. Actin spontaneously forms a trimeric nucleus above its critical concentration and polymerizes into filaments upon which pyrene fluoresces, with an emission at a λ_{max} of 405 nm. *[Continued on the following page.]*

Figure 5.5: B) Time course of actin polymerization at different monomeric actin concentrations. Color indicates the concentration of actin from 0 μM to 5 μM. **C)** Standard curve obtained from fitting the amount of polymerized actin and the relative fluorescence at saturation from polymerization time courses obtained from various concentrations of actin (as used in B). **D)** Time course of actin polymerization in the presence of different concentrations of profilin. Polymerization reaction was initiated with 5 μM actin, and varying concentrations of profilin from 0 to 5 μM were present (indicated by color). **E)** Quantifying the amount of suppression of nucleation with various concentrations of profilin. Dark pink indicates polymerization of 5 μM actin in the absence of profilin, as shown in B. Various shades from red (0 μM) to light yellow (5 μM) indicate the same reaction in the presence of different concentrations of profilin (as shown in D). The size of the shaded regions in the diagram signifies the disparities in the quantities of polymerized actin as the reaction proceeds. An equal extent of shading in both halves of the diagonal denotes an absence of suppression in nucleation, whereas smaller shaded areas in the profilin-containing diagonal half indicate suppressed nucleation in the presence of profilin. The data points in B, C, and D represent the average values derived from replicates. The shaded areas surrounding the points denote the standard deviations, with 6 replicates for data sets B and C, and 10 replicates for data set D. Areas in E are derived from average relative fluorescence intensity (RFU) values in B and D.

Equilibrium in the polymerization reaction is achieved within a span of 15-20 minutes for 5 μM actin (as shown in figure 5B, dark pink). In cells, the actin concentration range between 100-150 μM. If spontaneous nucleation were not prevented, actin would instantaneously polymerize into filaments, depleting the pool of actin available for further polymerization and exhausting the potential energy required to generate forces against a load-bearing membrane. Profilin impedes spontaneous nucleation of actin monomers and preserves a reservoir of polymerizable actin by binding with high affinity to monomers. When profilin is added to the polymerization reaction, it significantly reduces the rate of spontaneous nucleation at sub-stoichiometric concentrations of profilin and completely inhibits nucleation at stoichiometric amounts (as shown in figure fig. 5.5D). It is worth noting that while profilin hinders nucleation, it can still polymerize from the barbed end once a nucleus is formed. This effect is particularly evident when 3 μM profilin is used, as the amount of polymerized actin tends to increase towards the end of the time course (fig. 5.5D). The suppression of overall polymerization is higher during the initial stages but eventually the system approaches complete polymerization due to nuclei elongation by both actin and profilin-actin complexes (fig. 5.5E). These findings demonstrate that profilin can maintain a metastable state in which the system remains for prolonged times

away from thermodynamic equilibrium. However, upon the formation of a nucleus, the reaction will eventually progresses towards equilibrium.

To investigate branched actin nucleation, we used an excess of profilin in all subsequent experiments to maximally suppress spontaneous nucleation and to ensure Arp2/3 complex-mediated nucleation. This setup mirrors the cellular conditions, where most of the polymerizable pool of actin is bound to profilin. We utilized a constitutively active variant of NPF, which does not necessitate activation via GTPases or PIP lipid binding. This NPF construct only includes the proline-rich domain required for profilin-actin binding, the WH2 (V) domain required for actin binding, and the Arp2/3 complex activation domain (fig. 5.6A). Since spontaneous nucleation is suppressed in the presence of an excess of profilin over the time-scales of our experiment, any nucleation leading to polymerization and pyrene fluorescence must occur via Arp2/3 complex-mediated branched actin nucleation. Nevertheless, the Arp2/3 complex requires a pre-existing mother filament, which introduces a rate-limiting step dependent on mother filament formation.

The Arp2/3 complex initiates nucleation from a profilin-bound actin pool in the presence of NPFs at concentrations as low as 5 nM. Additionally, the nucleation rate increases with the concentration of the NPF. In contrast, the control reaction with profilin-actin does not nucleate and polymerize in the absence of NPFs, even with 50 nM Arp2/3 complex concentration. These results suggest that the Arp2/3 complex is inactive in the absence of the constitutively active NPF but initiates rapid nucleation upon interaction with the NPFs. Furthermore, at these concentrations of the Arp2/3 complex, the nucleation rate exhibits a $t_{1/2}$ of less than 10 minutes for the slowest reaction with 5 nM NPF (fig. 5.6B). The nucleation rate is contingent upon both the Arp2/3 complex and NPF concentrations. An increase in the concentration of either component leads to an increased nucleation activity, attaining the maximum at the highest concentrations of the Arp2/3 complex and the NPF (fig. 5.6C).

In cells, newly nucleated filaments do not polymerize indefinitely, but are eventually capped at their barbed ends by capping protein (CP). This process prevents the formation of excessively long filaments that do not offer the required pushing force. Capping barbed ends also enables the growing actin network to preserve a consistent directional pushing force due to Arp2/3 complex's canonical 70° branch angle and increasing network branching density. In an experiment involving profilin-actin, Arp2/3 complex, and

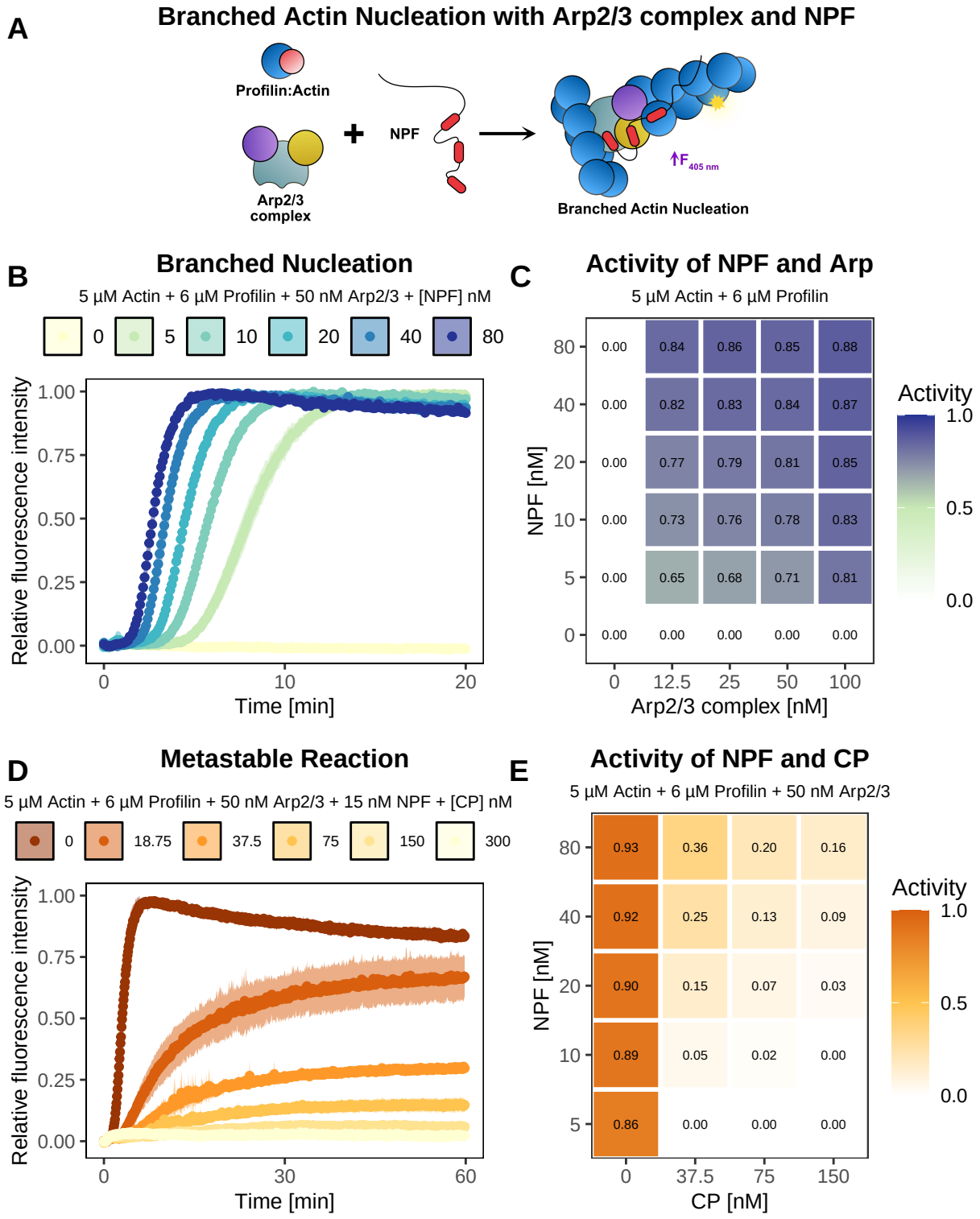

Figure 5.6: Branched Actin Nucleation and Metastability. **A)** Schematic representation of branched actin nucleation mediated by Arp2/3 complex and a constitutively active NPF. The VCA domain of NPF is indicated by three oblong structures in the NPF schematic, with the rest of the sequence being largely unstructured indicated with a wavy line. *[Continued on the following page.]*

Figure 5.6: Branched actin nucleation is indicated by the Arp2/3 complex binding to a pre-existing filament, a NPF, and spawning a daughter filament. **B)** Time course of actin polymerization from branched actin nucleation. The reaction contains 5 μM actin, 6 μM profilin, 50 nM Arp2/3 complex, and varying concentrations of NPF (0 to 80 nM, indicated by color). **C)** Activity matrix quantifying the area under the polymerization curve for reactions with actin, profilin, and various concentrations of the Arp2/3 complex (x-axis) and NPF (y-axis). The shade of the tiles indicates the activity, from a scale of 0 (white) to 1 (blue) obtained from a 30 min time course. **D)** Branched actin nucleation and polymerization in the presence of CP. The reaction contains the same components as in B with 15 nM NPF and varying concentrations of CP (0 to 300 nM, indicated by color). **E)** Activity matrix of the polymerization reactions in D with varying concentrations of CP (x-axis) and NPF (y-axis). The shade of the tiles indicates the activity, from a scale of 0 (white) to 1 (orange) obtained from a 60 min time course. D and E indicate that branched actin nucleation can be completely suppressed by CP, maintaining it in a metastable state. The data points in B, and D represent the average values derived from replicates. The shaded areas surrounding the points denote the standard deviations, with 8 replicates for data set B, and 6 replicates for data set D. The activity in C and E are derived from average area under the polymerization curves such as those in B and D respectively. Each tile contains averages calculated from 6 or more replicates.

constitutively active NPF, I observed that the rate of nucleation and overall amount of filamentous actin at saturation decreased with rising CP concentrations. Remarkably, at CP concentrations above 150 nM, nucleation and polymerization were completely abrogated, leaving the system in a new metastable state, which remained kinetically inhibited from nucleation even when the Arp2/3 complex and an activating NPF were present (fig. 5.6D). Furthermore, these results obtained were identical in constitutively active variants of both WAVE and NWASP. The metastable state of the system could be tuned by adjusting both the NPF and CP concentrations. Higher concentrations of CP and lower concentrations of NPF were more refractory to nucleation, while lower concentrations of CP and higher concentrations of NPF showed nucleation (fig. 5.6E).

The existence of the metastable state under physiological concentrations of nucleators, their regulators, and capping protein is surprising, given that these same conditions yield successful branched networks at the leading edge of the cell. However, in the experiments so far, I have neglected to incorporate a crucial boundary condition – restricting the NPF activity to the membrane. In the following sections, I examine the significance of this physical constraint on the system and explore how it promotes nucleation more closely approximating *in-vivo* conditions.

5.2.2 Overcoming metastability with membrane bound NPFs

In cells, NPF activity is restricted to the cellular membranes. To constrain the NPF activity to the membrane surface in experiments, I used lipid-bilayer coated silica microspheres, which interact with the NPFs and bind them to the membrane. For this purpose, I utilized Ni-containing lipid membranes (98% PC and 2% Ni-NTA) that stably bind to the N-terminal His-tag of the constitutively active NPFs (fig. 5.7A). This setup enabled me to examine the impact of confining the NPF activity to membranes while maintaining control over the reaction's overall NPF concentration. Additionally, embedding the NPFs onto a lipid bilayer allows for their diffusional mobility, in contrast to previous experiments [cite] where NPFs were covalently linked to microspheres, restricting their movement. Embedding NPFs onto mobile membrane surfaces in these experiments replicates the boundary conditions found in cells more accurately.

I compared the behavior of membrane-bound NPF and soluble NPF under metastable conditions in a reaction comprising actin (5 μM), an excess of profilin (6 μM), 50 nM Arp2/3 complex, and 150 nM CP. In the absence of membrane binding, soluble NPF nucleates promptly in the absence of CP, and the reaction saturates within 15 minutes (fig. 5.7B, pink crosses). However, at the same NPF concentration, no nucleation or polymerization occurred when CP was present (fig. 5.7B, pink points), as previously observed. In contrast, membrane-bound NPFs rapidly nucleate even under metastable conditions with a reaction saturation within 15-20 minutes (fig. 5.7B, right panel, blue points). This effect was not observed when the reaction contained silica microspheres coated with 100% PC lipids that do not bind NPFs (fig. 5.7B, left panel, blue points). These findings suggest that NPFs are capable of nucleating under metastable conditions exclusively when they are tethered to membranes instead of freely diffusing in solution. It's important to emphasize that the observed nucleation effect in membrane-bound NPFs occurs at the same concentration where soluble NPF fails to nucleate, underscoring the crucial role of recruiting NPFs onto membranes as a boundary condition.

NPFs embedded onto the membrane increase the local density of the NPFs without altering the overall concentration of NPFs in the reaction. In the following sections, I explore how this dimensionality reduction facilitates overcoming metastability.

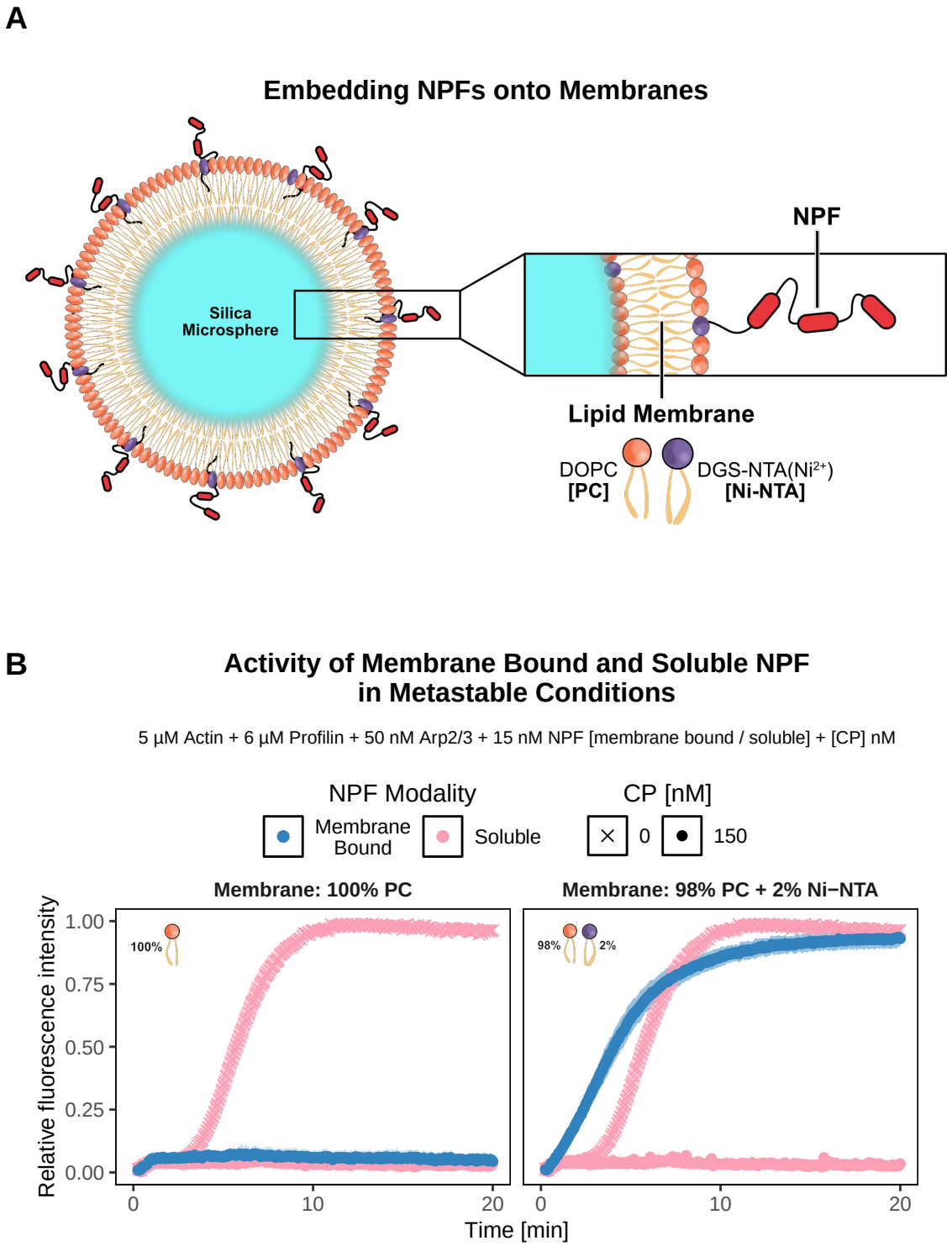

Figure 5.7: Membrane bound NPFs rescue metastability. A) Schematic representation of membrane-bound NPFs. Lipid bilayers comprised of a mixture of DOPC (PC) and DGS-NTA(Ni^{2+}) (Ni-NTA) are coated onto silica microspheres of 1 μm diameter. NPFs are embedded onto the lipid bilayers through interactions between their N-terminal His-tags and the Ni^{2+} metal ions in the lipid bilayer. *[Continued on the following page.]*

Figure 5.7: B) Time course of actin nucleation under metastable conditions. Comparison of nucleation induced by NPFs when supplied in a soluble form (pink) and in a membrane-bound state (blue). Soluble NPFs fail to initiate nucleation in the presence of CP under metastable conditions (pink points), whereas they rapidly nucleate in its absence (pink crosses). Membrane-bound NPFs rapidly nucleate actin even under metastable conditions when bound to Ni-containing membranes (blue dots in right panel), however, they fail to nucleate when provided with lipid-coated beads that do not embed NPFs due to their lack of Ni-containing lipids (blue dots in left panel). The data points in B represent the average values derived from 6 replicates and the shaded areas surrounding the points denote the standard deviations.

5.2.3 Heterogenous distribution of NPFs in cells

The findings from the preceding section suggest that alterations in the local concentration of NPFs while maintaining a constant global concentration can have substantial effects on nucleation dynamics. In light of these results, it is essential to examine the distribution of NPFs within cells, focusing on any potential differences between regions where cells are actively forming lamellipodia and areas where they are not. Our collaborator, Maureen Cercy in the laboratory of Grégory Giannone, University of Bordeaux, investigated the distribution of one such NPF - the WAVE Regulatory complex (WRC) - in the lamellipodial structures of B16-F1 melanoma cells using a quantitative super-resolution imaging method, qPAINT [113], and identified significant differences in its distribution based on its localization within the cells.

To investigate the localization of the WAVE Regulatory Complex (WRC), a crucial NPF regulating actin dynamics at lamellipodia, experiments were conducted on B16-F1 cells with knockouts for both WAVE1 and WAVE2. A recombinant version of the WAVE2 subunit tagged with C-terminal GFP (WAVE2-GFP) was ectopically expressed in these knockout cells to study its localization. As anticipated, the recombinant WAVE2-GFP localizes to the membrane where it is assumed to function in generating branched actin structures (fig. 5.8A, left panel). To visualize the distribution of WAVE molecules with higher resolution, DNA-PAINT was employed. This involved adding an anti-GFP nanobody conjugated with a docking DNA that later hybridized with a complementary DNA strand conjugated to the fluorescent dye Cy3B (fig. 5.8A, right panel).

The distribution of WRC at the lamellipodial tip was analyzed both in the direction of propagation (wave front) and away from it (wave back), as illustrated in fig. 5.8B. While

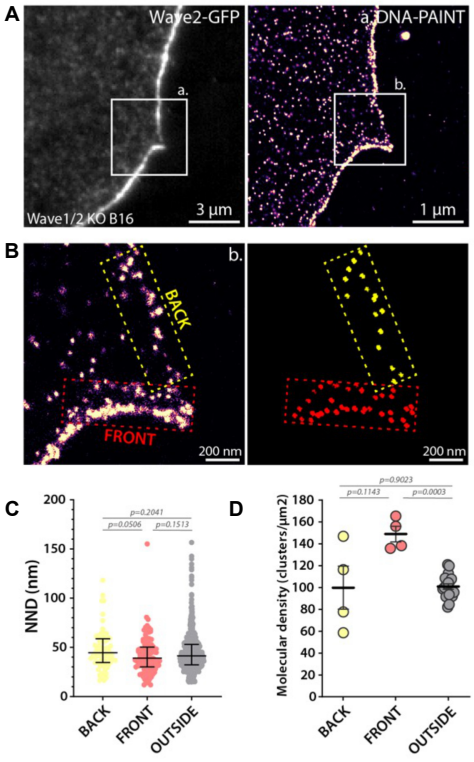

Figure 5.8: Distribution of WRC at the lamellipodia. A) Localization of WAVE2-GFP at the lamellipodial tip of WAVE1/2-KO B16-F1 cells. Left panel: Shows an image from GFP fluorescence. Right panel: Displays a super-resolution image with Cy3B fluorescence. **B)** Localization of WRC at the wave-front (FRONT) and wave-back (BACK) of the lamellipodial tip. Right panel illustrates clusters of WRC identified from the super-resolution data. **C)** Nearest neighbor distances of WRC clusters at the wave-front (FRONT), wave-back (BACK), and outside the lamellipodial tip (OUTSIDE). **D)** Molecular densities of WRC clusters at the wave-front (FRONT), wave-back (BACK), and outside the lamellipodial tip (OUTSIDE).

these regions are in immediate pyhsical proximity, only the wave front region spawns a branched actin network, whereas the wave back does not. WRC clusters were precisely identified with a localization accuracy of up to 7 nm and their differences in density and inter-cluster distances were compared (fig. 5.8B, right panel). The average density of WRC clusters appeared higher in the wave front when compared to a region outside the lamellipodia and the wave back: 150, 100, and 58 WRC clusters/μm^2 respectively (fig. 5.8D). Furthermore, the average nearest neighbor distances for WRCs were smallest for those observed within the wave front (42 nm), compared to those in a region outside the lamellipodia or at the back of the wave (45 and 47 nm, respectively, fig. 5.8C).

Taken together, these findings suggest that membrane areas that assemble a branched actin network, exhibit a denser concentration of NPFs. This increased density is also associated with shorter intermolecular distances between neighboring NPF molecules at these active sites. This indicates that NPF density *in vivo* is a crucial determinant of nucleation activity.

5.2.4 Density controls NPF activity in a switch-like manner

In the preceding sections, I have underscored the significance of recruiting NPFs to the membrane. A key distinction between membrane-recruited NPFs and their soluble counterparts lies in the higher local density of NPF on the 2D membrane compared to the soluble NPF, which freely diffuses in 3D. The data presented in the previous section implies a higher NPF local density at sites of activity compared to other areas. Consequently, one may ask if regulating NPF density could also control its activity.

To determine if NPF density on membranes influences its activity, I designed an experiment to systematically control the NPF density on membranes and test their nucleation activity under metastable conditions. To manipulate the density of NPFs integrated into membrane coated beads, I mixed NPFs with a mock protein at varying ratios and embedded the mixture of proteins onto lipid bilayers. Given that both NPFs and the mock protein bear N-terminal His-tags, they can both adhere to the Ni-containing lipid bilayers. As a result, the NPF density corresponds to the fraction of NPF in the NPF:Mock protein ratio (fig. 5.9A). However, as the mock protein cannot activate the Arp2/3 complex, the nucleation activity is solely contingent upon the NPF density.

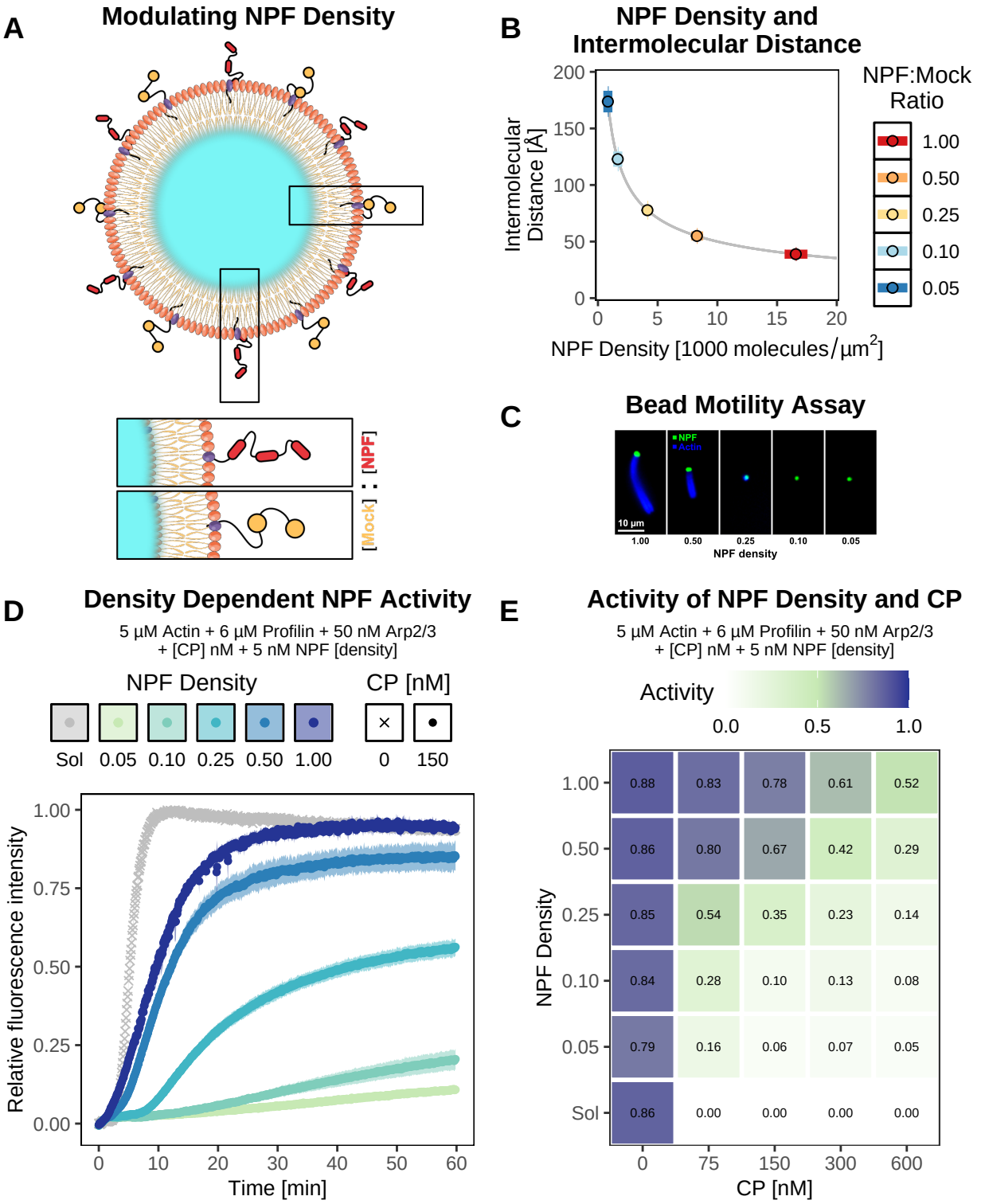

Figure 5.9: NPF density controls its activity. A) Schematic representation of modulating NPF embedding density. The NPF density on membrane-coated beads is systematically controlled by altering the ratio of His-tagged NPF (red) to another His-tagged mock protein (yellow) that binds to membranes with similar interactions but cannot nucleate filaments. *[Continued on the following page.]*

Figure 5.9: B) Molecular densities and average intermolecular distances of NPFs obtained from various embedding ratios (as indicated by color). The molecular densities (x-axis) were calculated based on the concentration of NPFs embedded onto membrane-coated beads per unit area. Average intermolecular distances (y-axis) were derived from molecular densities. **B)** TIRF microscopy images of actin networks grown on silica microspheres coated with lipid bilayers containing NPFs of varying densities (from 1.00 to 0.05, left to right). Actin polymerization reactions were performed under metastable conditions using 5 μM actin, 6 μM profilin, 50 nM Arp2/3 complex, 150 nM CP, and membrane-bound NPFs of varying densities. The images were taken after 5 minutes of reaction, fixed with Phalloidin (5 μM) and Latrunculin A (5 μM), and visualized under TIRF microscopy. Actin was labeled with LifeAct conjugated to AlexaFluor488, while NPFs were labeled with Cy3. **D)** Time course of actin nucleation and polymerization with membrane-bound NPFs at varying densities. Actin polymerization reactions were carried out under metastable conditions using 5 μM actin, 6 μM profilin, 50 nM Arp2/3 complex, 150 nM CP, and either membrane-bound (points) or soluble (Sol) NPFs with varying densities (as indicated by color). The concentration of NPF was kept constant at 5 nM regardless of the NPF density. A control reaction was carried out in the absence of CP (crosses) and with soluble NPF (Sol). **E)** Activity matrix of the polymerization reactions in D, illustrating variations in concentrations of CP (x-axis) and NPF densities (y-axis). The shade of each tile corresponds to the activity level, ranging from 0 (white) to 1 (blue), determined over a 60-minute time course. Data points in C, and D represent average values obtained from 5 and 6 replicates, respectively. The shaded areas surrounding data points in D denote standard deviations, while error lines in C indicate the standard deviation of measurements. The activity in E is derived from the averaged area under the polymerization curves such as in D. Each tile contains averages calculated from 6 or more replicates.

By embedding mixtures of NPF and mock protein at differing ratios, I produced membrane-coated beads with varying NPF molecular densities. I quantified the NPF densities of these beads by determining the total NPF concentration incorporated on the membranes and calculating the number of NPF molecules per unit area on the silica microspheres (fig. 5.9B). The attained NPF densities ranged from roughly 900 to 17,000 molecules/μm^2. Consequently, these densities encompassed an average intermolecular distance between 38 and 174 $\mathring{A}$. These molecular desnities are in line with NPF densities previously observed in cells [114, 115, 116].

To examine the influence of varying NPF densities on membranes, my initial investigation focused on their ability to generate branched actin networks on beads under metastable conditions and observing the morphology of generated actin tails using epifluorescence microscopy (fig. 5.9C). Beads with higher NPF densities (1.00 and 0.50)

successfully produced coherent actin tails, whereas those with lower densities either did not produce any discernible actin tail (densities 0.10 and 0.05) or generated a rudimentary actin tail, as seen in beads with an NPF density of 0.25 (fig. 5.9C). These findings suggest that branched actin tails only emerge from beads with higher densities and do not form at lower densities. However, it is also plausible that at lower NPF densities the actin network is sparse and undetectable due to dispersed and unconnected filament arbors. To prevent overlooking such instances, I performed pyrene assays with silica microspheres harboring varying NPF densities and measured the time course of actin polymerization. These experiments report the total amount of actin polymerized at any given moment during the reaction and are less likely to be misinterpreted due to variations in actin network density as inspected with microscopy. Moreover, they allow us to monitor the kinetics of the reaction.

To investigate the role of NPF densities on nucleation, I performed pyrene assays under metastable conditions (5 µM Actin, 6 µM Profilin, 50 nM Arp2/3 complex and 150 nM CP), maintaining a consistent NPF concentration (5 nM) but examining various NPF densities (fig. 5.9D). The experiments revealed three primary outcomes. First and foremost, both the rate of nucleation and the maximum amount of actin polymerized at saturation were influenced by NPF density. Secondly, the nucleation rate was nonlinearly impacted by NPF density, as evidenced by the slopes of the reaction curves. Lastly, some minimal nucleation was detected in all membrane-bound NPF densities, even when the NPF concentration was as low as 5 nM - a concentration previously shown to fail to nucleate in solution at CP concentrations of 37.5 nM or above (fig. 5.6D). Interestingly, the nonlinear behavior of nucleation in pyrene assays with membrane-coated NPFs of varying densities displays a qualitative resemblance to those previously reported in my bead motility assays. Specifically, higher densities yield coherent actin tails, lower densities do not produce any discernible actin tail, and moderate densities generate rudimentary actin tails (fig. 5.9C).

A better appreciation of the nonlinearity in NPF nucleation activity is obtained from the activity plot comparing varying NPF densities against different concentrations of CP (fig. 5.9E). At a concentration of 5 nM NPF, its soluble form (Sol) only nucleates in the absence of CP and exhibits no nucleation above 37.5 nM CP (fig. 5.6D and fig. 5.9E). However, membrane-bound NPF at the same overall concentration (5 nM), maintains over 50% of its nucleation activity in at least one density regime across all measured CP concentrations. Additionally, the density threshold surpassing which 50% of the

nucleation activity is maintained shifts according to the CP concentration. Specifically, this lowest density with more than 50% of nucleation activity shifts from 0.25 to 0.50 and eventually to 1.00 as we increase the CP concentration from 75 nM to 150 nM and ultimately to 300 nM (fig. 5.9). In summary, these findings reveal that NPF density influences nucleation activity nonlinearly, which can be fine-tuned by the CP concentration.

So far, I have demonstrated that NPF densities govern nucleation activity. However, a crucial factor to consider is that the average intermolecular distance between NPFs decreases as molecular density increases (fig. 5.9B). This observation is significant because a single Arp2/3 complex molecule has been documented to have the capacity to interact with two NPF molecules concurrently (fig. 5.10A) [117]. With increasing densities and shrinking intermolecular distances, it might be probable that the likelihood of two NPFs engaging an Arp2/3 complex molecule increases. As a consequence, nucleation activity under metastable conditions could be due to the simultaneous binding of two NPFs to one Arp2/3 molecule. To disentangle the role of concurrently binding two NPFs on a single Arp2/3 complex from a strictly density-dependent regulatory mechanism, I assessed the impact of a dimeric variant of NPF on nucleation activity.

I generated dimeric variants of constitutively active NPFs by covalently linking two molecules of NPF at the N-terminus with a bis-maleimide linker. Dimeric variants of NPFs have been shown to exhibit higher nucleation activity than their monomeric counterparts in solution assays [103, 118]. In agreement with this, I observed higher nucleation rates in pyrene assays with dimeric NPFs compared to their monomeric counterparts in solution at equal concentrations (fig. 5.10B).

Although dimeric variants of NPFs exhibit more potent nucleation activity than their monomeric counterparts, they still failed to induce robust and potent actin filament nucleation under metastable conditions (approximately 15-20%, fig. 5.10D). Moreover, experiments involving the embedding of dimeric variants of NPFs on membranes at varying densities produced results akin to those obtained with monomeric NPFs. Specifically, the nucleation activity was directly proportional to the density of NPF present on the membrane (fig. 5.10C and E). These findings contradict the hypothesis that simultaneous binding of two NPFs onto the Arp2/3 complex is the mechanism responsible for overcoming metastability. If simultaneous binding of two NPFs onto the Arp2/3 complex would have been the reason for overcoming metastability, then the nucleation activity

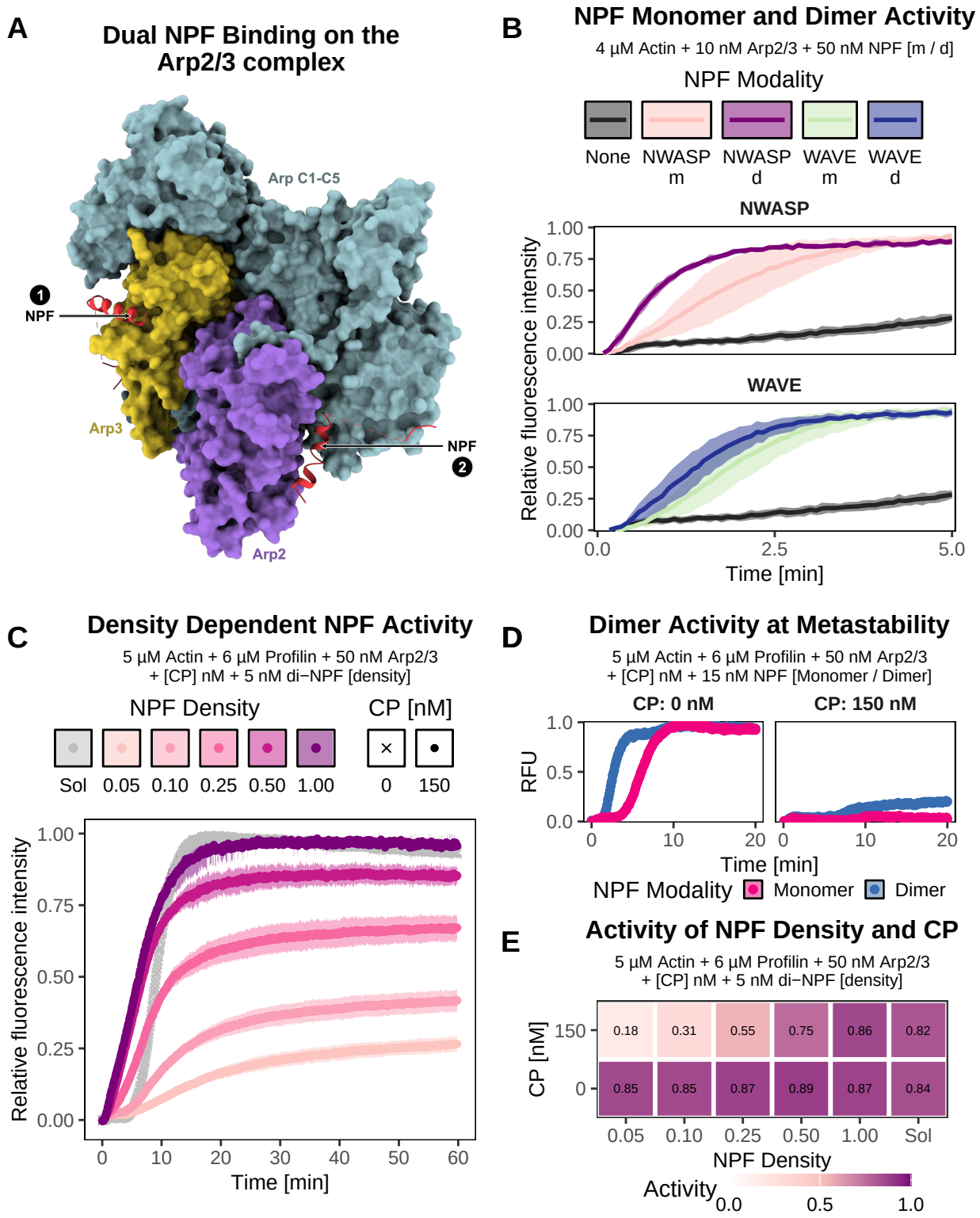

Figure 5.10: Influence of dimerization on NPF activity. A) Schematic representation of Arp2/3 complex bound to two NPF molecules simultaneously. Arp2/3 complex is depicted as a molecular surface, with its domains colored differently (Arp2 - blue, Arp3 - yellow, and ArpC1-C5 - green). NPFs are shown in ribbon diagram form (red), and the binding sites for the two NPF molecules are denoted by arrows. *[Continued on the following page.]*

Figure 5.10: B) Comparison of activity between monomeric and dimeric NPFs. Time course of actin nucleation and polymerization for reactions containing 4 μM actin, 10 nM Arp2/3 complex, and 50 nM NPF, either in its monomeric form (NWASP-m and WAVE-m) or dimeric form (NWASP-d and WAVE-d). Activity levels for both NWASP (upper panel) and WAVE (lower panel) were compared between their monomeric and dimeric states. A control reaction was carried out without the presence of any NPF (black). **C)** Time course of actin nucleation and polymerization with membrane-bound dimeric NPFs at varying densities. Actin polymerization reactions were conducted under metastable conditions using 5 μM actin, 6 μM profilin, 50 nM Arp2/3 complex, 150 nM CP, and either membrane-bound (points) or soluble (Sol) dimeric NPFs with varying densities (as indicated by color). The concentration of NPF was kept constant at 5 nM regardless of density. A control reaction was carried out without CP (crosses) and with soluble dimeric NPF (Sol). **D** The activity of monomeric (pink) and dimeric (blue) NPF variants, in the presence and absence of CP, is depicted in the figure. In the absence of CP (left panel), both types of NPF nucleate. However, only the dimeric NPF variant partially nucleates under metastable conditions (right panel). **E)** Activity matrix of the polymerization reactions in C, illustrating variations in membrane-bound dimeric NPF densities (x-axis) and concentrations of CP (y-axis). The shade of each tile corresponds to the activity level, ranging from 0 (white) to 1 (dark pink), determined over a 60-minute time course. Data points in B, C and D represent average values obtained from 3, 6 and 6 replicates, respectively. The shaded areas surrounding data points in B and C denote standard deviations in the measurements. The activity in E is derived from the averaged area under the polymerization curves such as in C. Each tile contains averages calculated from 6 replicates. RFU is relative fluorescence unit.

should not have correlated with the NPF density for dimeric variants as each individual dimeric molecule, regardless of overall NPF density, can still occupy both binding sites on the Arp2/3 complex. Collectively, these results suggest that NPF density plays a role in modulating NPF nucleation activity and not the dual binding of NPFs onto the Arp2/3 complex.

A comparison of the nucleation activity between the two NPF variants reveals that while dimeric NPF variants do not completely alleviate metastability on their own, they consistently exhibit better nucleation activity in both soluble form and membrane-bound form (fig. 5.11A). This observation is also apparent when examining their nucleation efficiencies side by side in the activity matrices (fig. 5.11B). Nevertheless, an overall density dependence is observable for both monomeric and dimeric variants of NPF. In general, high densities (lower intermolecular distances) of NPF result in the highest

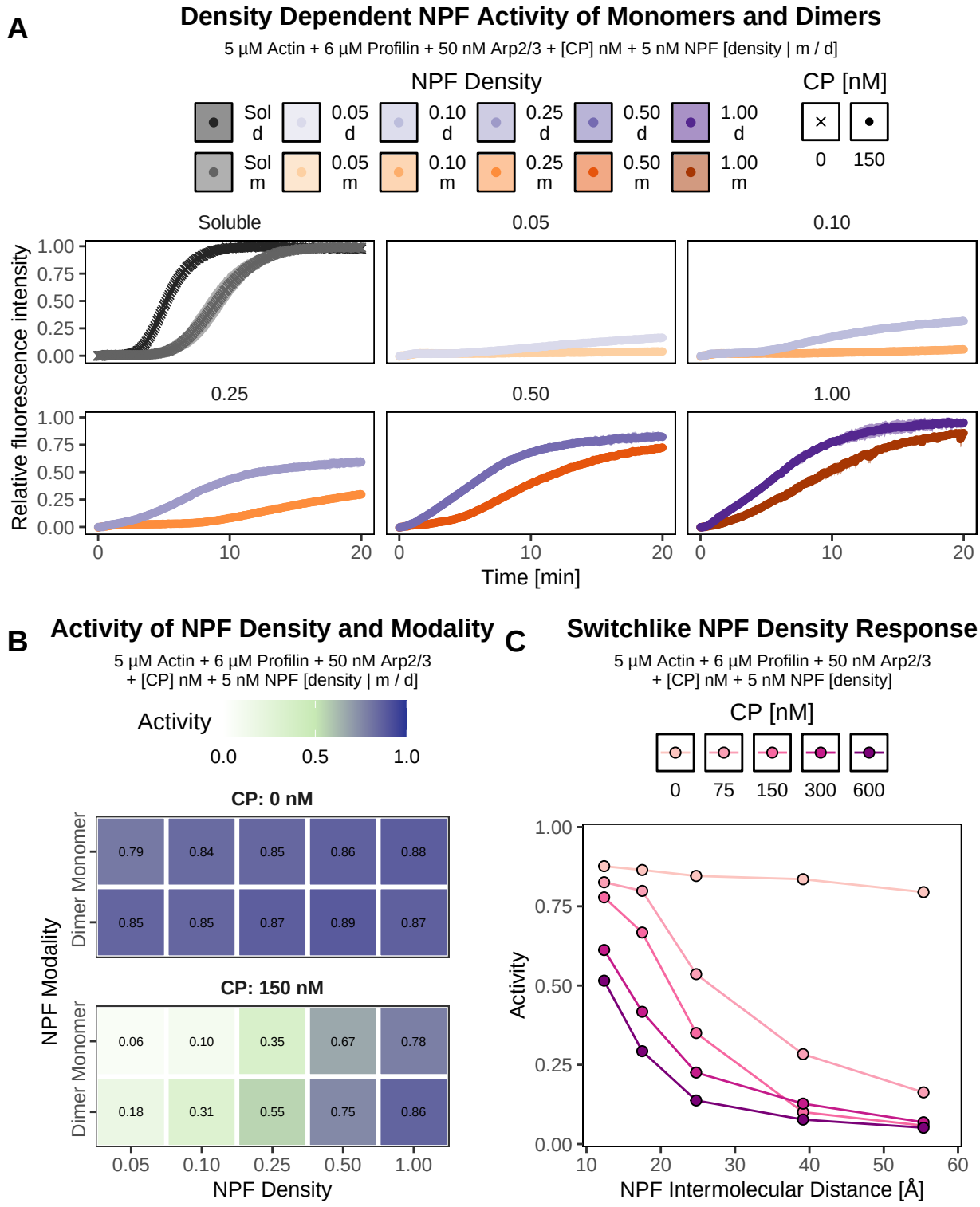

Figure 5.11: NPF densities regulate their activity in a switch-like manner. A) Time course of actin nucleation and polymerization comparing membrane-bound monomeric and dimeric NPFs at varying densities. Actin polymerization reactions were conducted under metastable conditions using a constant concentration of 5 μM actin, 6 μM profilin, 50 nM Arp2/3 complex, and 150 nM CP. *[Continued on the following page.]*

Figure 5.11: The NPFs were presented in two modalities: monomers and dimers. Different NPF densities, indicated by color, are illustrated in each subpanel. Each subpanel compares the activity of the monomeric version of the NPF (m) with its dimeric version (d) at a specific membrane density. The concentration of NPF was kept constant at 5 nM regardless of the NPF density or modality. Control reactions were performed without CP (crosses) and with soluble NPFs (Sol-m and Sol-d). **B)** Activity matrix of the polymerization reactions in A, demonstrating variations in NPF density (x-axis) and NPF modality (monomer or dimer, y-axis). The shade of each tile corresponds to the activity level, ranging from 0 (white) to 1 (blue), determined over a 60-minute time course. **C)** Activity of various NPF densities plotted against the average intermolecular distances of the NPFs at those densities. Actin polymerization reactions were carried out with 5 μM actin, 6 μM profilin, 50 nM Arp2/3 complex, and varying concentrations of CP (indicated by color). The NPF densities, expressed as their average intermolecular distance in x-axis, were also varied. Data points in A and C represent the average values obtained from 6 replicates for either modality. Standard deviations in the measurements are denoted by shaded areas surrounding data points in A. The activity in B is calculated as the averaged area under the polymerization curves such as in A. Each tile contains averages calculated from 6 or more replicates.

nucleation activity, followed by a sigmoidal decrease in activity towards lower densities (higher intermolecular distances). The density dependence is further fine-tuned by the CP concentration present in the reaction, which steepens the slope of the sigmoid with increasing CP concentrations (fig. 5.11C).

Given the possibility that high densities of NPF can generate available filaments for neighboring NPF, as close as 40 $\mathring{A}$ apart, the issue of mother filament availability is not problematic when nucleated on high-density NPF-coated beads. Additionally, it is plausible that mother filaments might be limited in metastable reactions under solution conditions. To validate this hypothesis, I devised an experiment where I supplied excess stabilized mother filaments to a reaction under metastable conditions. However, despite the inclusion of a dimeric NPF variant, the reaction remained metastable in solution even with supplemented stabilized mother filaments (fig. 5.12A). Furthermore, the reaction with NPF-coated beads displayed sensitivity to dimeric NPF densities and heightened nucleation activity at higher densities, regardless of the presence of absence of stabilized mother filaments (fig. 5.12B). These findings suggest that the availability of mother filaments and dimer NPFs combined cannot overcome metastability.

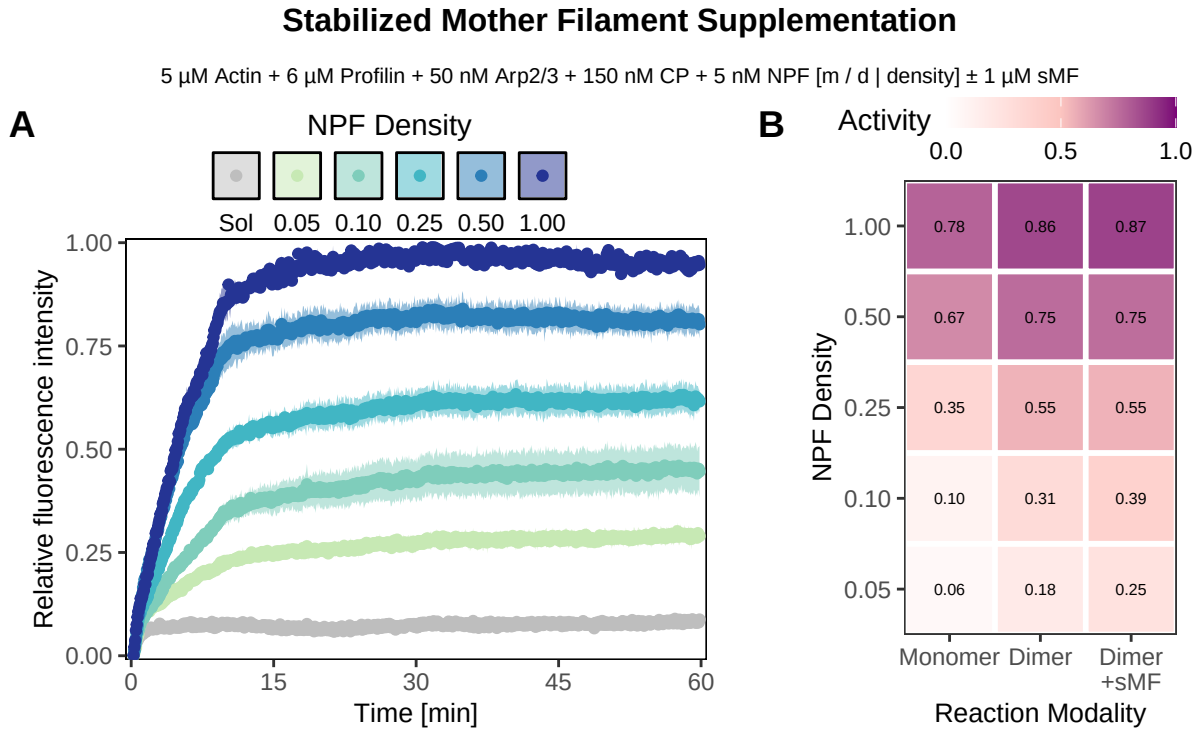

Figure 5.12: Mother filament supplementation. **A.** Time course of actin nucleation and polymerization with membrane-bound dimeric NPFs at varying densities, supplemented with 1 μM stabilized mother filaments (sMF). **B.** Comparison of activity of membrane-bound monomeric or dimeric NPFs in the presence or absence of stabilized mother filaments. Actin polymerization reactions were conducted under metastable conditions, using a constant concentration of 5 μM actin, 6 μM profilin, 50 nM Arp2/3 complex, 150 nM CP, and 5 nM NPF. Standard deviations in the measurements are denoted by shaded areas surrounding data points in A. The activity in B is calculated as the averaged area under the polymerization curves, such as those shown in A. Each tile represents the averages calculated from 6 or more replicates for experiments without stabilized mother filaments (sMF), and 2 replicates in the presence of sMF.

Collectively, these findings clearly demonstrate how the density of NPFs on a membrane can influence their nucleation efficiency, even in the absence of an autoinhibitory mechanism. Moreover, although dimeric NPFs exhibit higher nucleation activity, they do not surmount metastability and are similarly sensitive to a density-based control mechanism as their monomeric counterparts.

6 Discussion and Conclusions

6.0.1 Temporal control of P_i release

In the first part of this thesis, I explored the underlying mechanism of P_i release from actin filaments through computational simulations. Using stochastic simulation, I modeled an aging filament that polymerizes and depolymerizes in succession. During this process, as the filament ages, the bound nucleotides on actin subunits transition from ATP to ADP-P_i and finally to ADP. In the polymerization phase, subunits with ATP hydrolyze their nucleotide rapidly, but a finite number of ATP-bound subunits remain due to newly added subunits. Subsequently, a cap of ADP-P_i is formed that travels along with the polymerizing end. Simultaneously, the amount of ADP subunits continuously increases due to hydrolysis and successive P_i release towards the older parts of the filament. Once depolymerization commences, all ATP subunits are hydrolyzed or depolymerized within a short time frame. Subsequently, depolymerization proceeds through either ADP-P_i or ADP subunits. The filament's depolymerization rate is contingent on the nucleotide state of its terminal subunit, leading to an initial nonlinear change in filament lengths and providing a valuable readout for measuring P_i release rates.

In my stochastic simulation model, several assumptions warrant further examination. Firstly, the assumption that ATP hydrolysis is a stochastic process was made based on comparisons with P_i release. However, it is essential to experimentally verify this assumption. Moreover, there may exist a mixed mode of action where hydrolysis displays both deterministic and stochastic properties. For instance, the terminal subunit of the actin filament might not hydrolyze its bound nucleotide, while ATP hydrolysis in other regions could be stochastic. This possibility should be thoroughly investigated due to its potential consequences on polymerization dynamics, particularly depolymerization rates.

Additionally, the rotameric states of side chains in the nucleotide cleft of internal subunits appear to differ from those of the terminal subunit. These differences likely have implications for ATP hydrolysis and thus need to be explored further to accurately model actin polymerization and depolymerization kinetics. Indeed our recent structures indicated that the ultimate subunit differs in structural elements responsible for ATP hydrolysis and is likely less catalyticall active compared to the penultimate or internal subunits [106]. Future studies should focus on addressing these assumptions experimentally, employing techniques as established here to directly observe the dynamics of ATP hydrolysis and its relationship with actin filament growth and shrinkage. However, my simulations indicate that these experiments will be very challenging, given the small size of the ATP cap and the rapid decay of ATP after flushing out monomeric actin from the system with buffer to initiate depolymerization conditions. Nevertheless, such investigations will be crucial to gaining a more comprehensive understanding of actin polymerization and depolymerization mechanisms at the molecular level.

Results from the Cryo-EM experiments on the actin filament barbed end revealed that structurally, the terminal subunit, characterized by a faster P_i release rate, exhibits surprisingly small differences compared to the internal subunit, which displays a significantly slower P_i release rate. The overall backbone Cα RMSD between the two subunits was less than 1 $\mathring{A}$. However, upon closer examination of the nucleotide-binding cavity and the proposed P_i exit site, the backdoor, it became apparent that this area in the internal subunit was predominantly occluded due to a complex hydrogen bonding network that restricted P_i from escaping. Furthermore, enhanced sampling MD simulations identified two major P_i release pathways through residues N111 and R183, both of which have previously been associated with actin-related diseases. These findings suggest that subtle differences adjacent to the nucleotide-binding cavity structure between terminal and internal subunits play a crucial role in regulating P_i release rates from the actin filament.

Taken together, these findings from the experimental investigations of the actin mutant harboring a mutation at the pivotal N111 residue have shed new light on the role of this key residue in the intricate hydrogen bonding network that forms the closed backdoor in internal actin subunits. These experiments revealed that disrupting the hydrogen bonding network results in expedited P_i release from actin filaments.

The structures of actin subunits reveal that the P_i molecule is obstructed from exiting due to a network of hydrogen bonds, indicating its inhibition from leaving the subunit. Furthermore, the distances between the Mg^{2+} ion and the P_i molecule suggest the feasibility of a coordinate bond between them. There have been reports suggesting an increased stiffness in actin filaments comprised of ADP P_i subunits compared to ADP-subunits [119]. The influence of the P_i molecule on the mechanical rigidity of actin filaments and how external mechanical forces may affect its release is yet to be fully understood, warranting further investigation into the feedback mechanism between external forces applied on the filament and P_i release kinetics.

Bulk assays and single-filament experiments both demonstrated an instantaneous P_i release from N111S mutant actin filaments, as evidenced by a lack of a detectable time delay between polymerization and P_i release measurements, and the absence of the characteristic transition between slower ADP P_i subunit velocities and faster ADP subunit velocities. Therefore, both experimental modalities estimated a significantly increased P_i release rate (≥ 0.1 s^1) for the mutant compared to wild-type actin's P_i release rate (about 0.007 s^1), providing compelling evidence that P_i release is inherently slower in internal actin subunits due to their closed backdoors, of which N111 is a crucial constituent. It should be noted that the estimated P_i release rate for the N111S mutant only constitutes a lower bound and the true rate of release might even be much higher.

A notable observation from the single filament depolymerization experiments of the N111S mutant was the absence of a slow ADP P_i depolymerization velocity. However, this mutant displays a significantly higher overall depolymerization velocity compared to wt-actin (14.7 versus 6.6 s^{-1} respectively). Although the mutation is not located near a neighboring subunit interface, it seems that an enhanced overall depolymerization velocity arises as a result. Further investigation is required to determine the underlying cause for this observation. As the N111 residue plays a crucial role within an intricate hydrogen bonding network, it could be hypothesized that alterations in the overall hydrogen bonding network and potential changes in the arrangement of water molecules involved in long-range cross hydrogen bonds may contribute to the observed increase in the overall depolymerization velocity.

Collectively, these results contribute significantly to our understanding of the regulatory mechanisms governing the termporal dynamics of P_i release from actin filaments and further underscore the importance of investigating these molecular processes at an atomic

level for developing a better model of actin dynamics and to understand what goes wrong in actin-related diseases.

6.0.2 Spatial control of NPF activity

In the latter portion of this thesis, I investigated the regulatory mechanisms behind the Arp2/3 complex activating function of NPFs. To explore the kinetic parameters relavent to boundary conditions observed in a cell, I reconstituted an *in vitro* system containing the minimal constituents required for branched actin nucleation. During these investigations, two metastable regimes were identified where the system was kinetically kept away from thermodynamic equilibrium, one devoid of nucleators and another in their presence.

Monomeric actin above its critical concentration undergoes spontaneous nucleation but that is prohibited by profilin, which maintained the system in a metastable state. Despite sufficient actin for filament formation, profilin prevented polymerization by substantially diminishing the likelihood of nucleus formation that could further elongate and drive the reaction towards equilibrium. However, this metastable regime was unstable as any emerging nuclei were prone to immediate elongation until the process was completed.

In contrast, with the presence of Arp2/3 complexes and constitutively active NPFs, a pool of profilin-actin could rapidly nucleate branched actin filaments. Upon addition of CP, the system entered a different metastable state where it possessed the catalyst required for nucleation but failed to nucleate and polymerize. Furthermore, this state was more stable than the previously identified one because profilin prevented spontaneous nucleation and CP ensured that any emerging nuclei could be capped and arrested from further elongation.

The presence of the second scenario raised an intriguing conundrum, as cells manage to successfully nucleate branched actin filaments under similar concentrations of Arp2/3 complex, NPFs, and CP.

Although the solution polymerization reaction is maintained in a metastable state in the presence of CP, the origin of this metastability in the molecular context remains unclear. A conceivable explanation could be that CP impedes the formation of sufficiently large mother filaments, which can serve as a substrate for Arp2/3 complex to branch from. However, preliminary experiments with pre-formed stabilized filaments suggest that an excess of mother filaments fails to rescue the system from metastability. In the absence of definitive experimental evidence, it might prove beneficial to carry out reaction-diffusion

simulations where individual components are allowed to evolve from a starting condition reminiscent of the metastable conditions. These simulations may provide insights into how the reaction is kinetically regulated even when mother filaments are not limiting in supply.

The disparity between my *in vitro* reconstitution results and the behavior of NPFs in cells prompted me to further investigating the boundary conditions within cells where nucleation occurs. One essential difference between *in vitro* conditions and those in cells was that nucleation activity in cells was confined to the plasma membrane. Experiments involving NPFs bound to lipid bilayers on silica microspheres mimicking the boundary conditions presented by membrane-bound NPFs in cells exhibited rapid nucleation under conditions that would otherwise fail to do so in the solution based *in vitro* reconstitution experiments. This result underscored the significance of boundary conditions on NPF function and actin nucleation dynamics within cells.

The recruitment of NPFs onto cellular membranes presents a significant regulatory event. In experiments using WAVE1/2 knockout cells, ectopically expressed WAVE2-GFP subunits could be localized to the lamellipodial tip. Moreover, the densities of WRCs varied depending on the site of activity. Specifically, WRC membrane densities were the highest at the front edge of the lamellipodia tip as compared to the back edge or regions outside the lamellipodial tip. Additionally, the nearest neighbor distances of WRC clusters appeared to be smaller in areas with higher nucleation activity than in those with lower activity. These findings suggest that the density of NPFs is a critical regulatory element for their activity within cells.

To investigate causally the role of NPF density on its nucleation activity, I conducted experiments allowing me to systematically vary NPF density and assess its effect. This was accomplished by designing experiments where I could manipulate NPF densities within a range of 900 to 16,000 molecules$\cdot\mu\text{m}^{-2}$, encompassing an average intermolecular distance ranging from approximately 38 to 174 $\mathring{A}$.

Given that the Arp2/3 complex can bind simultaneously to two NPF molecules and dimeric variants of NPF exhibit higher nucleation activity than their monomeric counterparts, it was crucial to determine whether this heightened nucleation activity resulted from a higher probability of simultaneous binding of two NPF molecules or purely due to increased density. In experiments with dimeric variants of NPF, no significant nu-

cleation occurred under metastable conditions in contrast to instances with higher NPF densities that successfully nucleated and rapidly polymerized under the same conditions. Moreover, the proportional increase in nucleation activity to the NPF density on membranes persisted even with dimeric variants, suggesting that nucleation activity remained sensitive to NPF density in these cases as well.

In summary, my investigation unveiled similarities and differences between the monomeric and dimeric variants of NPF concerning their nucleation activities. Notably, the dimeric variants consistently outperformed the monomeric forms in both soluble and membrane-bound scenarios. However, it is important to emphasize that both variants displayed identical density dependence in their nucleation activity. Dimeric NPFs failed to induce significant nucleation in solution under realistic biochemical conditions and required membrane recruitment for full Arp2/3 complex activation.

Moreover, these results suggest that NPF nucleation activity depends on its density in a switch-like manner with higher densities being maximally active and the activity falling sigmoidally as average intermolecular distances between NPFs increase. Remarkably, the steepness of this sigmoidal relationship could be modulated by modulating CP concentrations, shedding light on a potential regulatory mechanism governing NPF-mediated actin nucleation dynamics. Furthermore, this newly discovered switch-like density-dependent mechanism supercedes the autoinhibitory regulation mechanism because it operates independently of its presence or absence.

These results distinctly underscore the role of NPF density in nucleation activity. Nevertheless, it is yet unclear how density manages to control nucleation at the molecular scale. Considering that NPF dimerization alone does not trigger nucleation under metastable conditions, it leaves us with a question as to how increased densities contribute to nucleation. A plausible explanation could be that a dense layer of NPFs interacts with the Arp2/3 complex and allows it to sample the 2D surface of NPFs through successive swapping of NFP partners until a mother filament is discovered, which in turn initiates nucleation. This approach would significantly accelerate the search process for the Arp2/3 complex from a 3D environment into a more manageable 2D problem by the principle of dimensionality reduction [120]. Experiments employing single molecule tracking of the Arp2/3 complex on varying NPF density surfaces could potentially elucidate how NPF density influences nucleation at a molecular scale.

In conclusion, the findings from the research conducted throughout this thesis reveal two significant aspects of actin dynamics regulation. The initial component of the thesis explores a mechanism controlling P_i release from actin filaments, which represents a temporal control of filament aging. Subsequently, the second part of the thesis introduces a novel density-dependent mechanism that regulates NPF activity, emphasizing a spatial control over actin dynamics.

7 Materials and Methods

7.1 Protein Purification

This section includes the detailed protocols for purifying various proteins that have been utilized in the course of this study.

7.1.1 α-actin

In order to purify α-actin, acetone powder was first solubilized in 20 mL of G-Buffer (2 mM Tris base pH 7.0, 0.1 mM $CaCl_2$, 0.2 mM ATP, 0.1 μg/mL NaN_3, 0.5 mM TCEP) per gram of acetone powder at a temperature of 10 °C and then stirred at 250 rpm for 30 minutes at 4 °C. The resulting solution was then centrifuged at 15,000 rcf for one hour at 4 °C, and the supernatant was collected. To initiate polymerization, ATP and 10X KMEI (100 mM Imidazole pH 7.0, 500 mM KCl, 15 mM $MgCl_2$, 10 mM EGTA) were added to the supernatant to reach a final concentration of 100 μM and 1x respectively. The reaction was carried out at room temperature for an hour and then at 4 °C for another hour while being gently stirred at 50 rpm in order to prevent sedimentation. After completing the polymerization process, KCl was added to the solution until it reached a final concentration of 800 mM and slowly mixed using a magnetic stirrer at the rate of 200 rpm for 10 minutes. The resulting mixture was then centrifuged again at 142,000 rcf for an hour at 4 °C and the supernatant was discarded. The translucent pellet of α-actin was resuspended in F-Buffer (1x KMEI, 2 mM Tris-Cl pH 8.0, 0.1 mM $CaCl_2$, 0.2 mM ATP, 0.1 μg/mL NaN_3, 0.5 mM TCEP) and dialyzed against F-Buffer at 4 °C until needed.

Monomeric α-actin was acquired by dialyzing polymeric α-actin into G-Buffer, followed by gel filtration. To do this, polymeric actin was initially centrifuged at 350,000 rcf for

30 minutes at 4 °C, and the pellet was resuspended in G-Buffer before being dialyzed, while gently being stirred, for 5 days at 4°C. Subsequently, the dialysate was centrifuged at 350,000 rcf for 30 minutes at 4 °C, to separate any remaining polymeric actin and the supernatant was gel filtered into G-Buffer using a Superdex 75 HiLoad 16/600 column. Fractions including and following the peak fractions were stored separately at 4°C.

7.1.2 β,γ-actin

Bovine thymus (600 g) was severed into smaller pieces and homogenized in the Holo-Extraction Buffer (10 mM Tris-Cl pH 8.0, 7.5 mM $CaCl_2$, 1 mM ATP, 5 mM β-Mercaptoethanol, 0.03 mg/mL Benzamidine, 1 mM PMSF, 0.04 mg/mL Trypsin Inhibitor, 0.02 mg/mL Leupeptin, 0.01 mg/mL Pepstatin, 0.01 mg/mL Aprotinin). An additional 2.5 mM β-Mercaptoethanol was added to the homogenized mixture, and the pH was adjusted to 8.0 with 1 M Tris base if required. The resulting homogenate was centrifuged at 30,000 rcf for 40 minutes at 4 °C, and the resulting supernatant was filtered through a nylon membrane (pore size: 100 μm). After filtration, the resulting filtrate was centrifuged at 142,000 rcf for 40 minutes at 4 °C. Any residual layer of lipid that appeared on the air-water interface was carefully aspirated off after centrifugation. KCl and Imidazole were added to the resulting solution to final concentrations of 50 mM and 20 mM, respectively. A deca-His tagged version of the C-terminal half of Gelsolin including the 4-6 th actin binding repeats (G4-6) was then added to this solution at a ratio of 4 mg per gram of thymus used for the purification. After adding G4-6, the solution was gently stirred for 2 hours at 4 °C.

The resulting mixture was dialyzed overnight against IMAC Wash Buffer (10 mM Tris-Cl pH 8.0, 50 mM KCl, 20 mM Imidazole, 5 mM $CaCl_2$, 0.15 mM ATP, 5 mM β-Mercaptoethanol). The dialysate was loaded onto the Ni^{2+} superflow column the next day. Actin was eluted using Elution Buffer (10 mM Tris-Cl pH 8.0, 50 mM KCl, 20 mM Imidazole, 5 mM EGTA, 0.15 mM ATP, 5 mM β-Mercaptoethanol), with a single-step elution. Fractions containing actin were pooled together and incubated at room temperature for an hour. After an hour, polymerization was initiated by adding KMEI (10 mM Imidazole pH 7.0, 50 mM KCl, 1.5 mM $MgCl_2$, 1 mM EGTA) and 500 μM ATP to the pooled actin fractions. Polymerization was carried out at room temperature for 2-3 hours.

After polymerization, the resulting solution was centrifuged at 142,000 rcf for 40 minutes at 4 °C. The translucent pellet of actin was resuspended in F-Buffer and dialyzed in the same buffer at 4 °C until needed. Similar to α-actin, monomeric β,γ-actin was acquired by dialyzing the polymeric β,γ-actin into G-Buffer, followed by gel filtration as mentioned in section 8.1.1 for purification of α-actin.

7.1.3 Gelsolin (G4-6)

A recombinant version of the C-terminal half of moluse Gelsolin (G4-6) containing an N-terminal deca-His tag was expressed in *E. coli* BL21 Rosetta cells using a pCold vector. We induced G4-6 expression for 16 hours at 16 °C after the bacterial cells reached an OD600 of 1.0. Bacterial cells producing G4-6 were lysed first by dounce homogenization and then by passing through a microfluidizer at 12 kPa in Lysis Buffer (20 mM Tris-Cl pH 8.0, 300 mM KCl, 5 mM $CaCl_2$, 0.2 mM ATP, 0.5 mM β-Mercaptoethanol, 1 mM PMSF, DNAse I). After centrifugation at 50,000 rcf for 40 minutes at 4 °C, the clarified cell lysate was loaded onto a Ni^{2+} superflow column and washed with IMAC Wash Buffer (20 mM Tris-Cl pH 8.0, 300 mM KCl, 5 mM $CaCl_2$, 0.2 mM ATP, 15 mM Imidazole). Following the washing step, G4-6 was eluted with a single-step elution using IMAC Elution Buffer (20 mM Tris-Cl pH 8.0, 300 mM KCl, 5 mM $CaCl_2$, 0.2 mM ATP, 500 mM Imidazole). The resulting eluate was then concentrated and gel filtered with the Superdex 200 HiLoad 26/600 column into Storage Buffer (5 mM Tris-Cl pH 8.0, 50 mM KCl, 5 mM $CaCl_2$, 0.1 mM ATP, 0.5 mM TCEP). Fractions containing G4-6 were pooled and flash-frozen in liquid nitrogen after adding 20% glycerol. The samples were then stored at -80 °C.

7.1.4 Profilin

Human profilin-1 was expressed in *E. coli* BL21 Rosetta cells using a pET vector. After reaching an OD600 of 0.7, we induced profilin expression for 5 hours at 30 °C. Cells producing profilin were lysed by dounce homogenization and subsequent passage through a microfluidizer at 12 kPa in Lysis Buffer (10 mM Tris-Cl pH 8.0, 1 mM EDTA, 2 mM DTT, 1 mM PMSF, DNAse I). The lysate was centrifuged at 50,000 rcf for 40 minutes at 4 °C.

Ammonium sulfate was added to the clarified cell lysate slowly up to a saturation of 35% while being gently stirred for 30 minutes at 4 °C. The mixture was then centrifuged again at 50,000 rcf for 40 minutes at 4 °C to sediment the precipitated proteins, and the supernatant containing profilin was retained. Ammonium sulfate was added to the supernatant gradually to bring the saturation up to 61%, followed by stirring and centrifugation under the same conditions as before. The resulting pellet was resuspended in Lysis Buffer and dialyzed overnight at 4 °C against the same buffer.

The next morning, the pH and conductivity of the dialysate were adjusted to match those of the Lysis Buffer if necessary. The dialysate was centrifuged again at 50,000 rcf for 40 minutes at 4 °C, and the supernatant was loaded onto a DEAE column. After washing the column with DEAE Wash Buffer (10 mM Tris-Cl pH 8.0, 50 mM NaCl, 0.2 mM EDTA, 2 mM DTT, 1 mM PMSF), the flow-through containing profilin was collected and dialyzed overnight at 4 °C against HA Wash Buffer (10 mM KP_i pH 7.5, 1 mM DTT).

The next morning, the pH and conductivity of the resulting solution were adjusted to match those of the HA Wash Buffer if required. The sample was centrifuged at 50,000 rcf for 40 minutes at 4 °C, and the supernatant was loaded onto an HA column. After washing the column with HA Wash Buffer, the flow-through containing profilin was collected, concentrated, and gel filtered into Storage Buffer (10 mM Tris-Cl pH 7.5, 50 mM NaCl, 0.5 mM TCEP) using Superdex 75 HiLoad 16/600. Fractions containing profilin were pooled and flash-frozen in liquid nitrogen with the addition of 20% glycerol before storage at -80 °C.

7.1.5 Arp2/3 complex

Bovine thymus (750 g) was severed into smaller pieces and homogenized with the Extraction Buffer (40 mM Tris-Cl pH 8.0, 10 mM EGTA, 1 mM $MgCl_2$, 0.00625 mg/ml Pepstatin A, 0.005 mg/ml Aprotinin, 0.04 mg/ml STI, 0.02 mg/ml Leupeptin, 0.03 mg/ml Benzamidine, 1 mM PMSF, 1 mM DTT). The homogenate was centrifuged at 5,500 rcf for 30 minutes at 4 °C after which the supernatant was filtered through a nylon membrane (pore size: 100 μm). After filtration, the filtrate was centrifuged twice to remove any insoluble residuals. The filtrate was initially centrifuged at 15,000 rcf for 20 minutes at 4 °C and the resulting supernatant was later centrifuged at 142,000 rcf for

60 minutes at 4 °C. Any residual layer of lipid that appeared on the air-water interface was carefully aspirated off after centrifugation, and the supernatant was collected.

The resulting clarified homogenate was adjusted to a pH of 8.0 and a conductivity of 10 mS/cm if required. Following the adjustment, the resulting mixture was loaded onto a Q Sepharose Fast Flow column and washed with Q-Sepharose Buffer (20 mM Tris-Cl pH 8.0, 75 mM NaCl, 1 mM EGTA, 1 mM $MgCl_2$, 1 mM DTT, 0.002 mg/ml Leupeptin, 0.002 mg/ml Pepstatin A). The flow-through was collected during the loading and washing steps.

Ammonium sulfate was added to the flow-through slowly up to a saturation of 33% while being gently stirred for 30 minutes at 4 °C. The resulting mixture was centrifuged at 15,000 rcf for 30 minutes at 4 °C to sediment the precipitated proteins and the supernatant containing Arp2/3 complex was retained. Ammonium sulfate was added to the supernatant gradually to bring the saturation up to 50%, followed by stirring and centrifugation under the same conditions as before. The resulting pellet was resuspended in the Dialysis Buffer (5 mM Tris-Cl pH 8.0, 0.5 mM EGTA, 0.5 mM $MgCl_2$, 1 mM DTT) and dialyzed overnight.

The next morning, the dialysate was centrifuged at 142,000 rcf for 60 minutes at 4 °C following which the pH and the conductivity of the resulting supernatant were adjusted to match that of Source Q Low Buffer (10 mM Tris-Cl pH 8.0, 0.5 mM EGTA, 0.5 mM $MgCl_2$, 1 mM DTT) if required. After the adjustments, the mixture was loaded onto the Source Q column and washed with the Source Q Low Buffer. Proteins bound to the column were eluted with the Source Q High Buffer (10 mM Tris-Cl pH 8.0, 100 mM NaCl, 1 mM EGTA, 1 mM $MgCl_2$, 1 mM DTT) in a gradient elution from 0 to 100% over a volume of 1 L and the eluate was dialyzed overnight in Source S Low Buffer (10 mM PIPES pH 6.8, 1 mM EGTA, 1 mM $MgCl_2$, 1 mM DTT).

The next morning, the pH and the conductivity of the dialysate were adjusted to match that of Source S Low Buffer if required. After the adjustments, the resulting mixture was loaded onto the Source S column and washed with the Source S Low Buffer. Proteins bound to the column were eluted with the Source S High Buffer (10 mM PIPES pH 6.8, 150 mM NaCl, 1 mM EGTA, 1 mM $MgCl_2$, 1 mM DTT) in a gradient elution from 0 to 100% over a volume of 250 mL. The resulting eluate was concentrated and gel filtered into Storage Buffer (5 mM HEPES pH 7.5, 50 mM KCl, 0.5 mM EGTA, 0.5 mM

$MgCl_2$, 0.1 mM ATP, 0.2 mM TCEP) using the Superdex 200 HiLoad 16/600. Fractions containing the Arp2/3 complex were pooled and flash-frozen in liquid nitrogen with the addition of 20% glycerol before storage at -80 °C.

7.1.6 Nucleation Promoting Factors

Constitutively active versions of NPFs, human WAVE1 (amino acids 274 - 559), and human N-WASP (amino acids 275 - 505), were expressed in *E. coli* BL21 Star (DE3) pRARE using the pET vectors. The constructs were designed to express a recombinant version of the NPFs with an N-terminal deca-His tag and a KCK motif. This motif was used either for labeling with a maleimide functional group containing dye or for dimerization with bis-maleimide functional groups.

Expression was induced after reaching an OD600 of 1.0 and maintained for a period of 16 hours at 16 °C. Bacterial cells producing NPF were then lysed first by dounce homogenization and subsequently passed through a microfluidizer at 12 kPa in Lysis Buffer (50 mM NaP_i pH 7.3, 400 mM KCl, 4 mM Imidazole, 1 mM β-Mercaptoethanol, 1 mM PMSF, DNAse). The cell lysate was centrifuged at 142,000 rcf for 40 minutes at 4 °C to remove insoluble cell debris.

The clarified cell lysate was loaded onto a HiTrap Chelating HP column and washed with IMAC Wash Buffer (50 mM NaP_i pH 7.3, 400 mM KCl, 4 mM Imidazole, 1 $MgCl_2$, 0.5 mM β-Mercaptoethanol). After washing the column, bound proteins were eluted with a gradient elution from 0 to 100% into IMAC Elution Buffer (50 mM NaP_i pH 7.3, 400 mM KCl, 500 mM Imidazole, 1 $MgCl_2$, 0.5 mM β-Mercaptoethanol) for a volume of 30 mL. The resulting eluate was incubated overnight with 1:30 mass fraction of TEV protease for cleavage of the N-terminal domain of the protein.

The buffer of the resulting mixture was then exchanged into Mono Q Low Buffer (20 mM Tris-Cl pH 8.0, 50 mM NaCl, 0.5 mM EDTA, 0.5 mM TCEP) by passing it through a HiPrep 26/10 Desalting column equilibrated in the same buffer. Following the buffer exchange, the mixture was loaded onto the Mono Q 5/50 GL and washed with the Mono Q Low Buffer. Bound protein was eluted in a gradient elution from 0 to 60% of the Mono Q High Buffer (20 mM Tris-Cl pH 8.0, 1000 mM NaCl, 0.5 mM EDTA, 0.5 mM TCEP) over 30 column volumes. After the elution, fractions containing NPF were

concentrated and gel filtered into Storage Buffer (20 mM Tris-Cl pH 7.5, 150 mM NaCl, 0.1 mM EDTA, 0.5 mM TCEP) using a Superdex 75 HiLoad 26/600 column. Fractions containing the NPF were pooled and flash-frozen in liquid nitrogen with the addition of 20% glycerol before storage at -80 °C.

7.1.7 Capping Protein

Mouse heterodimeric capping protein was expressed in *E.coli* BL21 Rosetta cells by cotransforming them with the α and β subunits of the capping protein. Recombinant versions of these subunits were produced, with an N-terminal Trx-His-tag and TEV cleavage site on the α subunit, and a His-GST-tag and PreScission recognition site on the β subunit.

Expression was induced when the OD600 reached 1.0, and continued for 16 hours at 18 °C. After producing capping protein in bacterial cells, they were lysed through a combination of dounce homogenization and passage through a microfluidizer at 12 kPa in Lysis Buffer (50 mM KP_i, 400 mM NaCl, 4 mM Imidazole, 0.5 mM β-Mercaptoethanol, 2 mM PMSF, DNAse). The resulting cell lysate was centrifuged at 142,000 rcf for 40 minutes at 4 °C to remove insoluble debris.

The clarified cell lysate was loaded onto a HiTrap Chelating HP column and washed using IMAC Wash Buffer (50 mM KP_i pH 7.3, 400 mM NaCl, 4 mM Imidazole, 0.5 mM β-Mercaptoethanol, 2 mM PMSF, 0.015 mg/mL Benzamidine). Proteins that bound to the column were eluted using a gradient elution with IMAC Elution Buffer (50 mM KP_i pH 7.3, 400 mM NaCl, 500 mM Imidazole, 0.5 mM β-Mercaptoethanol, 2 mM PMSF, 0.015 mg/mL Benzamidine) for a total volume of 30 mL.

Protein eluted from the column was incubated with a 1:30 mass fraction of His-tagged TEV protease and 1:50 mass fraction of PreScission protease to cleave the N-terminal tags on both capping protein subunits. The mixture was then dialyzed overnight in IMAC Wash Buffer and passed back through the HiTrap Chelating HP column. The flow-through was collected, containing capping protein devoid of any His-tagged proteases.

The buffer in the resulting mixture was exchanged into Mono Q Low Buffer (10 mM Tris-Cl pH 8.0, 5 mM KCl, 1 mM EDTA, 1 mM DTT, 2 mM PMSF, 0.015 mg/mL

Benzamidine) using a HiPrep 26/10 Desalting column equilibrated with the same buffer. The mixture was subsequently loaded onto the Mono Q 5/50 GL column and eluted with a gradient of 0 to 40% Mono Q High Buffer (10 mM Tris-Cl pH 8.0, 1000 mM KCl, 1 mM EDTA, 1 mM DTT, 2 mM PMSF, 0.015 mg/mL Benzamidine). Capping protein fractions were concentrated and gel filtered into Storage Buffer (10 mM Tris-Cl pH 7.5, 50 mM KCl, 0.5 mM TCEP) using the Superdex 200 HiLoad 16/600. Pooled capping protein fractions were flash-frozen in liquid nitrogen following the addition of 20% glycerol before storage at -80 °C.

7.1.8 Dark mCherry

A non-fluorescent version of mCherry, referred to as dark mCherry, containing the mutation Y71S was expressed in *E. coli* BL21 Star (DE3) pRARE using a pET vector. The expression and purification conditions were identical to those used for NPFs. In brief, bacterial cells producing dark mCherry were lysed and then subjected to consecutive purification steps: IMAC, anion exchange chromatography, and size exclusion chromatography, as outlined in section 8.1.7 for NPF purification. Purified dark mCherry was flash-frozen in liquid nitrogen and stored at -80 °C.

7.2 Protein Labeling

This section includes the detailed protocols for labeling various proteins that have been utilized in the course of this study. The protein concentration of all labelled proteins were calculated as follows:

$$C_{prot} = \frac{A_{280} - (A_{max} \times CF_{dye})}{\epsilon_{prot}} \times DF \tag{7.1}$$

where C_{prot} is the concentration of the protein, A_{280} is the absorbance at 280 nm, A_{max} is the absorbance at the λ_{max} of the dye, CF_{dye} is the correction factor for the dye absorbing at 280 nm, ϵ_{prot} is the molar extinction coefficient of the protein in $M^{-1}cm^{-1}$ and DF is the dilution factor.

The degree of labeling was calculated as follows:

$$DoL = \frac{A_{max}}{\epsilon_{dye} \times C_{prot}} \times DF \tag{7.2}$$

where DoL is the degree of labeling and ϵ_{dye} is the molar extinction coefficient of the dye in $M^{-1}cm^{-1}$.

7.2.1 Pyrene labeling

α-actin was labeled with pyrene for use in polymerization assays. First, α-actin was pre-reduced by adding 1 mM TCEP and centrifuged at 350,000 rcf for 30 minutes at 4 °C. The actin pellet was then resuspended in Labeling Buffer (1x KMEI, 0.2 mM ATP). The labeling reaction was initiated by mixing the actin with a 5:1 molar ratio of N-(1-Pyrene)Iodoacetamide dissolved in DMSO and incubating on ice for 2 hours. The labeling reaction was quenched by adding DTT to reach a concentration of 10 mM, followed by centrifugation at 350,000 rcf for 30 minutes at 4 °C. The actin pellet was resuspended in G-Buffer and dialyzed against the same buffer for 5 days at 4 °C while being gently stirred. Subsequently, the dialysate was centrifuged at 350,000 rcf to separate any remaining polymeric actin, and the supernatant was gel-filtered into G-Buffer using a Superdex 75 HiLoad 16/600 column. The fractions including and following the peak fractions were stored separately at 4°C. Actin concentration was measured at 290 nm and adjusted with the CF_{dye} of pyrene at 290 nm.

7.2.2 SNAP-tag based self-labeling

A recombinant version of capping protein, with an N-terminal SNAP-tag, was labeled with SNAP-Cell TMR-Star. The labeling reaction was initiated by mixing capping protein with a 3:1 molar ratio of SNAP-Cell TMR-Star and incubating at 16 °C for 5 hours, followed by an overnight incubation on ice. The mixture was centrifuged at 350,000 rcf for 30 minutes at 4 °C to pellet any precipitation that might have formed during the labeling reaction. After centrifugation, the resulting supernatant was gel-filtered into Storage Buffer (10 mM Tris-Cl pH 7.5, 50 mM KCl, 0.5 mM TCEP) using

a Superose 6 Increase 10/300 GL column. Pooled capping protein fractions were flash-frozen in liquid nitrogen and then stored at -80 °C following the addition of 20% glycerol.

7.2.3 Maleimide labeling

Monomeric NPFs and dimeric NPFs, as well as the Arp2/3 complex, were labeled with dyes containing a maleimide functional group. Specifically, monomeric and dimeric versions of NPFs were labeled with Cy3-maleimide dye, while the Arp2/3 complex was labeled with the AlexaFluor647-maleimide dye.

Before labeling, proteins were first reduced by adding 1 mM DTT and incubating on ice for 20 minutes. The buffer of the resulting mixture was then exchanged with the Labeling Buffer (equivalent to the Storage Buffer of the respective proteins but without any reducing agent) using a NAP-5 column.

The labeling reaction was initiated by mixing the protein solution with a 5:1 molar ratio of their respective dyes, dissolved in DMSO, and incubating on ice for 2 hours. The labeling reaction was quenched by adding DTT to reach a concentration of 5 mM, followed by centrifugation at 350,000 rcf for 30 minutes at 4 °C. After centrifugation, the supernatant was concentrated and gel-filtered into the Storage Buffer of the respective proteins using either a Superdex 75 Increase 10/300 column (for Monomeric NPFs) or the Superose 6 Increase 10/300 GL column (for Arp2/3 complex and dimeric NPFs). The pooled protein fractions were then flash-frozen in liquid nitrogen and stored at -80 °C following the addition of 20% glycerol.

7.3 NPF Dimerization

Dimeric versions of constitutively active NPFs were generated by covalently linking two protein molecules via their N-terminal KCK motifs using a crosslinking agent containing a bifunctional maleimide group. The dimerization reaction was initiated by adding a 1:2 molar ratio of the crosslinker, BM(PEG)3, to monomeric NPF and incubating at room temperature for 10 minutes. Subsequently, the reaction was quenched by adding 10 mM β-Mercaptoethanol to the solution.

Following the dimerization reaction, the resulting mixture was loaded onto a Mono Q 5/50 GL column and washed with the Mono Q Low Buffer (20 mM Tris-Cl pH 8.0, 50 mM NaCl, 0.5 mM EDTA, 0.5 mM TCEP). Bound protein was eluted in a gradient elution from 0% to 60% of the Mono Q High Buffer (20 mM Tris-Cl pH 8.0, 1000 mM NaCl, 0.5 mM EDTA, 0.5 mM TCEP) over 30 column volumes. After elution, fractions containing dimeric NPF were concentrated and gel filtered into Storage Buffer (20 mM Tris-Cl pH 7.5, 150 mM NaCl, 0.1 mM EDTA, 0.5 mM TCEP) using a Superose 6 Increase 10/300 GL column. NPF dimers eluted at earlier volume fractions and were successfully separated as confirmed by results from SDS-PAGE. Fractions containing dimeric NPF were pooled and flash-frozen in liquid nitrogen with the addition of 20% glycerol before storage at -80 °C.

7.4 Mother Filament Stabilization

Preformed actin filaments were utilized as mother filaments to facilitate Arp2/3 complex branching. To prevent mother filaments from engaging in actin polymerization dynamics, they were stabilized. Stabilization ensured two objectives: first, the barbed ends of the filaments did not participate in the polymerization reaction, and second, the filaments did not depolymerize and elevated the concentration of monomeric actin in the reaction mixture. To accomplish these goals, mother filaments were capped with capping protein to inhibit polymerization from the barbed end and bound to phalloidin to prevent depolymerization. As all reactions involving mother filaments were performed in the presence of profilin-actin complexes, the free pointed ends of stabilized mother filaments could not participate in polymerization reactions.

Mother filaments were produced by incubating preformed actin filaments with a 1:10 molar ratio of capping protein and a 1:1 molar ratio of phalloidin. First, the preformed actin filaments were centrifuged at 350,000 rcf for 30 minutes at 4 °C and the pellet was gently resuspended without extensive shearing, in K-mix Buffer (1x KMEI, 2 mM β-Mercaptoethanol, 1 mM ATP, 0.1 mg/mL β-Casein) and the protein concentration was determined by absorbance at 280 nm. Next, capping protein and phalloidin were added to the resuspended filaments and incubated for 15 minutes at room temperature. The mixture was then centrifuged at 350,000 rcf for 30 minutes at 4 °C to remove excess

free capping protein and phalloidin, and the pellet was gently resuspended in K-mix Buffer.

7.5 Lipid Preparations

This section includes the detailed protocols for various lipid bilayer based experiments that have been utilized in the course of this study.

7.5.1 Small Unilamellar Vesicles

Small unilamellar lipid vesicles were generated by extruding a lipid mixture through a membrane filter with a pore size of 30 nm. Two different lipid compositions were prepared: one consisted only of PC lipids (100% DOPC, 4 mM), and the other contained a mixture of PC lipids and Ni-containing lipids (98% DOPC and 2% DGS-NTA(Ni) mole fraction of 4 mM). The obtained lipid vesicles were used for the preparation of lipid coated beads and supported lipid bilayers.

To avoid contaminations, all glassware employed in the preparation process was thoroughly cleaned. Initially, it was rinsed with ultrapure water (TOC $\leq$ 3.5 ppb and conductivity of 18.2 Ω·cm at 25 °C) followed by incubation in Hellmanex III, a liquid alkaline detergent, for 30 minutes at 60 °C. After rinsing with ultrapure water, the glassware was sonicated for 30 minutes in 50% isopropanol. Subsequently, it was rinsed in ultrapure water and acid-etched in Piranha solution (5:8 concentrated H_2SO_4 and 3:8 H_2O_2 by volume fraction) for one hour. After removing the Piranha solution, the glassware was rinsed extensively with ultrapure water before incubating at 60 °C overnight to dry. The acid etching step was only required for lipid preparations used in single-molecule microscopy experiments.

Lipid mixtures were dissolved in chloroform and evaporated under reduced pressure using a rotary evaporator at 110 rpm. The round bottom flasks containing the lipid mixtures were immersed in a water bath maintained at 42 °C after the vacuum pressure was approximately 100 mbar. Once the vacuum pressure was approximately 1 mbar and

the solvent had evaporated, the flasks were further desiccated under high vacuum in a desiccator for an additional 20 minutes.

Subsequently, the dried lipids were dissolved in PBS and gently vortexed for 2 minutes to ensure complete lipid solubilization. The resulting aqueous lipid mixture was extruded through a 30 nm polycarbonate filter to obtain small, unilamellar vesicles. The lipid mixture was extruded 11 times with gastight syringes that had been cleaned similar to the glassware. The resulting small unilamellar lipid vesicles were stored at 4 °C for further use.

7.5.2 Lipid Coated Beads

The glass microspheres underwent a series of cleaning processes to prepare them for coating with lipids. First, 150 μL of 1 μm silica microspheres were transferred into a 1.5 mL glass vial and submerged in 1 mL of concentrated nitric acid. The tubes were then vortexed for 15 seconds and incubated for an hour for acid etching. Following incubation, the samples were vortexed and centrifuged at 50 rcf for 2 minutes to remove the nitric acid, followed by resuspension in MilliQ water, with this process being repeated thrice until the beads were washed free of any residual nitric acid. Following several washes with MilliQ water, the beads were resuspended in 150 μL of 1M HEPES (pH 7.0) and centrifuged at 50 rcf for 2 minutes to remove HEPES and resuspend the beads in 150 μL water to recreate a 10% bead slurry ready for being coated with lipids.

Subsequently, the glass beads underwent lipid coating through the addition of SUVs (Small Unilamellar Vesicles). The beads were first diluted in PBS and bath sonicated for 10 minutes to facilitate the formation of a homogeneous suspension. Then, 2 mM SUVs were added, and the samples were incubated while being rotated at 40 rpm for 3 hours to enable lipid coating. Note that the volume of PBS and SUVs were adjusted to acheive a final concentration of 1% bead slurry a minimum of 250 μM SUVs in the mixture. After incubation, the beads were washed with MilliQ water, centrifuged at 50 rcf for 2 minutes, with the step being repeated five times, to remove any unbound SUVs. After the final centrifugation, the beads were resuspended in PBS, to creating a final concetration of 1% bead slurry for further usage.

7.5.3 Embedding NPFs on beads

The lipid-coated glass beads were combined with a protein solution containing various fractions of labeled His-tagged NPF and fluorescently dead variant of His-tagged mCherry (dCherry). The specific fractions of the two proteins were determined based on the required ratio of NPF to dCherry density. While maintaining a constant amount of NPF, the concentration of dCherry was adjusted accordingly. The lipid-coated beads were then incubated with the protein mixture for 30 minutes while being rotated at 40 rpm to facilitate protein embedding on their surface.

Subsequently, the tubes were centrifuged at 50 rcf for 2 minutes to pellet the beads. The supernatant was carefully removed and stored for fluorescence measurement to ascertain the concentration of NPF depleted from the solution. The pelleted beads were then resuspended in the necessary assay buffer, and the amount of NPF bound to the lipid-coated beads was determined by calculating the difference in NPF concentrations before and after adding the lipid-coated beads.

7.6 Biochemical Assays and Microscopy

This section includes the detailed protocols for various biochemical assays and microscopy experiments that have been utilized in the course of this study.

7.6.1 Pyrene Assay

Pyrene assays were performed to monitor actin nucleation and polymerization kinetics. Each reaction was divided into two components. The first component, referred to as the G-Mix, contained monomeric actin and/or profilin in low salt buffer (G-Buffer). The second component, known as the K-Mix, contained proteins used to modulate the nucleation and polymerization of actin alone or profilin-bound actin, in high salt polymerization buffer (1x KMEI, 2 μM β-Mercaptoethanol, 1 mM ATP, 0.1 mg/mL β-Casein).

Components dissolved in the G-Mix were first exchanged into $MgCl_2$ containing buffer (50 μM MgCl2, 200 μM EGTA) to exchange Ca^{2+} ions with Mg^{2+} ions by incubating

for 2 minutes. After the divalent cation exchange, the G-Mix was combined with the K-Mix to initiate the reaction and pyrene fluorescence measurements were recorded over the time course of the reaction on a microplate spectrophotometer.

All protein components were adjusted to higher concentrations in the initial G-Mix and K-Mix such that the final mixture after combining the Mg^{2+} exchange G-Mix with the K-Mix contained the desired final concentrations of proteins used in the reaction.

7.6.2 Bead Motility Assay

A bead motility assay was conducted to grow branched actin networks on membrane-coated beads embedded with NPFs. The polymerization reaction was set up using 5 μM actin, 6 μM profilin, 50 nM Arp2/3 complex, 150 nM CP, and NPF-coated beads at varying densities. Similar to the setup in pyrene assays, the reaction components were separated into two mixtures: G-Mix containing actin and profilin, and K-Mix containing the remaining components necessary for nucleation. The K-Mix also contained 15 nM AlexaFluor488-labeled LifeAct for visualizing actin filaments later.

First, the G-Mix was exchanged with Mg^{2+} containing buffer for a duration of 2 minutes to initiate the cation exchange process. Then, the G-Mix was combined with the K-Mix to initiate the polymerization reaction. The polymerization reaction was allowed to proceed for a period of 5 minutes at 22 °C. Afterward, the reaction was quenched by adding 5 μM phalloidin and 5 μM Latrunculin A.

Actin networks grown on membrane-coated beads were observed using multichannel epifluorescence microscopy imaging to visualize actin filaments (AlexaFluor488) and NPF (Cy3).

Microscopy images were acquired using a customized Nikon Ti2 microscope, equipped with the Nikon Perfect Focus System. The microscope was set to epifluorescence mode, and images were obtained using a dual EMCCD Andor iXon camera system (Cairn), controlled by NIS-Elements software. Dual color imaging was performed through an Apo TIRF 60x oil DIC N2 objective. This objective was used in conjunction with a custom multilaser launch system (AcalBFi LC) to visualize samples at excitation wavelengths of 488 nm and 560 nm. The Quad-Notch filter (400-410/488/561/631-640 nm) was used to selectively capture emitted light from the respective fluorophores.

7.7 Data Analysis

In this section, a detailed description is given on how the analysis methods were implemented for every separate dataset in the study.

7.7.1 NPF Density and Intermolecular Distance Calculation

NPF density was calculated from the amount of NPF embedded onto membrane-coated beads and amount of beads in the mixture. The molecular density of NPF was calculated as follows:

$$\rho_N = \frac{C_N \times V \times N_A}{\rho_B \times V \times 4\pi r_B^2} = \frac{C_N \times N_A}{\rho_B \times 4\pi r_B^2} \tag{7.3}$$

where, ρ_N is the molecular density of NPF in molecules/μm^2, ρ_B is the bead density in solution, C_N is the concentration of NPF embedded onto the membrane-coated beads, V is the bead mixture volume, N_A is the Avagadro constant and r_B is the radius of the bead in μm.

The average intermolecular distance between NPF molecules on NPF coated beads was calculated as follows:

$$\langle d_N \rangle = \frac{1}{2\sqrt{\rho_N}} \tag{7.4}$$

where $\langle d_N \rangle$ is the average intermolecular distance between NPF molecules.

7.7.2 Filament Length Tracking

Timelapse TIRF microscopy images of actin filaments were denoised using the Non-Local Means algorithm implemented with a custom Python script. Subsequently, lengths of individual actin filaments were tracked over time with the JFilament plugin on ImageJ. The following parameters were specified for the analysis: alpha = 15, beta = 10,

gamma = 20,000, weight = 0.5, stretch = 2,000, deform iteration = 200, spacing = 1.0, smoothing = 1.01. To define the foreground (filament) and background regions for analysis, relevant areas were manually selected within the images using corresponding tools provided in the ImageJ interface.

The average lengths of filaments from various samples were determined and employed in calculating depolymerization velocities. Instantaneous velocities were calculated by fitting local linear regression lines of varying window sizes around specific time points. Window sizes were systematically selected to ensure reliable predictions of fit parameters with an average prediction standard deviation error below 10%. Instantaneous velocities calculated for each time point were averaged across various window sizes. An exponential decay function of the form $y = ae^{bx} + c$ was employed to fit the $1/v_{depol}$ versus filament age τ curves, where:

$$y = \frac{1}{v_{depol}} \tag{7.5}$$

$$b = k_{-P_i} \tag{7.6}$$

$$c = \frac{1}{v_{depol}^{ADP}} \tag{7.7}$$

$$a + c = \frac{1}{v_{depol}^{ADP \cdot P_i}} \tag{7.8}$$

where v_{depol}^{ADP} is depolymerization velocity of ADP-bound actin subunit, $v_{depol}^{ADP \cdot P_i}$ is depolymerization velocity of ADP-P_i-bound actin subunit and k_{-P_i} is the P_i release rate constant.

Filament age was calculated as follows:

$$\tau = t + \frac{L_0 - L_t}{v_{pol}} \tag{7.9}$$

where t is the time since depolymerization, L_0 is the filament length at the start of depolymerization, L_t is the filament length at time t, and v_{pol} is the polymerization velocity.

References

[1] Henry Higgs. Getting down to basics with actin. *Nature Cell Biology*, 3(8):E189–E189, August 2001.

[2] Johanna Funk, Felipe Merino, Larisa Venkova, Lina Heydenreich, Jan Kierfeld, Pablo Vargas, Stefan Raunser, Matthieu Piel, and Peter Bieling. Profilin and formin constitute a pacemaker system for robust actin filament growth. *eLife*, 8:e50963, October 2019.

[3] Peter W. Gunning, Umesh Ghoshdastider, Shane Whitaker, David Popp, and Robert C. Robinson. The evolution of compositionally and functionally distinct actin filaments. *Journal of Cell Science*, 128(11):2009–2019, June 2015.

[4] Edward D. Korn, Marie-France Carlier, and Dominique Pantaloni. Actin Polymerization and ATP Hydrolysis. *Science*, 238(4827):638–644, October 1987.

[5] Roberto Dominguez and Kenneth C. Holmes. Actin Structure and Function. *Annual Review of Biophysics*, 40(1):169–186, June 2011.

[6] Thomas D. Pollard and John A. Cooper. Actin, a Central Player in Cell Shape and Movement. *Science*, 326(5957):1208–1212, November 2009.

[7] Isabelle Sagot, Saskia K. Klee, and David Pellman. Yeast formins regulate cell polarity by controlling the assembly of actin cables. *Nature Cell Biology*, 4(1):42–50, January 2002.

[8] T.J Mitchison and L.P Cramer. Actin-Based Cell Motility and Cell Locomotion. *Cell*, 84(3):371–379, February 1996.

[9] I Rayment, H. Holden, M Whittaker, C. Yohn, M Lorenz, K. Holmes, and R. Milligan. Structure of the actin-myosin complex and its implications for muscle contraction. *Science*, 261(5117):58–65, July 1993.

[10] Francesc Miralles and Neus Visa. Actin in transcription and transcription regulation. *Current Opinion in Cell Biology*, 18(3):261–266, June 2006.

[11] Ira M. Herman. Actin isoforms. *Current Opinion in Cell Biology*, 5(1):48–55, February 1993.

[12] Sofia Yu. Khaitlina. Functional specificity of actin isoforms. In *International Review of Cytology*, volume 202, pages 35–98. Elsevier, 2001.

[13] Laurent Blanchoin, Rajaa Boujemaa-Paterski, Cécile Sykes, and Julie Plastino. Actin Dynamics, Architecture, and Mechanics in Cell Motility. *Physiological Reviews*, 94(1):235–263, January 2014.

[14] Dominique Pantaloni, Christophe Le Clainche, and Marie-France Carlier. Mechanism of Actin-Based Motility. *Science*, 292(5521):1502–1506, May 2001.

[15] Pieta K. Mattila and Pekka Lappalainen. Filopodia: molecular architecture and cellular functions. *Nature Reviews Molecular Cell Biology*, 9(6):446–454, June 2008.

[16] Revathi Ananthakrishnan and Allen Ehrlicher. The Forces Behind Cell Movement. *International Journal of Biological Sciences*, pages 303–317, 2007.

[17] Stéphanie Pellegrin and Harry Mellor. Actin stress fibres. *Journal of Cell Science*, 120(20):3491–3499, October 2007.

[18] Michael Murrell, Patrick W. Oakes, Martin Lenz, and Margaret L. Gardel. Forcing cells into shape: the mechanics of actomyosin contractility. *Nature Reviews Molecular Cell Biology*, 16(8):486–498, August 2015.

[19] Richard B. Dickinson. Models for actin polymerization motors. *Journal of Mathematical Biology*, 58(1-2):81–103, January 2009.

[20] Fumio Oosawa, Sho Asakura, Ken Hotta, Nobuhisa Imai, and Tatsuo Ooi. G-F transformation of actin as a fibrous condensation. *Journal of Polymer Science*, 37(132):323–336, June 1959.

[21] Fumio Oosawa and Michiki Kasai. A theory of linear and helical aggregations of macromolecules. *Journal of Molecular Biology*, 4(1):10–21, January 1962.

[22] M Carlier. Actin polymerization and ATP hydrolysis. *Advances in Biophysics*, 26:51–73, 1990.

[23] Edward M. Bonder, Douglas J. Fishkind, and Mark S. Mooseker. Direct measurement of critical concentrations and assembly rate constants at the two ends of an actin filament. *Cell*, 34(2):491–501, September 1983.

[24] David Sept and J. Andrew McCammon. Thermodynamics and Kinetics of Actin Filament Nucleation. *Biophysical Journal*, 81(2):667–674, August 2001.

[25] Aaron D. Rosenbloom, Elizabeth W. Kovar, David R. Kovar, Leslie M. Loew, and Thomas D. Pollard. Mechanism of actin filament nucleation. *Biophysical Journal*, 120(20):4399–4417, October 2021.

[26] I. Fujiwara, D. Vavylonis, and T. D. Pollard. Polymerization kinetics of ADP- and ADP-Pi-actin determined by fluorescence microscopy. *Proceedings of the National Academy of Sciences*, 104(21):8827–8832, May 2007.

[27] Thomas D. Pollard. Regulation of Actin Filament Assembly by Arp2/3 Complex and Formins. *Annual Review of Biophysics and Biomolecular Structure*, 36(1):451–477, June 2007.

[28] Thomas D. Pollard. Measurement of rate constants for actin filament elongation in solution. *Analytical Biochemistry*, 134(2):406–412, October 1983.

[29] T D Pollard. Polymerization of ADP-actin. *The Journal of cell biology*, 99(3):769–777, September 1984.

[30] Beáta Bugyi and Marie-France Carlier. Control of Actin Filament Treadmilling in Cell Motility. *Annual Review of Biophysics*, 39(1):449–470, April 2010.

[31] Marie-France Carlier and Shashank Shekhar. Global treadmilling coordinates actin turnover and controls the size of actin networks. *Nature Reviews Molecular Cell Biology*, 18(6):389–401, June 2017.

[32] M Fechheimer and S H Zigmond. Focusing on unpolymerized actin. *The Journal of cell biology*, 123(1):1–5, October 1993.

[33] Albrecht Wegner. Treadmilling of actin at physiological salt concentrations. *Journal of Molecular Biology*, 161(4):607–615, November 1982.

[34] Marie-France Carlier and Dominique Pantaloni. Control of actin dynamics in cell motility. *Journal of Molecular Biology*, 269(4):459–467, June 1997.

[35] J A Cooper. The Role of Actin Polymerization in Cell Motility. *Annual Review of Physiology*, 53(1):585–605, October 1991.

[36] Ingrid Blikstad, Francis Markey, Lars Carlsson, Torgny Persson, and Uno Lindberg. Selective assay of monomeric and filamentous actin in cell extracts, using inhibition of deoxyribonuclease I. *Cell*, 15(3):935–943, November 1978.

[37] T L Hill. Microfilament or microtubule assembly or disassembly against a force. *Proceedings of the National Academy of Sciences*, 78(9):5613–5617, September 1981.

[38] Tai Kiuchi, Tomoaki Nagai, Kazumasa Ohashi, and Kensaku Mizuno. Measurements of spatiotemporal changes in G-actin concentration reveal its effect on stimulus-induced actin assembly and lamellipodium extension. *Journal of Cell Biology*, 193(2):365–380, April 2011.

[39] A. Mogilner and G. Oster. Cell motility driven by actin polymerization. *Biophysical Journal*, 71(6):3030–3045, December 1996.

[40] Scot C. Kuo and James L. McGrath. Steps and fluctuations of Listeria monocytogenes during actin-based motility. *Nature*, 407(6807):1026–1029, October 2000.

[41] Fabien Gerbal, Valérie Laurent, Albrecht Ott, Marie-France Carlier, Paul Chaikin, and Jacques Prost. Measurement of the elasticity of the actin tail of Listeria monocytogenes. *European Biophysics Journal*, 29(2):134–140, May 2000.

[42] Mandy I. Cheng, Chen Chen, Patrik Engström, Daniel A. Portnoy, and Gabriel Mitchell. Actin-based motility allows *Listeria monocytogenes* to avoid autophagy in the macrophage cytosol. *Cellular Microbiology*, 20(9), September 2018.

[43] Arpita Upadhyaya, Jeffrey R. Chabot, Albina Andreeva, Azadeh Samadani, and Alexander Van Oudenaarden. Probing polymerization forces by using actin-propelled lipid vesicles. *Proceedings of the National Academy of Sciences*, 100(8):4521–4526, April 2003.

[44] Alex Mogilner and George Oster. Polymer Motors: Pushing out the Front and Pulling up the Back. *Current Biology*, 13(18):R721–R733, September 2003.

[45] A. Ghosh and N.S. Gov. Dynamics of Active Semiflexible Polymers. *Biophysical Journal*, 107(5):1065–1073, September 2014.

[46] B. Xue and R. C. Robinson. Actin-Induced Structure in the Beta-Thymosin Family of Intrinsically Disordered Proteins. *Vitamins and Hormones*, 102:55–71, 2016.

[47] I. Perelroizen, J. B. Marchand, L. Blanchoin, D. Didry, and M. F. Carlier. Interaction of profilin with G-actin and poly(L-proline). *Biochemistry*, 33(28):8472–8478, July 1994.

[48] Cristian Suarez, Robert T. Carroll, Thomas A. Burke, Jenna R. Christensen, Andrew J. Bestul, Jennifer A. Sees, Michael L. James, Vladimir Sirotkin, and David R. Kovar. Profilin regulates F-actin network homeostasis by favoring formin over Arp2/3 complex. *Developmental Cell*, 32(1):43–53, January 2015.

[49] L. A. Selden, H. J. Kinosian, J. E. Estes, and L. C. Gershman. Impact of profilin on actin-bound nucleotide exchange and actin polymerization dynamics. *Biochemistry*, 38(9):2769–2778, March 1999.

[50] Melissa A Chesarone and Bruce L Goode. Actin nucleation and elongation factors: mechanisms and interplay. *Current Opinion in Cell Biology*, 21(1):28–37, February 2009.

[51] Theresia Eb Stradal and Giorgio Scita. Protein complexes regulating Arp2/3-mediated actin assembly. *Current Opinion in Cell Biology*, 18(1):4–10, February 2006.

[52] Fang Li and Henry N. Higgs. The mouse Formin mDia1 is a potent actin nucleation factor regulated by autoinhibition. *Current biology: CB*, 13(15):1335–1340, August 2003.

[53] Agnieszka Kobielak, H. Amalia Pasolli, and Elaine Fuchs. Mammalian formin-1 participates in adherens junctions and polymerization of linear actin cables. *Nature Cell Biology*, 6(1):21–30, January 2004.

[54] Kevin G. Young, Susan F. Thurston, Sarah Copeland, Chelsea Smallwood, and John W. Copeland. INF1 is a novel microtubule-associated formin. *Molecular Biology of the Cell*, 19(12):5168–5180, December 2008.

[55] Henry N. Higgs and Kevin J. Peterson. Phylogenetic analysis of the formin homology 2 domain. *Molecular Biology of the Cell*, 16(1):1–13, January 2005.

[56] Margot E. Quinlan, John E. Heuser, Eugen Kerkhoff, and R. Dyche Mullins. Drosophila Spire is an actin nucleation factor. *Nature*, 433(7024):382–388, January 2005.

[57] Rashmi Ahuja, Roser Pinyol, Nicole Reichenbach, Laura Custer, John Klingensmith, Michael M. Kessels, and Britta Qualmann. Cordon-bleu is an actin nucleation factor and controls neuronal morphology. *Cell*, 131(2):337–350, October 2007.

[58] David Chereau, Malgorzata Boczkowska, Aneta Skwarek-Maruszewska, Ikuko Fujiwara, David B. Hayes, Grzegorz Rebowski, Pekka Lappalainen, Thomas D. Pollard, and Roberto Dominguez. Leiomodin Is an Actin Filament Nucleator in Muscle Cells. *Science*, 320(5873):239–243, April 2008.

[59] Matthias Krause, Erik W. Dent, James E. Bear, Joseph J. Loureiro, and Frank B. Gertler. Ena/VASP proteins: regulators of the actin cytoskeleton and cell migration. *Annual Review of Cell and Developmental Biology*, 19:541–564, 2003.

[60] Majdouline Abou-Ghali, Remy Kusters, Sarah Körber, John Manzi, Jan Faix, Cécile Sykes, and Julie Plastino. Capping protein is dispensable for polarized actin network growth and actin-based motility. *The Journal of Biological Chemistry*, 295(45):15366–15375, November 2020.

[61] Shalini Nag, Mårten Larsson, Robert C. Robinson, and Leslie D. Burtnick. Gelsolin: the tail of a molecular gymnast. *Cytoskeleton (Hoboken, N.J.)*, 70(7):360–384, July 2013.

[62] Ke Xu, Guisheng Zhong, and Xiaowei Zhuang. Actin, Spectrin, and Associated Proteins Form a Periodic Cytoskeletal Structure in Axons. *Science*, 339(6118):452–456, January 2013.

[63] Qian Li, Wei Bao, Qiong Fan, Wen-Jing Shi, Zhu-Nan Li, Ying Xu, and Dan Wu. Epidermal growth factor receptor kinase substrate 8 promotes the metastasis of cervical cancer via the epithelial-mesenchymal transition. *Molecular Medicine Reports*, 14(4):3220–3228, October 2016.

[64] A. Weeds and S. Maciver. F-actin capping proteins. *Current Opinion in Cell Biology*, 5(1):63–69, February 1993.

[65] Jack V. Greiner and Thomas Glonek. Intracellular ATP Concentration and Implication for Cellular Evolution. *Biology*, 10(11):1166, November 2021.

[66] Antoine Jégou, Thomas Niedermayer, József Orbán, Dominique Didry, Reinhard Lipowsky, Marie-France Carlier, and Guillaume Romet-Lemonne. Individual Actin Filaments in a Microfluidic Flow Reveal the Mechanism of ATP Hydrolysis and Give Insight Into the Properties of Profilin. *PLoS Biology*, 9(9):e1001161, September 2011.

[67] Hugo Wioland, Berengere Guichard, Yosuke Senju, Sarah Myram, Pekka Lappalainen, Antoine Jégou, and Guillaume Romet-Lemonne. ADF/Cofilin Accelerates Actin Dynamics by Severing Filaments and Promoting Their Depolymerization at Both Ends. *Current Biology*, 27(13):1956–1967.e7, July 2017.

[68] Jose Javier Bravo-Cordero, Marco A. O. Magalhaes, Robert J. Eddy, Louis Hodgson, and John Condeelis. Functions of cofilin in cell locomotion and invasion. *Nature reviews. Molecular cell biology*, 14(7):10.1038/nrm3609, July 2013.

[69] Alexis M. Gautreau, Fred E. Fregoso, Gleb Simanov, and Roberto Dominguez. Nucleation, stabilization, and disassembly of branched actin networks. *Trends in Cell Biology*, 32(5):421–432, May 2022.

[70] Vassilis Papalazarou and Laura M. Machesky. The cell pushes back: The Arp2/3 complex is a key orchestrator of cellular responses to environmental forces. *Current Opinion in Cell Biology*, 68:37–44, February 2021.

[71] J.V. Small, S. Auinger, M. Nemethova, S. Koestler, K.N. Goldie, A. Hoenger, and G.P. Resch. Unravelling the structure of the lamellipodium. *Journal of Microscopy*, 231(3):479–485, September 2008.

[72] Amine Mehidi, Frieda Kage, Zeynep Karatas, Maureen Cercy, Matthias Schaks, Anna Polesskaya, Matthieu Sainlos, Alexis M. Gautreau, Olivier Rossier, Klemens Rottner, and Grégory Giannone. Forces generated by lamellipodial actin filament elongation regulate the WAVE complex during cell migration. *Nature Cell Biology*, 23(11):1148–1162, November 2021.

[73] T. Svitkina and G. Borisy. Arp2/3 Complex and Actin Depolymerizing Factor/-Cofilin in Dendritic Organization and Treadmilling of Actin Filament Array in Lamellipodia. *Journal of Cell Biology*, 1999.

[74] Mohammed Shaaban, Saikat Chowdhury, and Brad J. Nolen. Cryo-EM reveals the transition of Arp2/3 complex from inactive to nucleation-competent state. *Nature Structural & Molecular Biology*, 27(11):1009–1016, November 2020.

[75] Florian Fäßler, Georgi Dimchev, Victor-Valentin Hodirnau, William Wan, and Florian K. M. Schur. Cryo-electron tomography structure of Arp2/3 complex in cells reveals new insights into the branch junction. *Nature Communications*, 11(1):6437, December 2020.

[76] Robert C. Robinson, Kirsi Turbedsky, Donald A. Kaiser, Jean-Baptiste Marchand, Henry N. Higgs, Senyon Choe, and Thomas D. Pollard. Crystal Structure of Arp2/3 Complex. *Science*, 294(5547):1679–1684, November 2001.

[77] Jeremy D. Rotty, Congying Wu, and James E. Bear. New insights into the regulation and cellular functions of the ARP2/3 complex. *Nature Reviews Molecular Cell Biology*, 14(1):7–12, January 2013.

[78] Alissa M. Weaver, Andrei V. Karginov, Andrew W. Kinley, Scott A. Weed, Yan Li, J.Thomas Parsons, and John A. Cooper. Cortactin promotes and stabilizes

Arp2/3-induced actin filament network formation. *Current Biology*, 11(5):370–374, March 2001.

[79] Christine L. Humphries, Heath I. Balcer, Jessica L. D'Agostino, Barbara Winsor, David G. Drubin, Georjana Barnes, Brenda J. Andrews, and Bruce L. Goode. Direct regulation of Arp2/3 complex activity and function by the actin binding protein coronin. *The Journal of Cell Biology*, 159(6):993–1004, December 2002.

[80] Irene Dang, Roman Gorelik, Carla Sousa-Blin, Emmanuel Derivery, Christophe Guérin, Joern Linkner, Maria Nemethova, Julien G. Dumortier, Florence A. Giger, Tamara A. Chipysheva, Valeria D. Ermilova, Sophie Vacher, Valérie Campanacci, Isaline Herrada, Anne-Gaelle Planson, Susan Fetics, Véronique Henriot, Violaine David, Ksenia Oguievetskaia, Goran Lakisic, Fabienne Pierre, Anika Steffen, Adeline Boyreau, Nadine Peyriéras, Klemens Rottner, Sophie Zinn-Justin, Jacqueline Cherfils, Ivan Bièche, Antonina Y. Alexandrova, Nicolas B. David, J. Victor Small, Jan Faix, Laurent Blanchoin, and Alexis Gautreau. Inhibitory signalling to the Arp2/3 complex steers cell migration. *Nature*, 503(7475):281–284, November 2013.

[81] Meghal Gandhi, Benjamin A. Smith, Miia Bovellan, Ville Paavilainen, Karen Daugherty-Clarke, Jeff Gelles, Pekka Lappalainen, and Bruce L. Goode. GMF Is a Cofilin Homolog that Binds Arp2/3 Complex to Stimulate Filament Debranching and Inhibit Actin Nucleation. *Current Biology*, 20(9):861–867, May 2010.

[82] Tanja Maritzen, Tobias Zech, Michael R. Schmidt, Eberhard Krause, Laura M. Machesky, and Volker Haucke. Gadkin negatively regulates cell spreading and motility via sequestration of the actin-nucleating ARP2/3 complex. *Proceedings of the National Academy of Sciences*, 109(26):10382–10387, June 2012.

[83] Erin D. Goley and Matthew D. Welch. The ARP2/3 complex: an actin nucleator comes of age. *Nature Reviews Molecular Cell Biology*, 7(10):713–726, October 2006.

[84] Daniel A. Kramer, Hannah K. Piper, and Baoyu Chen. WASP family proteins: Molecular mechanisms and implications in human disease. *European Journal of Cell Biology*, 101(3):151244, June 2022.

[85] Guillaume Bompard and Emmanuelle Caron. Regulation of WASP/WAVE proteins. *The Journal of Cell Biology*, 166(7):957–962, September 2004.

[86] Elena V Linardopoulou, Sean S Parghi, Cynthia Friedman, Gregory E Osborn, Susan M Parkhurst, and Barbara J Trask. Human Subtelomeric WASH Genes Encode a New Subclass of the WASP Family. *PLoS Genetics*, 3(12):e237, December 2007.

[87] Kenneth G. Campellone, Neil J. Webb, Elizabeth A. Znameroski, and Matthew D. Welch. WHAMM is an Arp2/3 complex activator that binds microtubules and functions in ER to Golgi transport. *Cell*, 134(1):148–161, July 2008.

[88] J. Bradley Zuchero, Amanda S. Coutts, Margot E. Quinlan, Nicholas B. La Thangue, and R. Dyche Mullins. p53-cofactor JMY is a multifunctional actin nucleation factor. *Nature Cell Biology*, 11(4):451–459, April 2009.

[89] Defne Yarar, Joseph A. D'Alessio, Robert L. Jeng, and Matthew D. Welch. Motility Determinants in WASP Family Proteins. *Molecular Biology of the Cell*, 13(11):4045–4059, November 2002.

[90] Bruce L. Goode, Avital A. Rodal, Georjana Barnes, and David G. Drubin. Activation of the Arp2/3 Complex by the Actin Filament Binding Protein Abp1p. *The Journal of Cell Biology*, 153(3):627–634, April 2001.

[91] Mara C. Duncan, M. Jamie T. V. Cope, Bruce L. Goode, Beverly Wendland, and David G. Drubin. Yeast Eps15-like endocytic protein, Pan1p, activates the Arp2/3 complex. *Nature Cell Biology*, 3(7):687–690, July 2001.

[92] Scott A. Weed, Andrei V. Karginov, Dorothy A. Schafer, Alissa M. Weaver, Andrew W. Kinley, John A. Cooper, and J. Thomas Parsons. Cortactin Localization to Sites of Actin Assembly in Lamellipodia Requires Interactions with F-Actin and the Arp2/3 Complex. *The Journal of Cell Biology*, 151(1):29–40, October 2000.

[93] Andrew R. Wagner, Qing Luan, Su-Ling Liu, and Brad J. Nolen. Dip1 Defines a Class of Arp2/3 Complex Activators that Function without Preformed Actin Filaments. *Current Biology*, 23(20):1990–1998, October 2013.

[94] Qing Luan, Su-Ling Liu, Luke A Helgeson, and Brad J Nolen. Structure of the nucleation-promoting factor SPIN 90 bound to the actin filament nucleator Arp2/3 complex. *The EMBO Journal*, 37(22):e100005, November 2018.

[95] Tadaomi Takenawa and Shiro Suetsugu. The WASP–WAVE protein network: connecting the membrane to the cytoskeleton. *Nature Reviews Molecular Cell Biology*, 8(1):37–48, January 2007.

[96] Shusaku Kurisu and Tadaomi Takenawa. The WASP and WAVE family proteins. *Genome Biology*, 10(6):226, 2009.

[97] Peter Bieling, Scott D Hansen, Orkun Akin, Tai-De Li, Carl C Hayden, Daniel A Fletcher, and R Dyche Mullins. WH2 and proline-rich domains of WASP-family proteins collaborate to accelerate actin filament elongation. *The EMBO Journal*, 37(1):102–121, January 2018.

[98] Dominique Pantaloni and Marie-France Carlier. How profilin promotes actin filament assembly in the presence of thymosin 4. *Cell*, 75(5):1007–1014, December 1993.

[99] Emmanuel Derivery and Alexis Gautreau. Generation of branched actin networks: assembly and regulation of the N-WASP and WAVE molecular machines. *BioEssays*, 32(2):119–131, January 2010.

[100] Peter J. Hume, Daniel Humphreys, and Vassilis Koronakis. Chapter Twenty - WAVE Regulatory Complex Activation. In Ronald D. Vale, editor, *Methods in Enzymology*, volume 540 of *Reconstituting the Cytoskeleton*, pages 363–379. Academic Press, January 2014.

[101] Klemens Rottner, Theresia E. B. Stradal, and Baoyu Chen. WAVE regulatory complex. *Current biology: CB*, 31(10):R512–R517, May 2021.

[102] J. Fawcett and T. Pawson. Signal transduction. N-WASP regulation–the sting in the tail. *Science (New York, N.Y.)*, 290(5492):725–726, October 2000.

[103] Shae B. Padrick, Hui-Chun Cheng, Ayman M. Ismail, Sanjay C. Panchal, Lynda K. Doolittle, Soyeon Kim, Brian M. Skehan, Junko Umetani, Chad A. Brautigam,

John M. Leong, and Michael K. Rosen. Hierarchical Regulation of WASP/WAVE Proteins. *Molecular Cell*, 32(3):426–438, November 2008.

[104] Alice Y. Pollitt and Robert H. Insall. WASP and SCAR/WAVE proteins: the drivers of actin assembly. *Journal of Cell Science*, 122(15):2575–2578, August 2009.

[105] Peter Bieling and Klemens Rottner. From WRC to Arp2/3: Collective molecular mechanisms of branched actin network assembly. *Current Opinion in Cell Biology*, 80:102156, February 2023.

[106] Wout Oosterheert, Florian E. C. Blanc, Ankit Roy, Alexander Belyy, Micaela Boiero Sanders, Oliver Hofnagel, Gerhard Hummer, Peter Bieling, and Stefan Raunser. Molecular mechanisms of inorganic-phosphate release from the core and barbed end of actin filaments. *Nature Structural & Molecular Biology*, September 2023.

[107] Wout Oosterheert, Björn U. Klink, Alexander Belyy, Sabrina Pospich, and Stefan Raunser. Structural basis of actin filament assembly and aging. *Nature*, 611(7935):374–379, November 2022.

[108] Julian Von Der Ecken, Mirco Müller, William Lehman, Dietmar J. Manstein, Pawel A. Penczek, and Stefan Raunser. Structure of the F-actin–tropomyosin complex. *Nature*, 519(7541):114–117, March 2015.

[109] Nikolas Hundt, Matthias Preller, Olga Swolski, Angella M. Ang, Hans G. Mannherz, Dietmar J. Manstein, and Mirco Müller. Molecular mechanisms of disease-related human -actin mutations p.R183W and p.E364K. *The FEBS Journal*, 281(23):5279–5291, December 2014.

[110] Biljana Ilkovski, Sandra T. Cooper, Kristen Nowak, Monique M. Ryan, Nan Yang, Christina Schnell, Hayley J. Durling, Laurence G. Roddick, Ian Wilkinson, Andrew J. Kornberg, Kevin J. Collins, Geoff Wallace, Peter Gunning, Edna C. Hardeman, Nigel G. Laing, and Kathryn N. North. Nemaline Myopathy Caused by Mutations in the Muscle -Skeletal-Actin Gene. *The American Journal of Human Genetics*, 68(6):1333–1343, June 2001.

[111] Thomas Niedermayer, Antoine Jégou, Lionel Chièze, Bérengère Guichard, Emmanuèle Helfer, Guillaume Romet-Lemonne, Marie-France Carlier, and Reinhard Lipowsky. Intermittent depolymerization of actin filaments is caused by photo-induced dimerization of actin protomers. *Proceedings of the National Academy of Sciences*, 109(27):10769–10774, July 2012.

[112] Lynda K. Doolittle, Michael K. Rosen, and Shae B. Padrick. Measurement and Analysis of In Vitro Actin Polymerization. In Amanda S. Coutts, editor, *Adhesion Protein Protocols*, volume 1046, pages 273–293. Humana Press, Totowa, NJ, 2013.

[113] Ralf Jungmann, Maier S Avendaño, Mingjie Dai, Johannes B Woehrstein, Sarit S Agasti, Zachary Feiger, Avital Rodal, and Peng Yin. Quantitative super-resolution imaging with qPAINT. *Nature Methods*, 13(5):439–442, May 2016.

[114] Julie A. Theriot. The Polymerization Motor. *Traffic*, 1(1):19–28, January 2000.

[115] Rajesh Arasada and Thomas D. Pollard. Distinct roles for F-BAR proteins Cdc15p and Bzz1p in actin polymerization at sites of endocytosis in fission yeast. *Current biology: CB*, 21(17):1450–1459, September 2011.

[116] Jonathon A. Ditlev, Paul J. Michalski, Greg Huber, Gonzalo M. Rivera, William A. Mohler, Leslie M. Loew, and Bruce J. Mayer. Stoichiometry of Nck-dependent actin polymerization in living cells. *The Journal of Cell Biology*, 197(5):643–658, May 2012.

[117] Austin Zimmet, Trevor Van Eeuwen, Malgorzata Boczkowska, Grzegorz Rebowski, Kenji Murakami, and Roberto Dominguez. Cryo-EM structure of NPF-bound human Arp2/3 complex and activation mechanism. *Science Advances*, 6(23):eaaz7651, June 2020.

[118] Shae B. Padrick, Lynda K. Doolittle, Chad A. Brautigam, David S. King, and Michael K. Rosen. Arp2/3 complex is bound and activated by two WASP proteins. *Proceedings of the National Academy of Sciences*, 108(33), August 2011.

[119] Matthew J. Reynolds, Carla Hachicho, Ayala G. Carl, Rui Gong, and Gregory M. Alushin. Bending forces and nucleotide state jointly regulate F-actin structure. *Nature*, 611(7935):380–386, November 2022.

[120] G Adam and M Delbrück. Reduction of dimensionality in biological diffusion processes. *Structural chemistry and molecular biology*, 198:198–215, 1968.

List of Figures

3.1 Schematic illustration of the distinct actin networks found within a cell. . 6
3.2 Schematic representation of actin treadmilling. 9
3.3 Electron micrographs of branched actin networks at the leading edge of *Xenopus* keratocytes and fibroblasts. 18

5.1 Stochastic simulation of an aeging actin filament. 28
5.1 *Legend continued* 29
5.2 Distribution of different nucleotide states in an aging actin filament. A. Filament Length Evolution. B. Length Distribution. C. Percentage Distribution 30
5.2 *Legend continued* 31
5.3 Cryo-EM structure of the barbed end of an actin filament. A. Barbed end of an actin filament. B. Open backdoor. C. Closed backdoor. 32
5.3 *Legend continued* 33
5.4 P_i release kinetics of actin and its mutant. A. Bulk polymerization and P_i release. B. Single filament TIRF assay. C. Length evolution of filaments. D. Depolymerization velocity. E. Pausing probability. 35
5.4 *Legend continued* 36
5.5 Spontaneous nucleation and polymerization. A. Pyrene Assay. B. Spontaneous Nucleation. C. Standard Curve. D. Suppression of Nucleation. E. Quantifying Nucleation Suppression. 39
5.5 *Legend continued* 40
5.6 Branched Actin Nucleation and Metastability. A. Branched Actin Nucleation with Arp2/3 complex and NPF. B. Branched Nucleation. C. Activity of NPF and Arp. D. Metastable Reaction. E. Activity of NPF and CP. 42
5.6 *Legend continued* 43

5.7 Membrane bound NPFs rescue metastability. A. Embedding NPFs onto Membranes. B. Activity of Membrane Bound and Soluble NPF in Metastable Conditions. 45
5.7 *Legend continued* 46
5.8 Distribution of WRC at the lamellipodia. A. WRC distribution. B. Super-resolution of WRC clusters. C. Nearest neighbor distance of WRC clusters. D. Molecular densities of WRC clusters. 47
5.9 NPF density controls its activity. A. Modulating NPF Density. B. Bead Motility Assay. C. NPF Density and Intermolecular Distance. D. Density Dependent NPF Activity. E. Activity of NPF Density and CP. 49
5.9 *Legend continued* 50
5.10 Influence of dimerization on NPF activity. A. Dual NPF Binding on the Arp2/3 complex. B. NPF Monomer and Dimer Activity. C. Density Dependent NPF Activity. D. Dimer Activity at Metastability. E. Activity of NPF Density and CP. 53
5.10 *Legend continued* 54
5.11 NPF densities regulate their activity in a switch-like manner. A. Density Dependent NPF Activity of Monomers and Dimers. B. Activity of NPF Density and Modality. C. Switchlike NPF Density Response. 55
5.11 *Legend continued* 56
5.12 Mother filament supplementation. A. Membrane-bound dimeric NPF with mother filaments. B. Comparison of membrane-bound monomeric, dimeric NPFs and mother filament supplementation. 57

List of Tables

3.1 Kinetic rate constants and critical concentrations of actin at the different ends of the filament and for different nucleotide states [26, 27]. 8

Acronyms

a	Number of attached filaments.
A_{280}	Absorbance at 280 nm.
A_{max}	Absorbance at the λ_{max} of a dye.
ACTA1	Actin isoform α - skeletal muscle.
ACTA2	Actin isoform α - aortic smooth muscle.
ACTB	Actin isoform β - cytoplasmic.
ACTC1	Actin isoform α - cardiac muscle.
ACTG1	Actin isoform γ - cytoplasmic.
ACTG2	Actin isoform γ - enteric smooth muscle.
ADP	Adenosine Diphosphate.
ADP-P_i	Adenosine Diphosphate with bound P_i.
ATP	Adenosine Triphosphate.
ATPase	Adenosine 5′-TriPhosphatase.
BM(PEG)3	1,11-bismaleimido-triethyleneglycol.
$CaCl_2$	Calcium chloride.
CF_{dye}	Correction factor for a specific dye while calculating protein concentration by absorbtion at 280 nm.
CP	Capping Protein.
C_{prot}	Protein concentration.
C_c	Critical concentration.
$C_c^{BE:ATP}$	Critical concentration at the barbed end with ATP-actin.
$C_c^{PE:ADP}$	Critical concentration at the pointed end with ADP-actin.

$C_c^{PE:ATP}$	Critical concentration at the pointed end with ATP-actin.
Cy3	Cyanine3.
DEAE	Diethylaminoethyl cellulose.
δ	Filament length extension of the filament in the direction of the force.
δ_0	Rise in an actin filament per subunit addition.
DF	Dilution factor.
DGS-NTA(Ni)	1,2-dioleoyl-sn-glycero-3-[(N-(5-amino-1-carboxypentyl)iminodiacetic acid)succinyl] (Nickel salt).
DMSO	Dimethyl sulfoxide.
DNase	Deoxyribonuclease.
DoL	Degree of labeling.
DOPC	1,2-dioleoyl-sn-glycero-3-phosphocholine.
DTT	Dithiothreitol.
E. coli	*Escherichia coli*.
EDTA	Ethylenediaminetetraacetic acid.
EGTA	Ethylene glycol-bis(β-aminoethyl ether)-N,N,N′,N′-tetraacetic acid.
ϵ_{dye}	Molar extinction coefficient of dye.
ϵ_{prot}	Molar extinction coefficient of protein.
F-Buffer	Filamentous/Polymeric actin buffer.
F_{eq}	Equilibrium stall force.
$[F]$	Concentration of actin filaments.
F	External force on filaments.
F_a	Load on attached filaments.
F_L	Load on the motile surface.
F_w	Load on the total working filaments.
f	Split of the work done between polymerization and depolymerization rate.

G-Buffer	Globular/Monomeric actin buffer.
ΔG	Change in Gibb's free energy.
GST	Glutathione S-transferase.
H_2O_2	Hydrogen peroxide.
H_2SO_4	Sulfuric acid.
HA	Hydroxyapatite.
HEPES	4-(2-hydroxyethyl)-1-piperazineethanesulfonic acid.
IMAC	Immobilized Metal Ion Affinity Chromatography.
κ	Bending stiffness.
k_B	Boltzmann's constant.
k_c	Capping rate.
KCK	Lys-Cys-Lys.
KCl	Potassium chloride.
k_d	Filament detachment rate.
K_{eq}	Equilibrium constant.
KMEI	Buffer containing KCl, $MgCl_2$, EGTA and Imidazole.
k_-	Depolymerization rate constant.
KP_i	0.39 molar ratio of KH_2PO_2 and 0.61 molar ratio of K_2HPO_4.
k_+	Polymerization rate constant.
λ_{max}	The wavelength at which the dye absorbs maximally.
$MgCl_2$	Magnesium chloride.
$[M_f]$	Concentration of actin monomers in filaments.
$[M_g]$	Concentration of free actin monomers.
NaCl	Sodium chloride.
NaN_3	Sodium azide.
NaP_i	0.39 molar ratio of NaH_2PO_2 and 0.61 molar ratio of Na_2HPO_4.
Ni^{2+}	Nickel cation.

NPF	Nucleation Promoting Factor.
NWASP	Neural Wiskott-Aldrich syndrome protein.
OD600	Optical Density (absorbance) at 600 nm.
PBS	Phosphate-buffered saline.
PC	Phosphatidylcholine.
pH	Power of Hydrogen.
P_i	Inorganic phosphate.
PIPES	Piperazine-N,N′-bis(2-ethanesulfonic acid).
PMSF	Phenylmethylsulfonyl fluoride.
ppb	Parts per billion.
$p(t)$	Detachment time probability density.
$p(x)$	Probability density for opening a gap of distance x.
r	Net filament polymerization rate.
rcf	Relative Centrifugal Force.
rpm	Revolutions Per Minute.
STI	Soybean Trypsin Inhibitor.
T	Absolute temperature in K.
t	Time.
TCEP	Tris(2-carboxyethyl)phosphine.
TEV	Tobacco Etch Virus.
θ	Angle of incidence of a growing actin filament.
TMR	Tetramethylrhodamine.
TOC	Total Organic Carbon.
Tris	Tris(hydroxymethyl)aminomethane.
Tris-Cl	Tris(hydroxymethyl)aminomethane with HCl.
Trx	Thioredoxin.
$U(x)$	Potential energy of opening a gap of distance x.
V	Filament extension speed.

w	Number of working filaments.
WASP	Wiskott-Aldrich syndrome protein.
WAVE	WASP-family verprolin-homologous protein.
x	Gap opening distance.
x_0	Equilibrium position of the actin filament end.

A Source Code

This appendix includes the source code for all scripts utilized in the data analysis presented within this thesis. You can obtain an up-to-date copy of the entire repository for personal use by cloning or forking it from **github.com@iamankitroy**.

A.1 Stochastic Simulation of an Ageing Actin Filament

```
#!/Users/roy/anaconda3/bin/python

import numpy as np
import pickle

def initiate_actin(time, pol_time, scale, rates):
    # 110% actin length
    max_length = int((pol_time * rates["k_pol"]) * 1.1)
    # actin filament
    scaled_time = int(time/scale)
    actin = np.zeros(shape = (scaled_time, max_length), dtype = np.
        ↪ uint8)

    return actin


def events_per_timescale(rates, scale):
```

```
17      return {key: value*scale for key, value in zip(rates.keys(),
            ↪ rates.values())}
18
19
20  def polymerize(filament, end_pos):
21      if np.random.uniform() <= rates_scaled["k_pol"]:
22          filament[end_pos] = 3
23          end_pos += 1
24
25      return filament, end_pos
26
27
28  def hydrolyze_atp(filament):
29      atp_subunits = (filament == 3).astype(int)
30
31      change_probs = (np.random.uniform(size = filament.size) <=
            ↪ rates_scaled["k_adp_pi"]).astype(int)
32
33      change_state = (atp_subunits * change_probs).astype(bool)
34
35      filament[change_state] = 2
36
37      return filament
38
39
40  def release_internalPi(filament, end_pos):
41      adp_pi_subunits = (filament == 2).astype(int)
42
43      change_probs = (np.random.uniform(size = filament.size) <=
            ↪ rates_scaled["k_adp_int"]).astype(int)
44
45      change_state = (adp_pi_subunits * change_probs).astype(bool)
46      change_state[end_pos] = False
47
48      filament[change_state] = 1
```

```
49
50      return filament
51
52
53  def release_terminalPi(filament, end_pos):
54      if (filament[end_pos] == 2) and (np.random.uniform() <=
            ↪ rates_scaled["k_adp_ter"]):
55          filament[end_pos] = 1
56
57      return filament
58
59
60  def depolymerize(filament, end_pos):
61
62      prob = np.random.uniform()
63
64      if (end_pos == 3) and (prob <= rates_scaled["k_atp_depol"]):
65          filament[end_pos] = 0
66          end_pos -= 1
67
68      elif (end_pos == 2) and (prob <= rates_scaled["k_adp_pi_depol"
            ↪ ]):
69          filament[end_pos] = 0
70          end_pos -= 1
71
72      elif prob <= rates_scaled["k_adp_depol"]:
73          filament[end_pos] = 0
74          end_pos -= 1
75
76      return filament, end_pos
77
78
79  def cycle_polymerization(actin, end_pos, time, pol_time):
80
81      scaled_time = int(time/scale)
```

```
82      scaled_pol_time = int(pol_time/scale)
83
84      simulation_results = []
85
86      for t in range(1, scaled_time):
87          filament = actin[t-1]
88          actin[t] = hydrolyze_atp(filament)
89          actin[t] = release_internalPi(filament, end_pos)
90          actin[t] = release_terminalPi(filament, end_pos)
91
92          if t <= scaled_pol_time:
93              actin[t], end_pos = polymerize(filament, end_pos)
94          else:
95              actin[t], end_pos = depolymerize(filament, end_pos)
96
97          simulation_results.append((t,
98          end_pos,
99          round(sum(actin[t]==3)/end_pos, 3),
100         round(sum(actin[t]==2)/end_pos, 3),
101         round(sum(actin[t]==1)/end_pos, 3)))
102
103         print(t,
104             end_pos,
105             round(sum(actin[t]==3)/end_pos, 3),
106             round(sum(actin[t]==2)/end_pos, 3),
107             round(sum(actin[t]==1)/end_pos, 3))
108
109     writeOUT(simulation_results, actin)
110
111
112 def writeOUT(simulation_results, actin):
113
114     with open("actin_time-evol.p", "wb") as fh:
115         pickle.dump(actin, fh)
116
```

```
117     with open("simulation_results.p", "wb") as fh:
118         pickle.dump(simulation_results, fh)
119 
120 
121 def main():
122 
123     global actin
124     global rates_scaled
125     global scale
126 
127     rates = {
128         "k_pol" : 320,    # monomers per second
129         "k_adp_pi" : 0.3,   # per second
130         "k_adp_int" : 0.011,  # per second
131         "k_adp_ter" : 5.084,  # per second
132         "k_atp_depol" : 1.4,  # per second
133         "k_adp_pi_depol" : 0.2,  # per second
134         "k_adp_depol" : 6.598  # per second
135     }
136 
137     # simulation time
138     time = 15 * 60     # seconds
139     pol_time = 30     # seconds
140     scale = 1e-3     # scale to milliseconds
141 
142     # initiate end position
143     end_pos = 0
144 
145     actin = initiate_actin(time, pol_time, scale, rates)
146     rates_scaled = events_per_timescale(rates, scale)
147     cycle_polymerization(actin, end_pos, time, pol_time)
148 
149 main()
150 
151 # Ankit Roy
```

```
152 # 21st February, 2021
153 # 13th March, 2023  >>  Changed kinetic constants to ones that
    ↪ were determined from my single filament experiments.
154 #      >>  Changed the 2D actin time evolution matrix to 8 bit
    ↪ unsigned integer data type to save data
```

Listing A.1: Stochastic Simulation of an Ageing Actin Filament

Eidesstattliche Versicherung (Affidavit)

Name, Vorname
(Surname, first name)

Matrikel-Nr.
(Enrolment number)

Belehrung:

Wer vorsätzlich gegen eine die Täuschung über Prüfungsleistungen betreffende Regelung einer Hochschulprüfungsordnung verstößt, handelt ordnungswidrig. Die Ordnungswidrigkeit kann mit einer Geldbuße von bis zu 50.000,00 € geahndet werden. Zuständige Verwaltungsbehörde für die Verfolgung und Ahndung von Ordnungswidrigkeiten ist der Kanzler/die Kanzlerin der Technischen Universität Dortmund. Im Falle eines mehrfachen oder sonstigen schwerwiegenden Täuschungsversuches kann der Prüfling zudem exmatrikuliert werden, § 63 Abs. 5 Hochschulgesetz NRW.

Die Abgabe einer falschen Versicherung an Eides statt ist strafbar.

Wer vorsätzlich eine falsche Versicherung an Eides statt abgibt, kann mit einer Freiheitsstrafe bis zu drei Jahren oder mit Geldstrafe bestraft werden, § 156 StGB. Die fahrlässige Abgabe einer falschen Versicherung an Eides statt kann mit einer Freiheitsstrafe bis zu einem Jahr oder Geldstrafe bestraft werden, § 161 StGB.

Die oben stehende Belehrung habe ich zur Kenntnis genommen:

Official notification:

Any person who intentionally breaches any regulation of university examination regulations relating to deception in examination performance is acting improperly. This offence can be punished with a fine of up to EUR 50,000.00. The competent administrative authority for the pursuit and prosecution of offences of this type is the chancellor of the TU Dortmund University. In the case of multiple or other serious attempts at deception, the candidate can also be unenrolled, Section 63, paragraph 5 of the Universities Act of North Rhine-Westphalia.

The submission of a false affidavit is punishable.

Any person who intentionally submits a false affidavit can be punished with a prison sentence of up to three years or a fine, Section 156 of the Criminal Code. The negligent submission of a false affidavit can be punished with a prison sentence of up to one year or a fine, Section 161 of the Criminal Code.

I have taken note of the above official notification.

Ort, Datum
(Place, date)

Unterschrift
(Signature)

Titel der Dissertation:
(Title of the thesis):

Ich versichere hiermit an Eides statt, dass ich die vorliegende Dissertation mit dem Titel selbstständig und ohne unzulässige fremde Hilfe angefertigt habe. Ich habe keine anderen als die angegebenen Quellen und Hilfsmittel benutzt sowie wörtliche und sinngemäße Zitate kenntlich gemacht.
Die Arbeit hat in gegenwärtiger oder in einer anderen Fassung weder der TU Dortmund noch einer anderen Hochschule im Zusammenhang mit einer staatlichen oder akademischen Prüfung vorgelegen.

I hereby swear that I have completed the present dissertation independently and without inadmissible external support. I have not used any sources or tools other than those indicated and have identified literal and analogous quotations.

The thesis in its current version or another version has not been presented to the TU Dortmund University or another university in connection with a state or academic examination.*

*Please be aware that solely the German version of the affidavit ("Eidesstattliche Versicherung") for the PhD thesis is the official and legally binding version.

Ort, Datum
(Place, date)

Unterschrift
(Signature)